

**ASSESSING THE EFFECTS OF
SEA LEVEL RISE ON URBAN
FLOODS, A 1D2D SATELLITE-
BASED FLOOD INUNDATION
MODELLING APPROACH IN
ACCRA COASTAL ZONE**

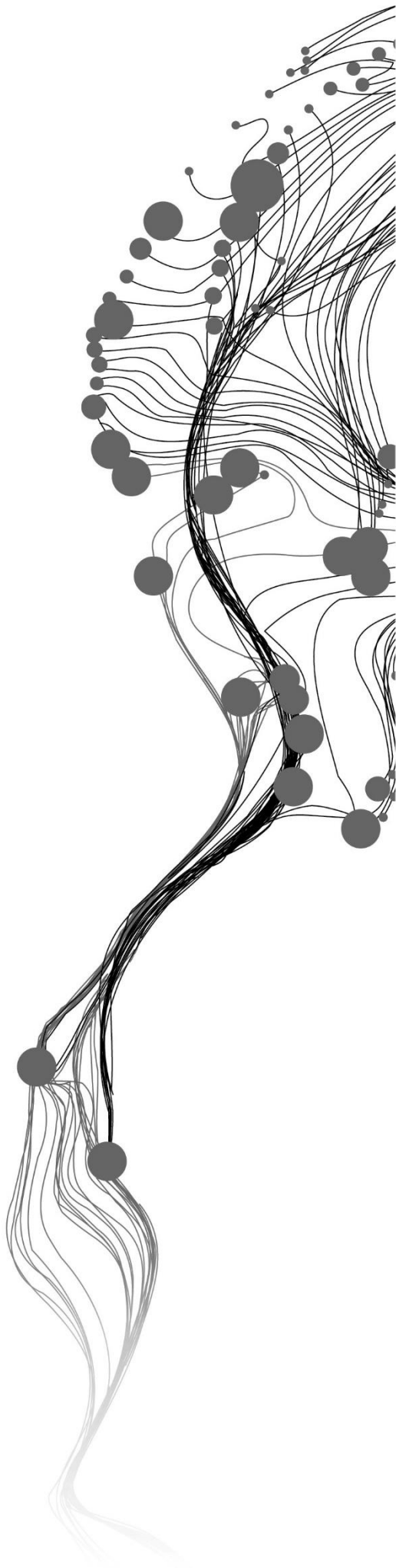
RANSFORD NII AYITEY WELBECK

August, 2021

SUPERVISORS:

Dr. Ing., T.H.M, Rientjes

Ir., G.N., Parodi



ASSESSING THE EFFECTS OF SEA LEVEL RISE ON URBAN FLOODS, A 1D2D SATELLITE- BASED FLOOD INUNDATION MODELLING APPROACH IN ACCRA COASTAL ZONE

RANSFORD NII AYITEY WELBECK

Enschede, The Netherlands, August, 2021

Thesis submitted to the Faculty of Geo-Information Science and Earth Observation of the University of Twente in partial fulfilment of the requirements for the degree of Master of Science in Geo-information Science and Earth Observation.

Specialisation: Water Resources and Environmental Management

SUPERVISORS:

Dr. Ing. T.H.M, Rientjes

Ir. G.N. Parodi

THESIS ASSESSMENT BOARD:

Dr. Ir C. van der Tol (Chair)

Dr. Alemseged Haile (Arba Minch University Ethiopië)

DISCLAIMER

This document describes work undertaken as part of a programme of study at the Faculty of Geo-Information Science and Earth Observation of the University of Twente. All views and opinions expressed therein remain the sole responsibility of the author, and do not necessarily represent those of the Faculty.

ABSTRACT

Accra, Ghana's regional capital, has experienced devastating impacts of urban floods since the late 1930s. The recurrent flooding of the coastal urban area of the Densu River Basin is an example of such events. The findings of a prior study of the area identified the upstream reservoir spillage and the backwater effect as a result of coastal water intrusion as the cause of the floods. The rapid unplanned urbanisation, the operation of the Weija reservoir and sea level rise make this low-lying coastal zone susceptible to severe flooding in the future. Therefore, the objective of this study was to evaluate the likely impacts of sea level rise by climate change on the recurrent floods in the area. The study employed hydrodynamic modelling to simulate flow processes in the area to achieve the study objective. Due to the lack of field observed data on recent inundations, satellite-based surface water maps were tested to serve model calibration. SAR and optical satellite images, namely Sentinel-1 and PlanetScope images, were sourced to produce surface water maps of a flood event that occurred in 2017. The Edge Otsu algorithm, an automatic threshold-based algorithm that integrates the Canny edge detection method, was applied to map surface water bodies in the satellite images. The surface water mapping operations were executed using Google Earth Engine (GEE), the GEE python API and the HYDRAFloods open-source python package. Surface water bodies in the Sentinel-1 images were mapped using the VV polarization bands. NDWI maps were computed using the green and near-infrared bands of the PlanetScope image to detect surface water bodies before applying the unsupervised surface water mapping algorithm chosen for the study. The evaluation of the surface water maps produced in the study was performed using visual inspection and the metrics, namely, the overall classification accuracy and Kappa coefficient. The overall classification accuracy recorded for the maps ranged from 84.16% to 90.10%, with Kappa coefficients also ranging from 0.69 to 0.80. With the aim of improving the satellite-based surface water maps produced from the individual images, the feature-level image fusion method was applied to fuse the SAR and optical satellite images using the random forest classifier. Overall classification accuracies of 97% and 98% with Kappa coefficients of 0.93 and 0.97 were achieved for the two fusion operations executed. Despite the results of the quantitative assessments performed, some causes of uncertainties were identified within the maps. Misclassification of water pixels was identified in the surface water maps produced from the optical images, while the maps produced from the SAR images showed dry patches along the course of the river channel. The cause of the former was attributed to the similarities of NDWI values of regions covered with water and built-up areas, while the latter was due to vegetation along the river channel. The schematization of the 1D2D SOBEK hydrodynamic model was designed to account for tidal behaviour at the downstream end of the model domain. Model tests performed proved that the model was able to replicate real-world flow processes affecting inundations in the study area. An attempt was made to calibrate the 1D2D SOBEK hydrodynamic model by means of the satellite-based surface water maps, and the corresponding model simulated inundation extents. The comparison results were not satisfactory, and as such, the model could not be calibrated. The assessment of the impacts of sea level rise on the flooding in the model domain was executed by comparing inundation area and average water depth of two scenarios with the flood event of 2017. These scenarios were based on the sea level rise projections for the years 2060 and 2100 that were obtained from literature. Overall, the results revealed that the inundation area at the downstream section of the model domain increased in all the scenarios. Also, the average water depth of the two scenarios also increased when compared to the flood event of 2017.

Keywords: PlanetScope, Sentinel-1, Edge Otsu, NDWI, 1D2D hydrodynamic model, SOBEK, surface water map, simulated inundation extent.

ACKNOWLEDGEMENTS

Thank God for life and the opportunity to undertake this master's programme and for all the memories I have made during this period. Also, for the strength and the will to never give up no matter what. I am grateful to my parents, Nii Osai Welbeck and Gladys Quarcoo, for all the encouragement and support. I am forever indebted to you, and I do not take your selfless sacrifices for granted. To my siblings, Vanessa Welbeck and Samuel Welbeck, thank you very much for believing in me.

My study here in the Netherlands would not have been possible without the opportunity given to me by the ITC Foundation Scholarship. I would like to express my most profound appreciation to the foundation and the management of ITC for enabling me to achieve this milestone in my education and career.

My earnest appreciation goes to my supervisors for their support and advice throughout the research period. To Dr Ing. Tom Rientjes and Ir. Gabriel Parodi, I say thank you very much for all the vital comments and discussions. This thesis would not have been possible without your constructive criticism and guidance. You managed to impart your knowledge and experience to develop my research skills. Accept my endless gratitude.

To the Department of Water Resources and Environmental Management staff of ITC, especially the lecturers, I say thank you for all the knowledge I have gained.

I want to express my profound appreciation to Mr Hubert Osei Wusu-Ansa (Director of the Hydrological Services Department of Ghana) for the mentorship, encouragement, and opportunity to further my education. Thank you, Director, for everything you have done for me.

I cannot forget the immense support from the Ghanaian community here at ITC. I am very grateful to you all for being part of this journey. To Prince, Eunice, Yusif, Letticia, Adwoa, Rexford, Efia, Mavis, and Derrick, thank you is an understatement; you guys are amazing.

To Anna Ennin, I cannot repay your invaluable support throughout this period. I am grateful for all the encouragement.

To everyone who has been part of this phase of my life, thank you. You are very much appreciated.

TABLE OF CONTENTS

1.	INTRODUCTION.....	1
1.1.	Background.....	1
1.2.	Problem Statement.....	2
1.3.	Research Objectives.....	3
1.4.	Research Questions.....	3
1.5.	Thesis Outline.....	3
2.	LITERATURE REVIEW.....	4
2.1.	Satellite-based Surface Water Mapping.....	4
2.2.	Sensor Approaches.....	4
2.3.	Optical Satellite-Based Surface Water Detection and Mapping Approaches.....	6
2.4.	SAR Satellite-Based Surface Water Mapping Approaches.....	8
2.5.	Combined Optical and SAR Satellite-Based Surface Water Mapping Approaches.....	9
2.6.	Evaluation of Surface Water Maps.....	11
2.7.	Conclusion of Literature Review.....	13
3.	STUDY AREA AND DATASET.....	15
3.1.	Description of the study area.....	15
3.2.	Dataset.....	16
4.	METHODOLOGY.....	20
4.1.	Surface Water Mapping.....	20
4.2.	Hydrodynamic Modelling.....	30
4.3.	Sobek Model Setup and Schematisation.....	30
4.4.	Tidal data referencing.....	33
4.5.	Model Testing.....	34
4.6.	Sensitivity Analysis.....	35
4.7.	Surface Roughness.....	35
4.8.	Model Calibration.....	35
4.9.	Model Simulation with Sea Level Rise Projections.....	36
5.	RESULTS AND DISCUSSION.....	38
5.1.	Surface Water Mapping.....	38
5.2.	Hydrodynamic Modelling.....	57
6.	CONCLUSION AND RECOMMENDATION.....	69
6.1.	Conclusion.....	69
6.2.	Recommendation.....	72

LIST OF FIGURES

Figure 2-1: An optical satellite image partly covered with clouds (Source: (“Copernicus: Sentinel-2 - Satellite Missions - eoPortal Directory,” n.d.))	5
Figure 2-2: Speckled and speckle-free SAR images (Source: (“Speckle Filtering Pada Synthetic Aperture Radar - Bagas Setyadi,” n.d.))	6
Figure 2-3: Image fusion methods a) pixel-level image fusion b) feature-level image fusion c) decision-level image fusion (source: Liu et al. (2018)).....	10
Figure 3-1: Map of the Densu River Basin and the selected model domain and a section of the Densu Delta Wetland	15
Figure 3-2: Tidal data comparison.....	16
Figure 4-1: Description of the Edge Otsu algorithm demonstrated in the study of Markert et al. (2020)...	21
Figure 4-2: Sentinel-1 surface water mapping workflow	22
Figure 4-3: PlanetScope surface water mapping workflow	25
Figure 4-4: Diagram explaining the HAND development process as executed in the study by Rennó et al. (2008).....	27
Figure 4-5: HAND creation flowchart	28
Figure 4-6: Feature-level satellite image fusion approach used to fuse the Sentinel-1 and PlanetScope satellite images.....	30
Figure 4-7: An example of a 2D line boundary configuration adapted from Deltares (2018).....	31
Figure 4-8: 1D2D SOBEK hydrodynamic model schematisation of the model domain	33
Figure 4-9: Diagram showing the referencing of the average tidal height to the lowest elevation of the DEM where the 2D line boundary was installed	34
Figure 5-1: Sentinel-1 RGB composites images of floods (a) SF25JUN17 (b) SF07JUL17	39
Figure 5-2: Image histograms of the Sentinel-1 flood images (captured on 25/06/2017 & 07/07/2017) and the dry-weather flow image (captured on 24/12/2019).....	40
Figure 5-3: Sensitivity analysis performed on surface water maps produced from SF25JUN17	41
Figure 5-4: Surface water maps of the model domain based on the Sentinel-1 flood images.....	42
Figure 5-5: Surface water map of the Densu Delta Wetland based on the dry-weather condition captured by the Sentinel-1 SAR satellite image.....	43
Figure 5-6: NDWI maps of the PlanetScope flood images used in mapping surface water within the model domain.....	45
Figure 5-7: Spectral reflectance signatures of different compositions of water adapted from (ITC, 2013).46	
Figure 5-8: Surface water maps of the model domain based on the PlanetScope flood images.....	49
Figure 5-9: Surface water map of the Densu Delta Wetland based on the dry-weather condition captured by the PlanetScope optical satellite image	50
Figure 5-10: Map of HAND filter created using the 10m resolution DEM.....	51
Figure 5-11: Filtered surface water maps of the model domain based on the Sentinel-1 flood images.....	52
Figure 5-12: Filtered surface water maps of the model domain based on the PlanetScope flood images ...	53
Figure 5-13: Surface water map of the Densu Delta Wetland based on the fusion of the Sentinel-1 and PlanetScope dry-weather flow images.....	55
Figure 5-14: Surface water maps of the model domain based on the fusion of the Sentinel-1 and PlanetScope flood images	56
Figure 5-15: Maps showing the simulated inundation extents and water depths during low and high tides without inflow discharges	57

Figure 5-16: Maps showing the simulated inundation extents of low and high inflow discharges without tidal intrusion.....	58
Figure 5-17: Maps showing the simulated inundation extents and water depths of low and high inflow discharges and tidal intrusion.....	59
Figure 5-18: Scatter plots of the sensitivity analysis results	60
Figure 5-19: Simulated inundation extents	62
Figure 5-20: Maps showing the comparisons made between satellite-based surface water maps and simulation inundation extents.....	64
Figure 5-21: DEM used for creating the 2D grid in the 1D2D SOBEM hydrodynamic model	65
Figure 5-22: Change in simulated inundation extent as a result of the sea level rise (SLR) projection of 2060.....	67
Figure 5-23: Change in simulated inundation extent as a result of the sea level rise (SLR) projection of 2100.....	68

LIST OF TABLES

Table 2-1: Spectral Indices.....	8
Table 2-2: Metrics for assessing the accuracy of surface water maps used in Notti et al. (2018).....	13
Table 3-1: Description of the satellite data collected for the study.....	17
Table 3-2: Description of the Sentinel-1 data obtained for the study	18
Table 3-3: Description of the PlanetScope Analytic Ortho Tile Product (source: (Planet Labs, 2021))	19
Table 4-1: Manning’s roughness coefficient values adapted from Medeiros et al. (2012).....	35
Table 4-2: Contingency table adapted from Grimaldi et al. (2016).....	36
Table 4-3: Information on performance measure used for the inundation extent comparisons adopted from Grimaldi et al. (2016).....	36
Table 5-1: Comparison of Sentinel-1 surface water maps and water masks.....	40
Table 5-2: Pixel-by-pixel assessment of spectral reflectance values in the PlanetScope flood images.....	47
Table 5-3: Comparison of the PlanetScope surface water maps and water masks.....	48
Table 5-4: Results of the inundation area comparisons	61
Table 5-5: Results of the satellite-based surface water maps and simulated inundation extent comparisons	63

1. INTRODUCTION

1.1. Background

Natural disasters and hazards pose severe challenges to the economic growth and stability of many developing countries in Africa (Okyere, Yacouba, & Gilgenbach, 2013). The most recurrent and devastating of them is flooding. Floods have affected populations and their means of survival all across the continent of Africa. Such events have led to impacts that have caused interruptions in energy, water supply, communication, and transportation. Many people have been displaced, whilst others have suffered from health-related problems as a result of flood events. Ghana's history with floods has hindered the socioeconomic development of the country to some extent. Nearly 3.9 million people were affected by floods, out of which 409 people lost their lives between 1968 and 2014 (Asumadu-Sarkodie, Owusu, & Jayaweera, 2015). Documented damages incurred from June 2015 to June 2016 were estimated to be over 108 million dollars (Tengan & Aigbavboa, 2016). Floods have been causing significant damage in Ghana since 1995, predominantly in coastal regions (Douglas et al., 2008).

Accra is Ghana's capital city as well as the capital of the Greater-Accra Region, making it the country's administrative centre. This coastal city serves as the locus for the majority of the nation's administrative, political, and commercial activities and has a population of about 2.557 million (CIA Factbook, 2021). Accra's flooding issues extend back to the late 1930s, when the city began to develop (Karley, 2009). The floods in Accra have become recurrent with increasing levels of damages. In over a decade, the city experienced its worst tragedy on the 3rd of June, 2015, when a flood accompanied by an explosion at a fuel station killed over 152 people (Asumadu-Sarkodie, Owusu Phebe, & Rufangura, 2015). Accra's situation has proven that urban flooding is a demanding and evolving developmental challenge. Moreover, the triggers of urban floods are changing with aggravating effects and thus, with population growth, urbanisation patterns, and climate change, the hazards posed by such floods may be intensified.

Urban coastal zones such as Accra are vulnerable areas with increasing flood risks due to the effects of the changing climate, sea level rise and urbanisation of low-lying coastal zones. The warming of the ocean, melting of glaciers and ice sheets are the factors causing sea levels to rise. The destructive impacts of sea level rise on urban coastal areas have attracted interest from researchers, governments, and the media, to mention a few. An example of an impact of sea level rise is coastal flooding. Coastal floods are a result of high sea levels driven by combinations of factors such as high tides and storm surges. A report represented by the German Federal Ministry for Economic Cooperation and Development (2019) documented that Ghana's mean sea level is anticipated to rise by 39 cm by the year 2080. This indicates threats to urban coastal communities such as the downstream area of the Densu River basin as expected sea level rise may exacerbate the frequency and severity of the perennial flooding that already affects the area. To address this challenge, it is vital to investigate new ideas and ways that may be implemented into current systems, if any exists.

Knowledge of historical floods, future flood scenarios, and identifying areas that have a high vulnerability of being inundated are essential for the effective management of floods (Ekeu-wei & Blackburn, 2018). Water flow simulation by hydrodynamic models has been extensively utilised to evaluate the dangers of floods for many years (Pasquier et al., 2019). These models compute water flow by applying numerical

equations and are built with the knowledge of a domain's hydrodynamic processes. Consequently, these models require hydrometric and topographic data of a basin for simulations. Moreover, detailed data on flow conditions in a basin, the geometry of the river channels and accurate representation of the basin's terrain are imperative to obtain accurate results. Such datasets are conventionally collected in the field and are usually desired to have high spatial and temporal resolutions in order to reduce model uncertainties.

1.2. Problem Statement

The downstream area of the Densu River Basin has been affected by recurrent floods with increasing hazards over the past few decades. According to Owusu-Ansah et al. (2019), the flooding of the area may as well be influenced by factors such as inadequate stormwater drainage system, urbanisation of low lying terrain and the increasing failure of authorities and construction developers to adhere to planning regulations. The distressing impacts of the floods, which often result in economic hardship among residents, include health-related problems and damage to properties. The rising cost of emergency relief items for flood victims has become an annual expense to governmental and non-governmental organisations. The findings of the study by Addae (2018) indicated flow releases from the Weija reservoir and the backwater effect by coastal water intrusion as the two elements causing the periodic inundation of the coastal zone. These causes, together with sea levels projections due to climate change, may cause frequent and severe inundations. Hence, the constant reservoir operations, the rate of urban expansion and the potential effects of sea level rise reinforce the need to study this coastal urban area's hydrodynamic processes and assess the possible flood damage.

The analysis of an extreme flood event in the area using hydrodynamic modelling is essential. This can serve as a foundation to assess future floods scenarios to gain insights into potential future impacts, which will be invaluable, especially to planners and landowners in the region. However, setting up such flood models require extensive data that is often not available in Ghana. Most basins in Ghana have scarce data owing to data collection constraints caused by the lack of funding and logistics. As a result, monitoring and management of hydrological stations are not prioritised. Also, for simulation results of hydrodynamic flood models to be meaningful to society, these models ought to be calibrated (Karim et al., 2011). Therefore, to perform accurate and detailed flood analysis in the downstream area of the Densu River basin, it is imperative to set up a hydrodynamic model for the area and calibrate it. However, due to the limited data in the basin, an alternative data source is vital.

Remote sensing can serve as an alternative data source to overcome the limitations of flood modelling in this data-scarce basin. In recent times, the evaluation of inundation extents using remotely sensed data has been given attention (Wang, 2015) and as such, flood mapping can be performed using well-documented methodologies (Notti et al., 2018). This also is due to the accessibility of open-source remote sensing data. Optical and radar sensors on satellites and aircrafts have supplied necessary data for inundation extent mapping, damage evaluation and flood modelling for the past few decades (Klemas, 2015). Nevertheless, optical remote sensing is hindered by clouds, which are common during floods (Shen, Wang, Mao, Anagnostou, & Hong, 2019). In comparison with optical sensors, the core advantage of synthetic-aperture radar (SAR) sensors is evident in the ability of these sensors to acquire data during the day, night and under any atmospheric condition, thus eliminating the effects of cloud cover (Notti et al., 2018). However, the roughening of water surfaces by wind, vegetation and man-made structures such as tall buildings make flood mapping in forested, vegetated, and urban areas difficult (Giustarini et al., 2013; Pulvirenti, Chini, Pierdicca, & Boni, 2016). Also, backscatter intensities in SAR imagery is not a unique indicator and could indicate different surface properties.

Insufficient flood extent data needed for calibrating flood models in the Densu River basin necessitates the use of remote sensing data. However, the inherent characteristics of the two satellite data types, together with atmospheric and land surface conditions, affect the accuracy of satellite-based inundation mapping. Also, advanced hydrodynamic flood model calibration with satellite-based flood extent mapping has not been examined routinely in Ghana and the basin. A first attempt at calibrating a hydrodynamic model using satellite-based inundation extents was shown by Addae (2018). This study extends on the study by Addae (2018) and seeks to improve the 1D2D SOBEK hydrodynamic flood modelling and to assess impacts due to sea level rise by climate change.

1.3. Research Objectives

The main objective of this study is to assess the potential effects of sea level rise by climate change on flooding in the coastal urban area of the Densu River basin using hydrodynamic modelling, satellite-based flood mapping and sea level rise projections by climate change.

1.3.1. Specific objectives

Below are the specific objectives of the study.

- To evaluate the performance of optical and SAR satellite imagery in mapping flood extent.
- To perform satellite-based flood mapping by merging optical and SAR images.
- To set up a 1D2D hydrodynamic model to simulate inundation extents as affected by tidal behaviour.
- To compare the model simulated flood extent with a merged satellite-based flood extent.
- To assess the calibration of a 1D2D hydrodynamic model with a merged satellite-based flood extent.
- To assess how sea level rise affects flood extent and water depth.

1.4. Research Questions

The following are research questions that follow up on and relate to the study objectives:

- What accuracy can be achieved by mapping surface water bodies with optical and SAR imagery?
- What method can be exploited to effectively delineate urban inundation from merged optical and SAR based satellite images?
- How effectively can tidal intrusion be simulated in a 1D2D SOBEK hydrodynamic flood model?
- What performance index can be applied to assess the fit between the merged satellite-based flood extents and the model simulated flood extent?
- What are the setbacks in calibrating a 1D2D SOBEK hydrodynamic flood model using satellite-based inundation extent?
- How is inundation extent affected by sea level rise?

1.5. Thesis Outline

The thesis is structured in six chapters. Chapter one presents the introduction, which consists of the background, the problem statement, and the objective of the study. A review of literature examining the methods applied and previous studies performed that are related to this study are provided in chapter two. Chapter three contains information on the study area and the datasets used. The methods employed to achieve the objective of the study are described in chapter four. The results of the study and the discussions of the outcomes are presented in the fifth chapter. Chapter six contains the conclusion of the study and the outlined recommendation made regarding future studies.

2. LITERATURE REVIEW

2.1. Satellite-based Surface Water Mapping

Satellite-based surface water body mapping concerns the detection and mapping of surface bodies, including lakes, rivers, floods, and water intrusion at coastal zones. A literature review for this MSc study showed that such applications mostly were performed to observe changes in lake size due to seasonal effects as a result of changes in lake inflows and outflows. Satellite-based principles to map water bodies, and to assess accuracy, have unified validity and as such, mapping procedures and techniques can be applied to any open water body. As such, this literature review targets to present commonly used mapping techniques and satellite data sources with the objective to develop a procedure to map flood extent in the coastal flood zone of the Densu River basin in Accra. The review aims to identify satellite products, evaluate mapping principles, identify water surface indicators, and identify performance indicators that indicate the accuracy of mapping with reference to field observations. In Chapter 3 of this thesis, a holistic approach covering all steps involved in satellite-based surface water body mapping will be proposed based on this review.

2.2. Sensor Approaches

Remotely sensed data offers an inexpensive means of mapping surface water on a large scale. Consequently, satellite images are fast becoming the fundamental source of data for surface water studies and water resources monitoring and management across the world. Surface water body mapping can be performed using optical and radar-based satellite imagery. Optical images are characterised by infrared-based observations, which are direct and unique in observing wet surfaces, but the use of such imagery is hampered by atmospheric conditions (i.e., cloud cover). Furthermore, optical sensors are mounted on geostationary satellites, and as such, observations are commonly available at high temporal resolutions. However, factors such as spatial resolution, water extraction approach, and image acquisition time determine the accuracy of mapping surface water bodies with optical satellite imagery. Surface water maps produced from optical satellite images with high spatial resolution have shown better accuracies (i.e., when compared to ground truth data) as compared to coarse spatial resolution images. The poor performance of low spatial resolution optical satellite images can be attributed to the high level of data generalisation. Other factors that affect optical satellite-based surface water detection and mapping include mixed or diffused pixels containing a mixture of land cover types, for example, a pixel containing water and vegetation probably due to emergent or floating vegetation. There is also the problem of detecting the edges between water and land accurately.

Notti et al. (2018) mapped flooded regions in the Arahalin and the Ebro River Valley in Spain as well as the Po and Tanaro plains in Italy using MODIS, Proba-V, Landsat, and Sentinel-2 images. According to the study's findings, over 90% of the 2015 Ebro floods was successfully mapped using optical satellite imagery captured during the event. Furthermore, the flood map produced using the imagery captured some weeks after the flood event in the Po and Tarano plains in 2016 recorded a flood ratio of under 50%, which the authors described as useful to track the trend of inundation. Using Landsat imagery spanning a period of 17 years, Ashtekar, Mohammed-Aslam, & Moosvi (2019) studied the surface water dynamics in the parts of India's Upper Krishna River basin. From the study results, the basin's surface water showed an overall increase from an area of 132.47 km² to 140.84 km² during the period (1999 - 2016) of analysis, although 2003 recorded the lowest surface water coverage. Bhaga, Dube, & Shoko (2020) evaluated Sentinel-2 and Landsat 8 in monitoring temporary surface water bodies in the Cape

Winelands and Overberg regions in the Western Cape of South Africa. The study's findings revealed that both satellite images used were able to map surface water changes as less surface water was mapped during the dry season compared to the wet season. The authors reported that their findings proved the capability of utilising Sentinel-2 and Landsat 8 in studying the spatio-temporal changes of surface water bodies.



Figure 2-1: An optical satellite image partly covered with clouds (Source: (“Copernicus: Sentinel-2 - Satellite Missions - eoPortal Directory,” n.d.))

An alternative to optical imagery is radar-based satellite (i.e., SAR) imagery captured with signals that penetrate cloud systems, and as a result, data acquisition can practically be made in any weather condition. Since SAR sensors are equipped with illumination sources, images can be captured both during the day and at night. This makes SAR images suitable for regions mostly covered by clouds and enables the continuous monitoring of surface water bodies. Some fundamental knowledge of how various land cover types interact with radar signals is necessary to interpret SAR imagery accurately. Regions covered by surface water bodies with smooth surfaces show almost perfect reflective scattering due to low surface roughness. As a result, radar signals incident on such surfaces are scattered away from the receiving antenna and consequently appear darker than other land cover types on SAR imagery. In principle, this allows for the differentiation of surface water bodies from other land cover types. However, factors such as wind that roughens the surfaces of water bodies, vegetation, and nearby structures such as walls and buildings affect the specular reflection of radar signals by smooth water. These mentioned factors cause water-covered regions to exhibit high radar backscatter returns comparable to dry regions instead of low returns.

Also, the side-looking nature of SAR sensors may result in some ground regions not being captured due to layover and foreshortening caused by features such as mountains, tall vegetation and buildings that cause shadows (Mason, Giustarini, Garcia-Pintado, & Cloke, 2014). This makes the use of SAR imagery in mapping surface water bodies in urban areas a challenge. SAR sensors are usually mounted on satellites in orbit, causing images to be available only at the satellite revisit time, commonly multiple days. Furthermore, SAR observations are indirect and not unique and require advanced image processing to differentiate wet pixels from dry or partly dry pixels. A typical example of an inherent SAR image interference that degrades the quality of SAR images is speckle. With regards to surface water mapping

using SAR imagery where clear and substantially coherent indications of regions covered with water are a priority (Refice, D’Addabbo, & Capolongo, 2018), speckle is deemed an irritant.



Figure 2-2: Speckled and speckle-free SAR images (Source: (“Speckle Filtering Pada Synthetic Aperture Radar - Bagas Setyadi,” n.d.))

Xing, Tang, Wang, Fan, & Wang (2018) produced surface water maps of the Dongting Lake using Sentinel-1 imagery to analyse the dynamic variations in the lake’s surface area at a monthly timestep. The study results showed that the VH polarisation band performed better than the VV polarisation band in mapping surface water within the study site. The Kappa coefficient and overall classification accuracy were above 0.88 and 94.50% for the VV polarisation band and above 0.90 and 95.50%, respectively, for the VH polarisation band. The authors attributed the performance of the VV polarisation band to the wind roughening of the lake. From the evaluation of the monthly surface water changes, Xing et al. (2018) stated that the area of the Dongting Lake increased in April but decreased in August of 2016. July was, however, the month in which the lake had the largest surface area, while December was the month to record the smallest surface area. Concerning working with SAR imagery, Notti et al. (2018) reported that the useful flood maps produced in their study were obtained from the Sentinel-1 satellite imagery captured during the floods as the flood ratio values recorded for the flood maps produced using imagery captured few days after the Po River flood event in 2016 were below 5%. Markert et al. (2020) mapped floods in the lower Mekong basin in Cambodia and the upper Irrawaddy River system of Northern Myanmar using Sentinel-1 satellite imagery. Using two different surface water mapping algorithms, the overall classification accuracy of the surface water maps produced from the VV polarisation bands ranged from 92% to 95% and recorded Kappa coefficients also ranging from 0.7999 to 0.8427. It was reported by the authors that, overall, the Sentinel-1 VV polarisation bands that were pre-processed through radiometric terrain correction performed better than the respective VV polarisation bands that were not. This review also refers to recent studies that indicate the advantages of fusing optical and SAR images to make the best use of both satellite products.

2.3. Optical Satellite-Based Surface Water Detection and Mapping Approaches

Many methods have been developed to delineate floods using optical satellite imagery. The most prominent ones include using classification algorithms to perform either unsupervised or supervised image classifications and the use of spectral reflectance information to compute a spectral index to detect and distinguish surface water bodies from other land cover types (Pan, Xi, & Wang, 2020).

The supervised image classification process categorises pixels of an image based on spectral information into specified classes. The method is executed by using information from identified spectrally homogeneous pixels, which are termed training samples. A pixel is placed in a particular class if it has the same spectral characteristics as the training samples used in defining the class. For this particular variant of image classification, before training samples are selected, knowledge of the reflectance of different land cover types present in the region of interest, the preferred number of classes and the appropriate classification algorithm to use is essential (Ashtekar et al., 2019). Training samples of each desired class are created to encompass a broad range of spectral reflectance variability that may exist on an image to enable a chosen classification algorithm to produce accurate results. Researchers have employed many classification algorithms to map surface water bodies. Notti et al. (2018) found the maximum likelihood and spectral angle methods as the best-performing ones for their study.

Among all the methods documented, the computation of spectral indices is the unsophisticated technique commonly used for detecting and mapping surface water bodies (Herndon, Muench, Cherrington, & Griffin, 2020). Although a number of the water indices have evolved over the years, notable ones have been documented. A few of the usually exploited spectral indices include the Tasseled Cap Wetness Index (TCW) (Crist, 1985; Crist & Cicone, 1984), which differentiates water from non-water surfaces by using a set threshold value of zero (0) and six spectral bands. Based on Landsat-4 (TM) data, the spectral bands include the red, green, blue, near-infrared (NIR) and the two (2) short-wave infrared (SWIR1 & SWIR2) bands (see Table 2-1). The study by Mishra & Pant (2020), in which the two variants of the TCW were compared to other spectral indices, highlighted the TCW introduced in 1985 (TCW₈₅) as the lowest-performing index followed by the TCW introduced in 1984 (TCW₈₄) based on the classification accuracy performed.

As proposed by McFeeters (1996), the Normalised Difference Water Index (NDWI) is used to delineate open surface water bodies by subtracting the NIR band from the green band and then dividing by the sum of the two bands (see Table 2-1). The index enhances the surface water bodies and suppresses non-water surfaces such as land and vegetation on optical satellite imagery. As a result, positive NDWI values indicate water, while NDWI values ranging from 0 to -1 indicate vegetation and soil. However, the spectral index is often impacted by noise from built-up areas due to the similar reflectance characteristics of built-up and water in the green and NIR bands. Consequently, built-up areas exhibit positive NDWI values, thereby causing overestimation of extracted surface water bodies. However, several studies have employed NDWI to map surface water (Ashtekar et al., 2019; Bhaga et al., 2020; Jiang et al., 2020). Bhaga et al. (2020) indicated that the index performed marginally better than other water indices used in their study. Ashtekar et al. (2019) concluded that NDWI is effective in surface water detection and mapping.

As developed with the aim of improving the NDWI, the Modified Normalised Difference Water Index (MNDWI) by Xu (2006) depicts water as positive values and other land cover types as values in the range of 0 to -1. As documented by Xu (2006), the index can effectively suppress and possibly eliminate the effects of built-up areas, soil and vegetation and is computed by replacing the NIR band with the middle infrared (MIR) band (see Table 2-1). The fact that not all optical satellite images have MIR bands is a drawback of applying the MNDWI. Studies such as Notti et al. (2018) and Ogilvie et al. (2020) applied the MNDWI in delineating temporary inundation.

Table 2-1: Spectral Indices

Spectral Indices	Equation
Tasseled Cap Wetness Index (Crist & Cicone, 1984)	$TCW_{84} = 0.1509 * Blue + 0.2021 * Green + 0.3102 * Red + 0.1594 * NIR - 0.6806 * SWIR1 - 0.6109 * SWIR2$
Tasseled Cap Wetness Index (Crist, 1985)	$TCW_{85} = 0.0315 * Blue + 0.1973 * Green + 0.3279 * Red + 0.3406 * NIR - 0.7112 * SWIR1 - 0.4572 * SWIR2$
Normalised Difference Water Index (McFeeters, 1996)	$NDWI = \frac{Green - NIR}{Green + NIR}$
Modified Normalised Difference Water Index (H. Xu, 2006)	$MNDWI = \frac{Green - SWIR}{Green + SWIR}$

Thresholding is a technique used to segment satellite images to create binary maps where the value one (1) indicates water while zero (0) indicates non-water features. A vital step in mapping surface water bodies using spectral indices is selecting an appropriate threshold value. This process can be challenging due to the variation in spectral reflectance of surface water bodies in different images. There is also the issue of the separation of the image histogram peaks and uneven image illumination. Thus, a single threshold value cannot be used for every optical satellite image. A wrongly selected threshold value results in the misclassification of non-water features as water. Threshold values can be selected empirically by analysing image histograms or automatically through the use of algorithms. Sipelgas et al. (2020) empirically selected and used an MNDWI threshold value of 0.6, while Jiang et al. (2020) employed Otsu's method to automatically determine the NDWI threshold value.

2.4. SAR Satellite-Based Surface Water Mapping Approaches

Several SAR surface water detection and mapping methods have been developed and documented in literature. The growing accessibility to SAR images with high spatial and temporal resolutions may be the reason for the field's progression. However, SAR surface water detection and mapping algorithms are challenging to construct, and solely automated algorithms that necessitate no human intervention are scarce (Shen et al., 2019). Some techniques include visual interpretation, histogram thresholding, change detection and active contour. Some studies have employed a combination of histogram thresholding and edge detection filters to map surface water bodies.

Possibly, due to the computational efficiency and potential of yielding results comparable to complex segmentation methods, histogram thresholding has been widely used by many researchers (Sipelgas et al., 2020; van Leeuwen, Tobak, & Kovács, 2020). The method is centred on the fact that surface water bodies have low radar backscatter. The essential aspect of using this technique is determining an applicable threshold value that yields optimum results. Empirical techniques of determining threshold values primarily depend on an operator's experience, resulting in a wide range of accuracy attributable to subjective assessment (Xing et al., 2018). The technique is simple if the SAR image has a bimodal histogram. However, the process is not straightforward if there is a significant noise or wind-induced surface roughness on a SAR image. Other methods of selecting a threshold value for segmenting SAR images into water and non-water image objects are automated and include Otsu's method. Otsu's method is a histogram-based global thresholding method that maximises the inter-class variance between two classes (background and foreground) to obtain an optimal threshold (Otsu, 1979). Although Otsu's method can generate sub-optimal outcomes if the image has more than two unique classes, the method

presupposes bimodality in image histograms. In the study by Sipelgas et al. (2020), the authors used an empirical approach to define the SAR images' threshold values.

The change detection method has been an efficient means of mapping inundated regions of multi-temporal SAR imagery. Such methods conventionally refer to comparing SAR backscattering intensities of in-flood or pre-flood and post-flood to detect variations caused by floods. This method prevents the over-detection of inundated regions since similar regions in both reference and flood images are lost in the final image. A division of change detection approaches that can be used for inundation delineation includes algebraic techniques of image differencing, ratioing and index differencing (Martinis et al., 2017). Image differencing and image ratioing are the two main methods exploited to acquire difference images in order to evaluate changes (Vaiyammal & Raja, 2017). Image differencing involves the pixel-level deduction of intensity values between selected temporal SAR imagery to assess changes. Image ratioing, on the other hand, involves the application of the ratio operator in a pixel-by-pixel manner to evaluate changes. The image ratioing method is usually applied instead of the image differencing method because it is adaptive to SAR imagery statistics (Ashok & Patil, 2014). Vanama, Rao, & Bhatt (2021) employed two change detection methods and a semi-automatic thresholding approach to detect and map floods.

The Edge Otsu algorithm is an approach that combines histogram thresholding and an edge detection filter. The Edge Otsu algorithm is automated and uses the Canny edge filter (Canny, 1986) to enable accurate delineation of surface water bodies. It carries out automatic satellite image segmentation by applying Otsu's method to produce surface water maps. The workflow of the Edge Otsu algorithm begins with the definition of an initial threshold value which is applied to generate a binary image. This procedure avoids detecting other land cover types present in satellite images, thereby enabling the delineation of only water and non-water edges. Edges in the binary images are detected with the application of the Canny edge filter. Subsequently, with a user-defined distance known as the edge length parameter, the detected edges undergo a filtering by length process which is performed to exclude tiny edges that can skew the histogram sampling. Thus, only edge elements greater than or equal to the user-defined length are deemed valid edges. Afterwards, using a user-defined distance known as the edge buffer parameter, buffers are then created around the extracted edges. Pixels within these buffers are sampled to create a histogram. The follow-up step involves the use of the created histogram to compute a threshold value using the Otsu's method. Finally, the threshold value is applied to the whole image, with pixel values greater than the threshold value being mapped as non-water while those lower than the threshold mapped as water. Markert et al. (2020) compared the Edge Otsu algorithm with another automated surface water mapping algorithm known method as the Bmax Otsu algorithm to map floods and reported that the Edge Otsu slightly performed better than the Bmax Otsu algorithm.

2.5. Combined Optical and SAR Satellite-Based Surface Water Mapping Approaches

In remedying the limitations of both optical and SAR satellite data, studies have investigated the use of combining multi-sensor images in mapping surface water bodies. This approach has enabled researchers to capitalise on the strengths of both data types. Optical images are known for their multispectral and spatial information (Mahyoub, Fadil, Mansour, Rhinane, & Al-Nahmi, 2019), while SAR images are almost not affected by any atmospheric condition. Therefore fusing these two data types results in a more informative composite image suitable for visual perception and computer processing (Ardeshir Goshtasby & Nikolov, 2007). The primary aim of this method is to obtain better and accurate water maps. Furthermore, image fusion methods can be used in merging multi-temporal images and images of different spatial resolutions.

The pixel-level, the feature-level, and the decision-level image fusion methods are three states of the art types of image fusion methods used to combine optical and SAR images (Liu et al., 2018). The pixel-level fusion method entails combining multiple co-registered and geocoded images into a single image with the goal of improving image object perception. For creating water maps, the fused image can be further processed using a suitable surface water detection and mapping technique. Compared to the pixel-level fusion method, the feature-level fusion method operates with images of higher degrees of processing. The fusion process is performed using extracted features such as textures, lines, and shapes extracted from the individual images. The findings of Zhang & Xu (2018) also revealed that, when compared to the other levels of image fusion, a considerable improvement of about 10% was achieved with the feature-level image fusion utilising the extracted features and the original images. The highest level of image fusion is the decision-level fusion method. The technique is based on creating a definitive decision due to the integration of multiple findings obtained from selecting the optimum results from more than one classifier (Roggen, Tröster, & Bulling, 2013). It enables the fusion of different outcomes from different processes or algorithms into a composite decision dataset.

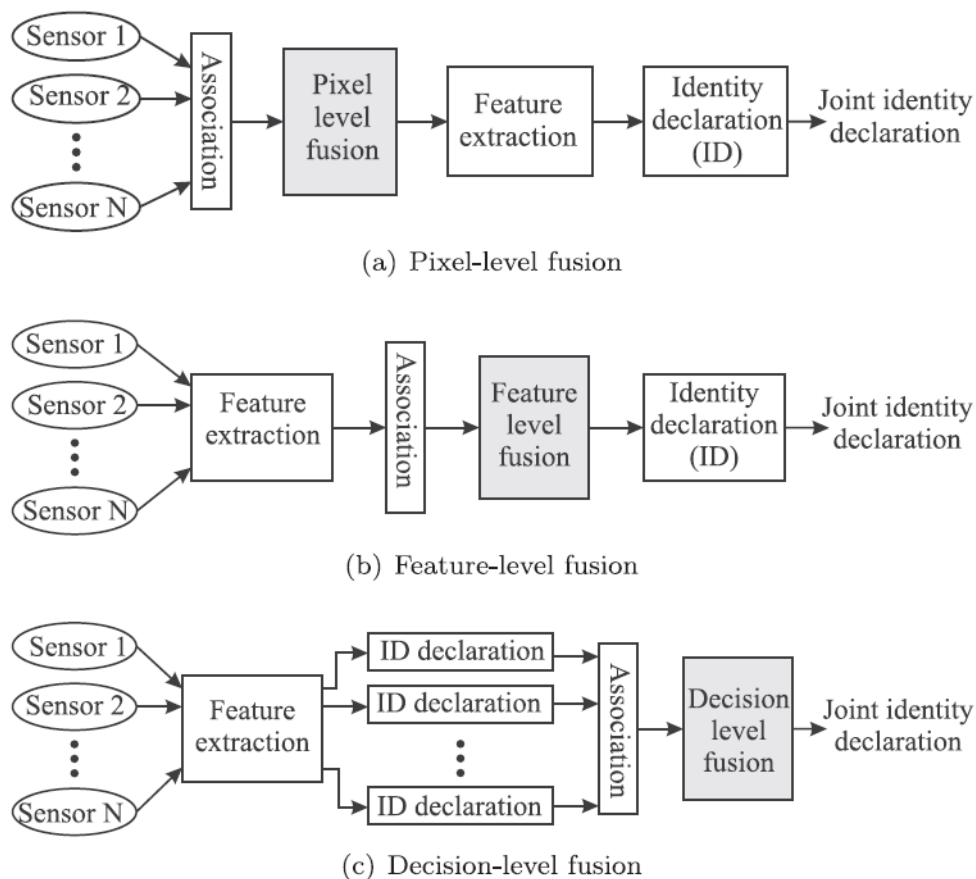


Figure 2-3: Image fusion methods a) pixel-level image fusion b) feature-level image fusion c) decision-level image fusion (source: Liu et al. (2018))

Using pixel-level image fusion methods, Landsat 8 and Sentinel-1 images were fused to improve image quality in the study by Quang et al. (2019). From the study results, the Gram-Schmidt Spectral sharpening method produced the best results against the other image fusion methods and was the least affected by cloud cover. However, comparing the output of the Gram-Schmidt Spectral sharpening method and the field survey map revealed an overestimation of water by 5.1%. The cause of the overestimation was

attributed to a number of factors, such as the difference in dates of the captured Sentinel-1 image and the field survey map.

In the study of Irwin, Beaulne, Braun, & Fotopoulos (2017), the feature-level fusion method was employed to fuse WorldView-2 imagery and TerraSAR-X imagery. The study also involved the use of an airborne light detection and ranging (LiDAR) digital elevation model (DEM) in the fusion process. The fused water map was created based on the concurrence of each pixel in all the images. The study's findings revealed that the uncertainty of any of the single-image techniques was higher than that of the uncertainty of the fused water map though the LiDAR, optical and SAR were obtained in separate seasons. The fused water map's uncertainty ranged from 4%-9%, while that of the single polarisation SAR water maps had an uncertainty range of 17%-20%. Moreover, the trends observed in the study revealed that through time all datasets were consistent in areas of open surface water and fields. The shorelines and wetlands exhibited more inconsistencies of pixels across all the datasets. Also, the LiDAR DEM used was imperative in reducing shadows and layover effects that tend to overestimate inundation extents in SAR flood imagery. Bioresita, Puissant, Stumpf, & Malet (2019) investigated the potential of fusing multi-temporal Sentinel-1 and Sentinel-2 images by applying the decision-level fusion method to improve surface water delineation. The study results indicated that the fused product of the Sentinel-1 and Sentinel-2 images recorded a higher accuracy for permanent surface water delineation as compared to the single image method. Furthermore, the time-series images used enabled an improved detection of temporary surface water and permanent surface water and underlined the possibilities of studying surface water dynamics. Sentinel-1 and Sentinel-2 images were fused using the feature-level fusion method by Tavus, Kocaman, Nefeslioglu, & Gokceoglu (2020) to detect and map floods in Turkey's Ordu Province. The study's methodology involved the co-registration and stacking of extracted image features as well as the Sentinel-1 and Sentinel-2 imagery bands for supervised classification with a random forest classifier. Three scenarios were executed to investigate the best performing fusion. These included the use of only the VV and VH polarisation bands for the initial scenario, followed by the VV, VH and spectral indices and lastly, the VV, VH, spectral indices and the original bands of the Sentinel-2 imagery. As reported by the authors, out of the three scenarios evaluated, the map produced from the fusion of Sentinel-1 and Sentinel-2 bands with the spectral indices computed from the Sentinel-2 imagery performed best. The study results indicated the approach's applicability in mapping flood regions effectively.

2.6. Evaluation of Surface Water Maps

Accuracy assessments refer to the procedures used in comparing remote sensing outputs with geospatial data that is regarded as ground truth. The quality of satellite-based surface maps is determined through such assessments. These assessments are crucial to surface water body detection and mapping since the results of these assessments verify the validity and influence the usefulness of the derived information. Such evaluations may be carried out applying either qualitative or quantitative approaches. Qualitative assessments are typically performed by comparing the satellite-based map and field conditions to observe similarities and disparities. A typical example is visual inspection. Although this method can evaluate satellite-based surface water maps, it is insufficient and generally improper to make conclusions about the quality of surface water maps based on this assessment. Quantitative assessment, on the other hand, is the comparison of satellite-based maps and field observed data to quantify how well the two fit.

The construction of a confusion matrix is a critical component of a quantitative accuracy assessment. As an effective means of representing accuracy, an error matrix is a square array of numbers arranged in rows and columns that expresses the number of pixels assigned to a certain class compared to the actual class

obtained from the reference data (Congalton, 2001). In the error matrix, the reference data are generally presented in columns, while the satellite-based classes are presented in rows. The computation of several accuracy metrics is possible with the use of confusion matrices. The overall classification accuracy, which is probably the most straightforward accuracy metric, essentially provides information on the correctly mapped proportions of the satellite-based surface water maps. As a percentage, the metric is computed by dividing the total correctly mapped pixels and the total of the pixels in the error matrix. An overall classification accuracy of 100% indicates that all reference data points (pixels) were correctly mapped. Another approach that uses error matrices to compute values that express the quality of satellite-based surface water maps is the Cohen's kappa coefficient (K) by Cohen (1960). This commonly used metric is a statistic employed to test the inter-rater reliability as well as the intra-rater reliability of categorical data (McHugh, 2012). Inter-rater reliability in statistics is a score that defines the degree of agreement or the homogeneity among several raters. In essence, it shows how accurate the satellite-based surface water map represents the reference data collected from the field or a tangible source. Even though likely K values range from +1 to -1, K ranges typically between 0 and 1. K value of 1 indicates a perfect agreement between the reference data and the satellite-based surface water map. As per the categorisation by Landis & Koch (1977), K values greater than 0.80 indicate a strong agreement while values lower than 0.40 indicate poor agreement. K values in the range of 0.40 and 0.80 signify a moderate agreement.

Many studies on surface water body mapping have employed different metrics for assessing the accuracy of the derived surface water maps. An example is a study performed by Notti et al. (2018) in which Flood Ratio (flood-mapping ratio (FR) and not flood ratio (NFR)) and official flood maps (reference data) were used to evaluate the quality of the satellite-based flood maps created. Permanent surface water bodies were not considered in the accuracy assessments to ensure a more consistent comparison strategy. After crossing each of the satellite-based surface water maps with the raster of the reference data, four outcomes, namely, true positive (TP), false positive (FP), false negative (FN) as well as true negative (TN), were obtained. The flood-mapping ratio was computed in the study by dividing the true positive (TP), which denotes the number of correctly mapped flooded pixels by the sum of the TP and the false negative (FN), which is the number of pixels that were flooded but mapped as dry. The not-flood ratio was also computed by dividing the true negative (TN), which denotes the number of correctly mapped dry pixels by the sum of the TN, and the false positive (FP), which is the number of pixels that were dry but mapped as flooded (see Table 2-2). FR and NFR were expressed in percentages, with 100% indicating the highest accuracy while a percentage of 0 indicates the lowest accuracy. Xing et al. (2018) quantitatively assessed the accuracy of satellite-based surface water maps using metrics such as overall classification accuracy and Kappa coefficient. The authors collected validation samples using stratified random sampling from Landsat 7, Landsat 8, and Google Earth images of the same month as the satellite images used for deriving the surface water maps. The validation samples were categorised into two classes: water and non-water, which included land cover types such as buildings, marshes, and farms. Markert et al. (2020) performed accuracy assessments on satellite-based flood maps using user-interpreted samples collected from PlanetScope imagery and metrics, namely, overall classification accuracy and Cohen's Kappa coefficient.

Table 2-2: Metrics for assessing the accuracy of surface water maps used in Notti et al. (2018)

Flood Ratio	Equation
Flood-mapping ratio	$FR (\%) = \frac{TP}{TP+FN} * 100 \%$
Not-flood ratio	$NFR (\%) = \frac{TN}{TN+FP} * 100 \%$

2.7. Conclusion of Literature Review

Satellite images have offered the means to cost-effectively map surface water bodies over the years. Due to the simple methods available to map floods on optical satellite images, researchers have documented many studies on surface water detection and mapping across the world. These studies have applied different methods and have produced variable results and accuracies based on the nature of the study site as well as the shape and size of the surface water body being studied. However, cloud cover has been a major limitation of employing optical satellite imagery for most mapping exercises. This has hindered the continuous monitoring of surface water bodies in regions periodically and heavily covered by clouds for major parts of the year.

Consequently, SAR images have been sourced as substitutes, and as a result, many SAR surface water mapping methods have been recorded in papers. This is due to the cloud penetrating ability of radar signals and the fact that SAR sensors can acquire images of the earth's surface in the day and at night. However, SAR images are affected by speckle and shadows caused by layovers due to the angle at which SAR sensors are tilted. This has made mapping surface water bodies on SAR images a complex task since SAR images require more elaborate processing as compared to optical images. Furthermore, the most accurate and effective method for mapping surface water was not highlighted in any of the studies reviewed due to the variable degrees of performance and the different test sites.

To improve the quality of images and thus improve the accuracy of satellite-based surface water maps, studies have fused the two satellite image data types to capitalise on their strengths. Researchers have published results indicating improvements in satellite-based surface water maps using image fusion approaches as compared to the results produced by single image studies. Such studies have highlighted the importance of multi-sensor surface water body mapping. Moreover, although using a single satellite image has made it possible to study specific instances in time, multiple images are vital for examining dynamic system conditions. This approach enables surface water bodies such as floods to be accurately studied. Since surface water maps mostly are used in decision making, it is paramount to evaluate the usefulness of such maps to make informed decisions and base decisions on accurate results. Determining the accuracy of satellite-based surface water maps is an essential step to ascertain the reliability of the maps. Two known ways, namely, qualitative and quantitative assessments, have been documented in literature. These methods are dependent on the aim of the study as well as the availability of ground truth data.

For this study, possible optical satellite imagery that can be considered for surface water mapping include Sentinel-2, Landsat 8, PlanetScope and MODIS. SAR images that can be employed included Sentinel-1, TerraSAR-X and COSMOSkyMed images. These satellite images have been used in many studies and have produced plausible results. However, since there is free access to Sentinel-2, Landsat 8 and Sentinel-1 images, these satellite images have been highlighted for the study. Although MODIS images are also freely accessible, the coarse spatial resolution of MODIS images may introduce errors in satellite-based surface

water maps. Also, since the edges of surface features are represented well in high-resolution images, MODIS images are unfit for the study. The other rejected datasets, although commercial, will serve as alternatives in case none of the earlier highlighted images for the study was captured during the identified study windows.

As demonstrated in the study by Markert et al. (2020), the Edge Otsu algorithm will be used for inundation detection and mapping. The algorithm can be used on both optical and SAR satellite imagery. Moreover, the algorithm's potential to accurately map the edges of surface water bodies where mixed pixels of different land cover types are often found makes it a plausible choice and method for the study. In the case of the optical images, the normalised difference water index (NDWI) by McFeeters (1996) or modified normalised water index (MNDWI) by H. Xu (2006) will be used to detect water and non-water classes, after which the outcome of the water index will then be processed using the Edge Otsu algorithm. These water indices have been widely used and reported to have shown performed plausibly in mapping surface water. However, per the literature reviewed in this study, the NDWI showed an overall high accuracy in most of the studies. It must be stated that the choice of a spectral index depends on the bands a particular optical satellite image has. The satellite-based surface water maps will be assessed using both qualitative (i.e., visual inspection) and quantitative (i.e., overall classification accuracy and Kappa coefficient) assessments.

3. STUDY AREA AND DATASET

3.1. Description of the study area

The Densu River basin is located between latitudes $5^{\circ}30'N$ - $6^{\circ}17'N$ and longitudes $0^{\circ}10'$ - $0^{\circ}37'W$ and has an area of about 2,600 km². Located in the south-eastern part of Ghana, the basin covers portions of the Greater Accra, Central and Eastern regions, comprising a total of 13 districts (WRC, 2007). Water resources in the basin are managed by the Water Resource Commission (WRC). The hills occupying the north, together with the flatlands in the south of the basin, characterise its topography. As per the 2010 population census, the basin is made up of about 300 communities with a population of about 1.2 million (GSS, 2013). The main water body in the basin is the Densu River and has a total length of about 120 km. The source of this coastal river system is the Atewa range. The river flows southwards into the Weija reservoir, from which water is released through the ecologically significant Densu Delta Wetland, which is a Ramsar site before entering the Atlantic Ocean. The Ghana Water Company Limited (GWCL) is the body responsible for the operation and management of the Weija reservoir. The reservoir is an essential source of drinking water to a considerable section of the Accra metropolitan area. The study is to be conducted in the region downstream of the Weija dam as shown in Figure 3-1.

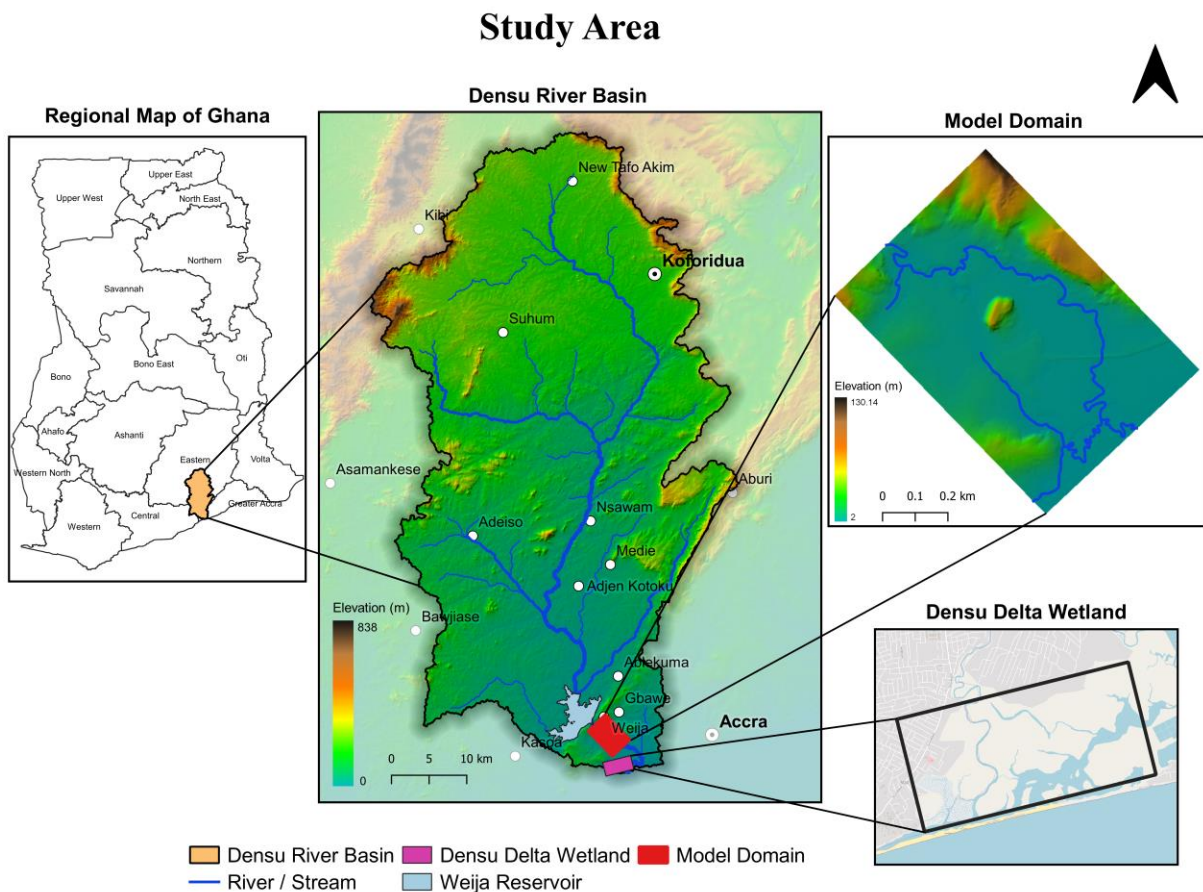


Figure 3-1: Map of the Densu River Basin and the selected model domain and a section of the Densu Delta Wetland

3.2. Dataset

The data gathered for the study include satellite images (optical and SAR), digital elevation model (DEM), discharge data, surface roughness data, river cross-section data and tidal data. The 10 m spatial resolution DEM, river cross-section data and discharge data were obtained from the study of Addae (2018). The satellite data acquired for the study are described in the following sections.

3.2.1. Tidal Data

Due to the lack of observed historical tidal data, the tidal data of Accra for 2017 was obtained from two independent data sources, both based on tide simulations. The data sources are the Tides4fishing (<https://tides4fishing.com>) and Tideschart (<https://nl.tideschart.com>) websites. A comparison of the data provided by these two sources was performed to assess differences and patterns. Figure 3-2 shows the comparison made with a 7-day window (28/07/2021 – 03/08/2021) tidal data from Tides4fishing and Tideschart. The figure shows that although the tidal data from Tides4fishing is slightly higher than that of the Tideschart, both exhibit similar shapes. Since historical data is available on the Tides4fishing website and not on the Tideschart website, tidal data from the former was chosen for the study.

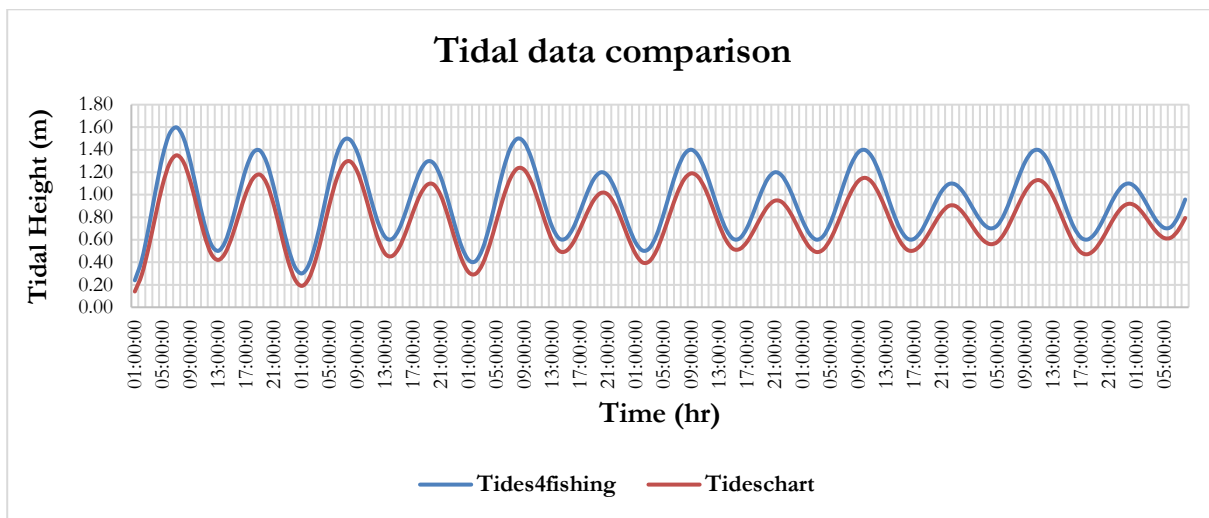


Figure 3-2: Tidal data comparison

The tidal data provided by Tides4Fishing is computed from historical time-series data obtained from mareographs. According to Tides4fishing (2021), this historical time-series data is modified using the Manual for Tidal Heights Analysis and Prediction by Foreman (1977). This manual by Foreman (1977) represents a user manual to G. Godin's tidal heights analysis and predictions programmes. This programme examines the height of hourly tidal data and simulates the amplitudes and Greenwich phase lags through the application of the least-squares method. Information on the tidal data provided by Tideschart was not available on the website.

3.2.2. Satellite Data

The initial flood windows identified for the study were centred on the Weija reservoir spillage dates from the year 2018 to 2020. A timeline on recent flood events was not available, so data on flood events were obtained from news outlets in Ghana. Personnel at the reservoir were also contacted for recent reservoir spillage dates. Freely accessible Landsat 8, Sentinel-2, and Sentinel-1 were the possible satellite imagery highlighted for the study. However, after an extensive search, clouds made it challenging to acquire good optical satellite images that captured flood events in the study area. Moreover, efforts made to acquire commercial satellite data such as WorldView-3 and SPOT 6 & 7 proved that none of these satellites'

sensors captured an image during the flood windows. Consequently, PlanetScope optical and Sentinel-1 SAR satellite images were obtained from the requisite online data repositories using flood windows deduced from the reservoir release data in Addae (2018). Additionally, PlanetScope and Sentinel-1 images of a dry-weather flow condition captured on the same day were acquired.

Table 3-1: Description of the satellite data collected for the study

Satellite Image	Bands/ Polarization	Spatial Resolution (m)	Revisit Time (day)	Acquisition Date	Condition
PlanetScope	R, G, B, NIR	3	2	25/06/2017	Flood
PlanetScope	R, G, B, NIR	3	2	14/07/2017	Flood
PlanetScope	R, G, B, NIR	3	2	24/12/2019	Dry
Sentinel-1	VV, VH	10	6	26/04/2017	Dry
Sentinel-1	VV, VH	10	6	25/06/2017	Flood
Sentinel-1	VV, VH	10	6	07/07/2017	Flood
Sentinel-1	VV, VH	10	6	24/12/2019	Dry

3.2.2.1. Sentinel-1 Imagery

Sentinel-1A and Sentinel-1B make up the Sentinel-1 constellation that capture images of the earth's surface using C-band synthetic aperture radar (SAR). Since the sensors on these satellites are not affected by atmospheric conditions, Sentinel-1A and Sentinel-1B provide images during the day and at night. The two satellites have the same orbital plane and are in a sun-synchronous orbit. The sensors aboard these satellites operate in four exclusive imaging modes and have spatial resolutions of down to 5 m. With a spatial coverage of up to 400 km, Sentinel-1 imagery offer dual polarisation capabilities, quick revisit times, and quick product distribution. For this study, four Level-1 Ground Range Detected (GRD) Sentinel-1 Interferometric Wide swath (IW) images were obtained from the Copernicus Open Access Hub (<https://scihub.copernicus.eu/>). Level-1 GRD images have been multi-looked and with the use of an earth ellipsoid projected to ground range. As a result, phase information is lost, although speckle is reduced. The IW mode enables the combination of a considerable swath width of 250 km and a moderate geometric resolution of 5 m × 20 m. The dual polarisation capabilities (i.e., vertical transmit and vertical receive (VV) and vertical transmit and horizontal receive (VH)) offered by Sentinel-1 both have a different interaction with surface water. The surface roughness of water, which may change due to wind, affects VV polarisation, while the presence of vegetation affects VH polarisation. Sentinel-1 images of dry conditions captured on 26/04/2017 (SD26APR17) and 24/12/2019 (SD24DEC19) were obtained together with flood images captured on 25/06/2017 (SF25JUN17) and 07/07/2017 (SF07JUL17). Table 3-2 contains detailed descriptions obtained from the metadata of the Sentinel-1 images employed for this study.

Table 3-2: Description of the Sentinel-1 data obtained for the study

Image Attribute	Date of Capture			
	26/04/2017	25/06/2017	07/07/2017	24/12/2019
Satellite mission	Sentinel-1A	Sentinel-1A	Sentinel-1A	Sentinel-1A
Product type	GRD	GRD	GRD	GRD
Acquisition mode	IW	IW	IW	IW
Orbit cycle	107	112	113	188
Polarisation	VV and VH	VV and VH	VV and VH	VV and VH
Spatial resolution	10 m	10 m	10 m	10 m
Incidence (near)	30.80	30.80	30.80	30.80
Incidence (far)	46.00	46.00	46.00	46.00
Relative orbit	147	147	147	147
Format	SAFE	SAFE	SAFE	SAFE
Pass	Ascending	Ascending	Ascending	Ascending

3.2.2.2. PlanetScope Imagery

The PlanetScope constellation comprises several satellites that capture optical images in the visible and near-infrared (NIR) bands. Although on-orbit capacity is continuously improving by rapid technological advancements, the PlanetScope constellation of almost 120 satellites can capture the entire globe daily at a collection capacity of 150 million km²/day (Planet Labs, 2021). PlanetScope satellite images are captured in scenes that are continuous parts of a single-frame satellite image. Three PlanetScope Analytic Ortho Tile (Level 3A) images were obtained from the Planet Explorer (<https://www.planet.com/explorer/>). According to Planet Labs (2021), these multispectral data have been orthorectified, radiometrically corrected, transformed to scaled at-sensor radiance and projected to a UTM projection. As a result of further processing, PlanetScope Surface Reflectance (SR) products are transformed from radiance to bottom-of-atmosphere (BOA) reflectance (Planet Labs, 2020). Table 3-3 provides detailed information on PlanetScope Analytic Ortho Tile (Level 3A) images. A dry PlanetScope image captured on 24/12/2019 (PD24DEC19) and flood images captured on 25/06/2017 (PF25JUN17) and 14/07/2017 (PF14JUL17) were downloaded for this research. PD24DEC19 had a cloud cover of about 5%. Also, PF14JUL17 had a cloud cover of less than 10%, while PF25JUN17 had a cloud cover of 40%. Portions of the area of interest in the flood images were covered with clouds, especially in PF25JUN17. The area of interest in PD24DEC19 was, however, cloud-free.

Table 3-3: Description of the PlanetScope Analytic Ortho Tile Product (source: (Planet Labs, 2021))

Product Attribute	Description
Information Content	
Analytic Bands	4-band multispectral image (blue, green, red, near-infrared)
Ground Sample Distance	3.7 m (average at reference altitude 475 km)
Processing	
Pixel Size (orthorectified)	3.125 m
Bit Depth	Analytic (DN): 12-bit Analytic (Radiance - $W\ m^{-2}\ sr^{-1}\ \mu m^{-1}$): 16-bit Analytic SR (Surface Reflectance): 16-bit
Geometric Corrections	Sensor-related effects are corrected using sensor telemetry and a sensor model, bands are co-registered, and spacecraft-related effects are corrected using attitude telemetry and best available ephemeris data. Orthorectified using GCPs and fine DEMs (30 m to 90 m posting) to <10 m RMSE positional accuracy.
Positional Accuracy	Less than 10 m RMSE
Radiometric Corrections	<ul style="list-style-type: none"> • Conversion to absolute radiometric values based on calibration coefficients • Radiometric values scaled by 100 to reduce quantization error • Calibration coefficients regularly monitored and updated with on-orbit calibration techniques.
Atmospheric Corrections	<ul style="list-style-type: none"> • Conversion to top of atmosphere (TOA) reflectance values using at-sensor radiance and supplied coefficients • Conversion to surface reflectance values using the 6SV2.1 radiative transfer code and MODIS NRT data • Reflectance values scaled by 10,000 to reduce quantization error

4. METHODOLOGY

4.1. Surface Water Mapping

Image pre-processing is an essential part of satellite image processing. The procedure prevents the propagation of image distortions that render satellite-based maps inaccurate and unsuitable for decision making. Although the PlanetScope Analytic Ortho Tile images have undergone orthorectification, radiometric correction and have been projected to UTM coordinates, only surface reflectance products of this category have been processed beyond the at-sensor radiance scale transformation. As a result, surface reflectance images have bottom-of-atmosphere reflectance. Furthermore, since PlanetScope images are produced in scenes that may not fully cover the area of interest, image pre-processing was essential to merge the required scenes to cover the areas of interest. The Sentinel-1 images were pre-processed to account for image distortions.

To address the misfit along the edges of the satellite-based inundation extents and the 1D2D Sobek hydrodynamic model simulated inundation extents, as indicated in the findings of Addae (2018), the use of a surface water mapping approach that considers edge detection was imperative to this study. Hence, as demonstrated in the study by Markert et al. (2020), the Edge Otsu algorithm was used to map surface water bodies in the SAR and optical satellite images considered for the study. Surface water bodies within the model domain and the portion of the Densu Delta Wetland highlighted for the study were mapped using the flood images and dry-weather flow condition images, respectively. The surface water within the Densu Delta Wetland was primarily mapped to assess the performance of the Edge Otsu algorithm in mapping permanent surface water bodies. As described in section 2.4 above and illustrated in Figure 4-1 below, the Edge Otsu algorithm is an unsupervised algorithm that requires a number of parameters to function. The parameters used in the study of Markert et al. (2020) included the initial threshold, edge length and edge buffer parameters were applied in this study for surface water mapping.

The initial threshold parameter determines which part of a satellite image is considered water and which part is considered non-water. Essentially, the parameter is used to create a binary image of water and non-water classes. The edge length parameter filters detected edges in the binary image created using the initial threshold by retaining only edges with lengths greater than or equal to the parameter value. On the other hand, the edge buffer parameter determines the distance of the buffers created on both sides of the filtered edges for pixel sampling to create a bimodal histogram. Details of the Edge Otsu algorithm and the parameters used in this study can be found in the Hydrologic Remote Sensing Analysis for Floods (HYDRAFloods) open-source Python package documentation (<https://servir-mekong.github.io/hydra-floods>). The parameters of the Edge Otsu algorithm as introduced above should be suited to the region being studied as well as the characteristics exhibited by the surface water bodies present in the satellite images employed. Although the methodology used by Markert et al. (2020) involved mapping surface water in all the satellite images analysed by assigning a fixed set of values to the parameters to underscore baseline accuracies, the authors indicated that tuning these parameters could offer customised results for different sites. In view of this, the three parameters used to apply the surface water mapping algorithm highlighted for this study were fine-tuned by evaluating and considering the employed satellite images' properties and assessing the effects of possible parameter values on the resultant surface water maps.

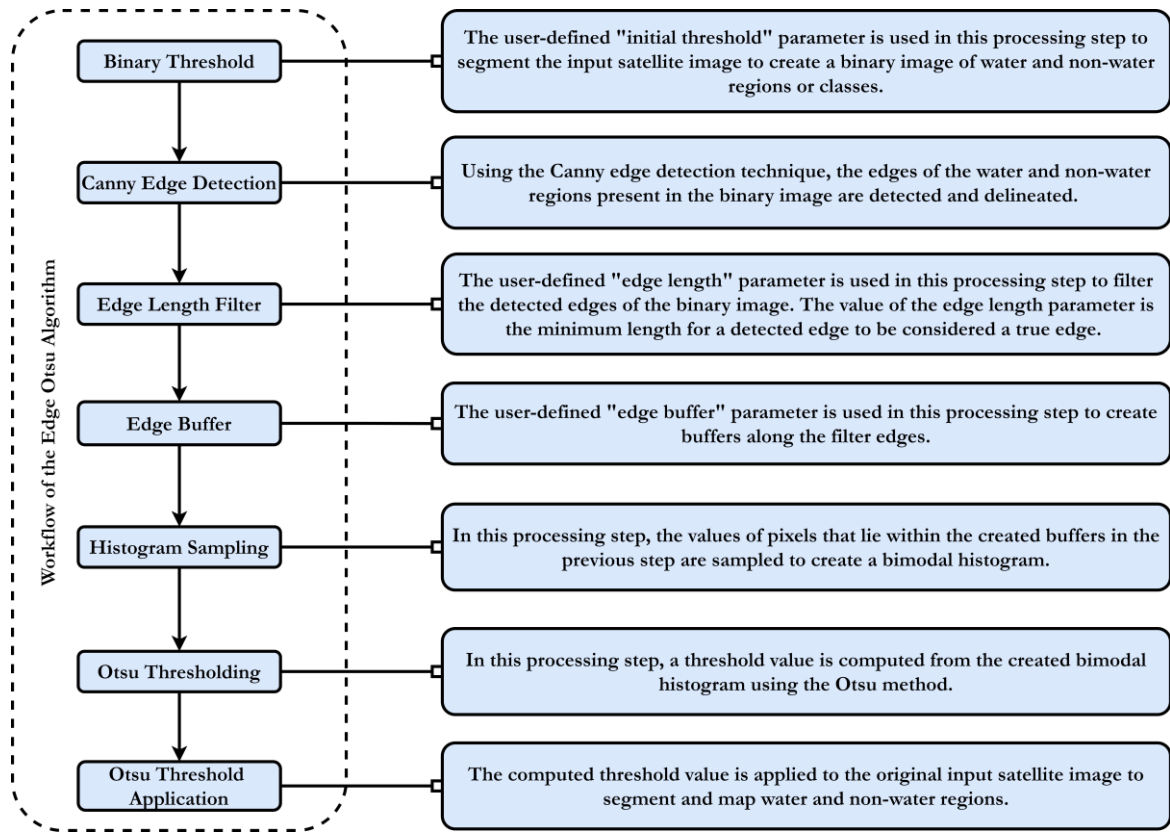


Figure 4-1: Description of the Edge Otsu algorithm demonstrated in the study of Markert et al. (2020)

The surface water mapping operations of the study were performed employing the Google Earth Engine (GEE) platform, the HYDRAFloods open-source python package and the GEE Python application programming interfaces (API). GEE is a cloud-based computational resource for scientific evaluation and visualisation of geospatial data for various purposes. The platform hosts several satellite images stored in a public repository and offers simple, web-based access to new and historical satellite images. GEE's data catalogue is complemented by adaptable APIs (JavaScript and Python) and robust, scalable computing offered by Google data centres that easily allow users to execute current geospatial workflows. The GEE code editor, a web-based integrated development environment (IDE) that uses the JavaScript API by default, is perhaps the most utilised means to interact with GEE. Apart from the GEE code editor, the GEE Python API can be used without operating a web browser. The pre-processed Sentinel-1 and the further processed PlanetScope satellite images were uploaded to GEE as assets in GeoTIFF format. The images were then imported into Jupyter Notebook via the GEE Python API, after which the Edge Otsu algorithm was applied using the HYDRAFloods package.

4.1.1. Sentinel-1 Surface Water Mapping

The findings of Addae (2018) proved that the VV polarisation bands performed best in mapping floods in the study area. Also, the accuracy assessment executed on the Sentinel-1 surface water maps produced in Twele, Cao, Plank, & Martinis (2016) proved that the VV polarisation band performed better than the VH polarisation band. Therefore, only VV polarisation images were considered for this study. Figure 4-2 describes the Sentinel-1 surface water mapping workflow.

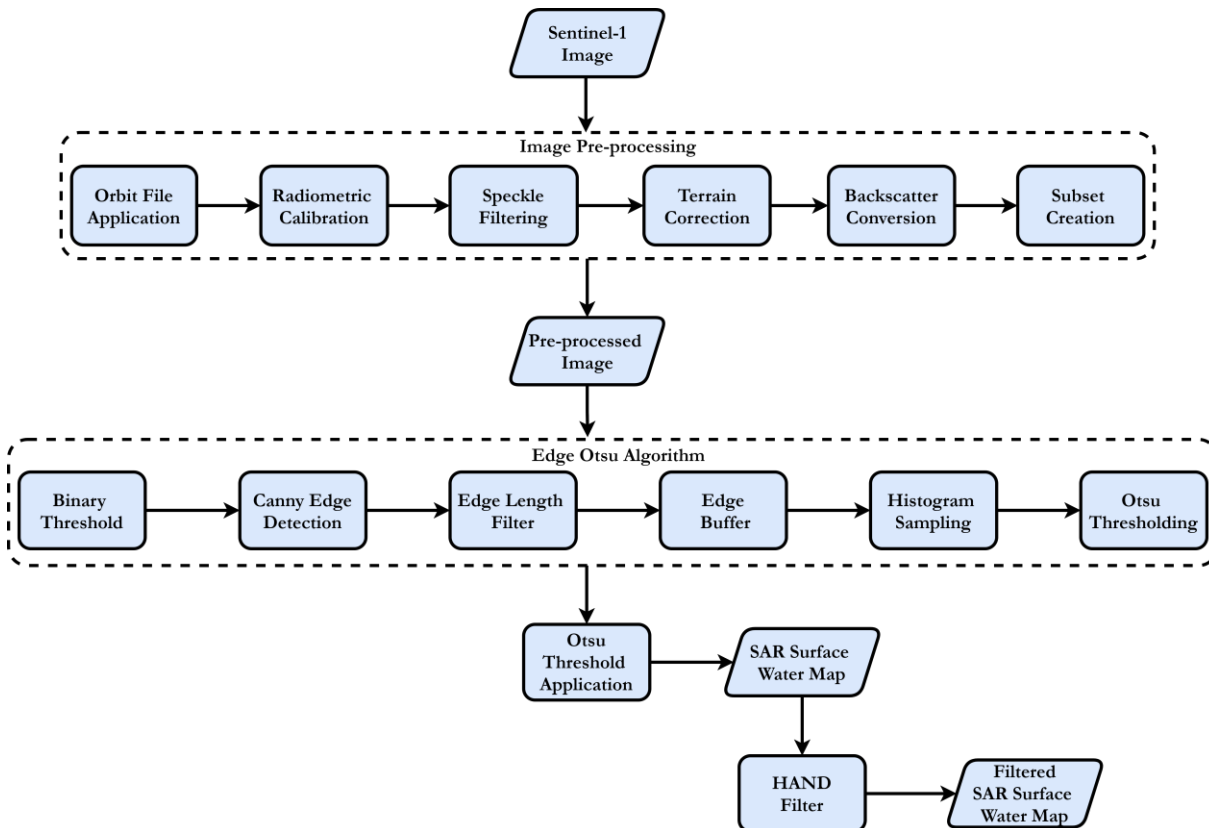


Figure 4-2: Sentinel-1 surface water mapping workflow

4.1.1.1. Sentinel-1 Image Pre-Processing

Sentinel-1 image pre-processing was performed to reduce speckle effects, orbital drift, and terrain and geometric distortions. Generally, images with correct geometry and backscatter coefficient values independent of the observation are appropriate for useful analysis. The processing tools of the Sentinel-1 Toolbox (S1TBX) were employed to pre-process the Sentinel-1 images in the Sentinel Application Platform (SNAP 8.0). The collection of tools and data products in the S1TBX are utilised for reading, writing, displaying and analysing SAR imagery. The Sentinel-1 image pre-processing steps used for the study were orbit file application, terrain correction, calibration, speckle filtering and subset creation. All the pre-processing steps were automated using the graph builder and batch processing tools in SNAP 8.0.

Although a satellite's orbit may be fine-tuned, the satellite's precise position may drift over time due to factors such as atmospheric drag and solar winds. Adjustments are required due to such drifts and as such, having the most up-to-date orbit file that provides information on a satellite's exact position is crucial. The orbit information found in the metadata of downloaded Sentinel-1 images is often inaccurate. Such inaccurate orbit files cause mismatching when SAR data are superimposed after pre-processing. By

applying the updated orbit file, the geographic location accuracies of Sentinel-1 images are improved. The orbit file application procedure was performed using the apply orbit file tool.

Sentinel-1 images obtained from the Copernicus Open Access Hub have digital pixel values. Since surface features on SAR images are identified due to variations in backscatter intensity, the pixels values (digital numbers (DN)) of the Sentinel-1 images must be converted into radiometrically calibrated backscatter values. Radiometric calibration of SAR images was performed using the calibrate tool. Based on the metadata of a SAR input image, SNAP automatically determines the necessary conversion needed. Also inherent to coherent measuring techniques like SAR is the granular interference known as speckle. The quality of SAR images is significantly degraded due to this unwanted modification. Speckle occurs when scattered radar signals interfere with each other, causing positive and negative interference patterns seen on SAR images as dark and bright spots. Speckle filtering is a method of reducing speckle to make image interpretation less challenging. Such filtering methods often remove actual pixel information, and the selection and application of a particular filter come with trade-offs. Also, performing speckle filtering after radiometric calibration prevents the filtered speckle from propagating into subsequent satellite image processes. The 3×3 Gamma Map filter was used for the study. This speckle filter was applied on Sentinel-1 images in the same study area by Addae (2018) and was documented to have effectively reduced speckle and maintained the edge information of surface features.

Since Sentinel-1 images do not have geographic coordinates, transforming these images into a coordinate system is necessary for proper spatial analysis of such data. Also, due to the viewing geometry of SAR sensors, SAR images are impacted by geometric distortions owing to relief displacement. Two of the effects of relief displacement are foreshortening and layover. Both effects result in radar shadows. As a result, terrain correction is needed to correct the effects caused by the side-looking SAR sensor and various terrain features. The procedure was performed using the range-doppler terrain correction tool. The tool applies topographic information (typically provided by a DEM) and orbit information to correct geometric distortions and assign a coordinate system to SAR images.

The backscatter coefficient values obtained after radiometric calibration was transformed to decibel (dB) through a logarithmic conversion using the linear to dB conversion tool. The logarithmic conversion addresses the skewness of the image histogram towards large values and, as a result, enables backscatter intensities to be shown with detail. Finally, since the obtained Sentinel-1 images covered more area than required, further image processing operations warranted the need to extract the area of interest. Creating a subset reduces the size of the image and, subsequently, the computational time required for further image processing. This step of the SAR image pre-processing was executed applying the subset tool.

4.1.1.2. RGB Composite image creation

To know where floodwaters (shallow waters), permanent water bodies (deep water), and dry areas existed in the Sentinel-1 flood images, RGB composite images were created. For this process, the pre-processed Sentinel-1 flood images captured on 25/06/2017 and 07/07/2017 (SF25JUN17 and SF07JUL17) were considered crisis images, while the dry-weather flow image captured on 26/04/2017 (SD26APR17) was considered the archive image. Separate image stacks created from the archive and each crisis image were employed to create the RGB composite images. The band combination used involved assigning the VV polarisation band of the archive image to the red channel, while the green and blue channels were assigned the VV polarisation band of a crisis image. The archive image was not involved in any further processing apart from creating the RGB composite images from the Sentinel-1 flood images.

4.1.1.3. Application of the Edge Otsu Algorithm on the Sentinel-1 Images

Before uploading the VV polarisation bands of SF25JUN17, SF07JUL17 and SD24DEC19 to the GEE platform, the flood images were assessed to identify backscatter coefficient (sigma nought) values of pixels located in flood areas and permanent water bodies. Knowledge of these differences through the pixel-by-pixel examination of backscatter coefficient values aided in determining the backscatter threshold values. The initial threshold parameter values assigned to the Edge Otsu algorithm for the various Sentinel-1 images were determined manually through visual interpretation as in the study of Psomiadis, Diakakis, & Soulis (2020) by carefully examining the logarithmic bimodal image histograms. In addition, the backscatter coefficient (sigma nought) values of pixels within permanent water and the shallow water bodies were examined. Since the Edge Otsu algorithm uses the initial threshold parameter to create binary images of water and non-water regions in the satellite images, the Canny Edge filter applied to the binary images delineates the edges of water and non-water regions only. In view of this, eliminating any detected surface water body edge would negatively affect the pixel sampling for the bimodal histogram creation and, ultimately, the computation of the Otsu threshold. As a result, all detected surface water body edges were considered for the buffering processes that followed as per the workflow of the Edge Otsu algorithm shown in Figure 4-2 above. Also, since the smallest surface water body edge that can be detected on each of the various satellite images would be contained in a pixel, the edge length parameter was assigned a value equal to the spatial resolution of Sentinel-1 images used.

The edge buffer parameter could not be determined from any of the properties of the Sentinel-1 satellite images used for the study, and thus the parameter values assigned to the Edge Otsu algorithm were determined using the trial-and-error approach. First, sensitivity analysis was performed by varying the edge buffer parameter values to assess the effects of the parameter on the surface water maps produced. Later, to obtain optimal parameter values, the surface water maps produced from each of the Sentinel-1 images as a result of the edge buffer parameter variations were compared to corresponding water masks created using the respective backscatter threshold values used as the initial threshold parameter values. The water masks of the Sentinel-1 images were separately computed using the band maths tool in SNAP by selecting pixel values less than the initial threshold parameter values. The comparisons were based on the area of inundation and were performed to keep the surface water maps realistic since the initial reason for selecting the Edge Otsu algorithm was to accurately detect the surface water bodies at the edges of water and non-water regions and not to obtain inundation increases. The edge buffer parameter value that resulted in a surface water map with the smallest root mean square error (RMSE) when compared to a corresponding water mask was considered optimal. Surface water in the Weija reservoir and the Densu Delta Wetland were used as checks during the mapping exercises. The final stage of the algorithm's workflow involved applying the computed Otsu threshold values to segment the Sentinel-1 images by categorising pixels with backscatter values lesser than the threshold value as water and those greater than the threshold value as non-water. SF25JUN17 and SF07JUL17 were used to create surface water maps of the model domain. SD24DEC19 was used for mapping surface water within the Densu Delta Wetland.

4.1.2. PlanetScope Surface Water Mapping

Spectral indices such as the Tasseled Cap Wetness Index (TCW) and the Modified Normalised Difference Water Index (MNDWI) can be applied to map surface water provided an optical satellite image has a short-wave infrared band. This indicates that the choice of a spectral index for detecting surface water bodies depends on the particular bands a satellite image has. For this study, since the PlanetScope images lacked short-wave infrared bands, the Normalised Difference Water Index (NDWI) was computed to detect surface water bodies in the study area. The NDWI for each optical satellite image employed for the

study was computed by subtracting the NIR band from the green band and dividing the result by the sum of the two bands. The equation for the spectral index is stated in Table 2-1. The processes employed for the PlanetScope surface water mapping procedure is presented in Figure 4-3.

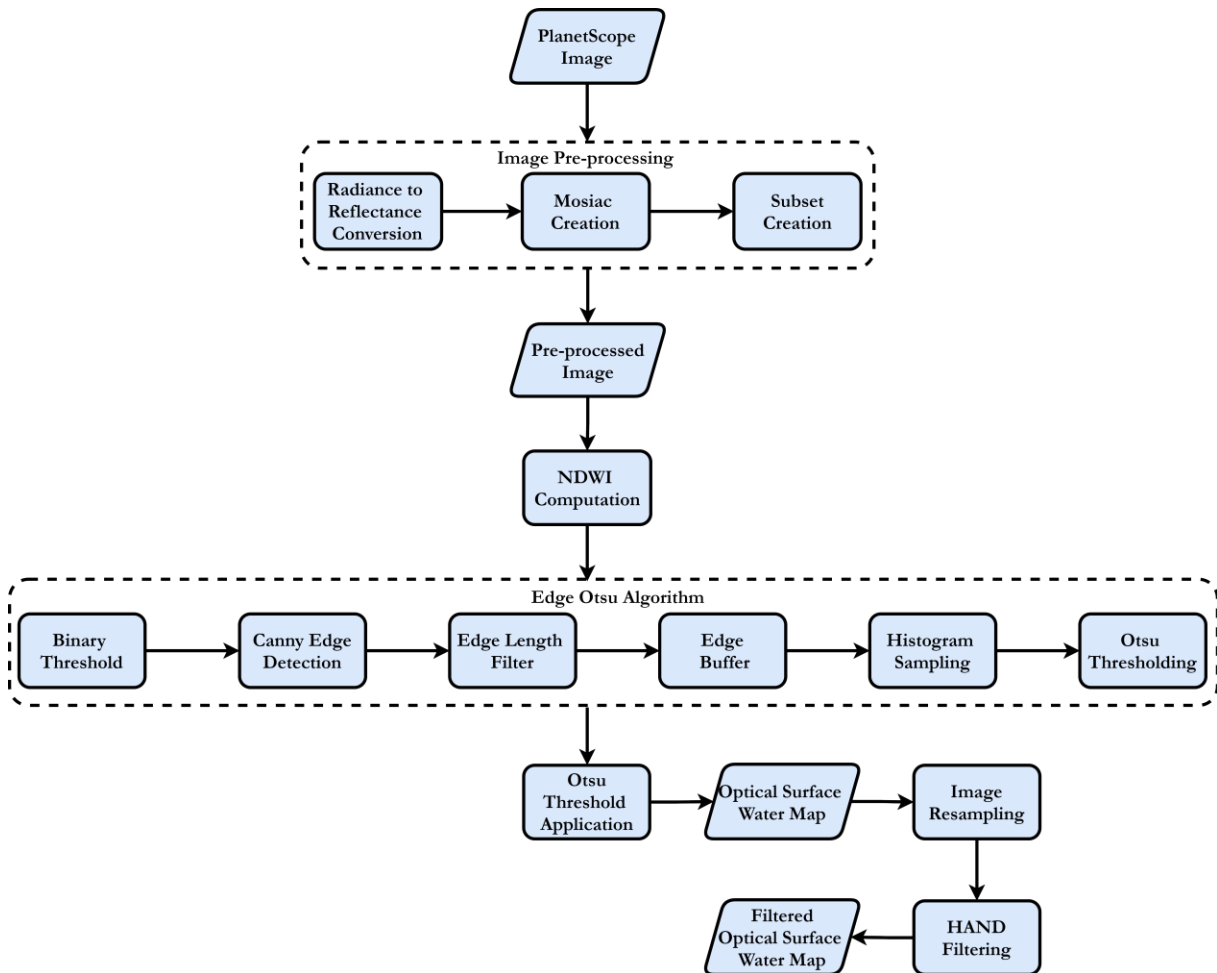


Figure 4-3: PlanetScope surface water mapping workflow

4.1.2.1. PlanetScope Image Pre-Processing

Since image distortions with the PlanetScope images have been corrected from source, the pre-processing steps taken to ready the PlanetScope images for further processing included radiance to top-of-atmosphere (TOA) reflectance conversion, mosaic and subset creation. The conversion of pixel values from radiance to TOA reflectance was important for a more accurate spectral index calculation. The acquired PlanetScope flood image captured on 25/07/2017 (PF25JUN17) and the dry-weather flow image captured on 24/12/2017 (PD24DEC19) were surface reflectance products with bottom-of-atmosphere pixel reflectance values. As a result, a radiance to TOA reflectance conversion procedure was not required for these images. The pixel values of the PlanetScope flood image captured on 14/07/2017 (PF14JUL17), on the other hand, were radiance values and needed to be pre-processed to TOA reflectance values. The radiance to TOA reflectance conversion was executed in Python 3.9.4 using the TOA reflectance coefficients obtained from the metadata of the various scenes. The mosaic creation procedure executed in the pre-processing of the PlanetScope images entailed stitching the various scenes of the individual downloaded images into single units to include the areas of interest. Subsets of the individual images were

then created to obtain the exact areas of interest. Mosaics and subsets of the acquired PlanetScope images were created using the mosaicpro and create subset image tools in ERDAS IMAGINE 2020.

4.1.2.2. Application of the Edge Otsu Algorithm on the PlanetScope Images

The outputs of the NDWI computation were used as inputs to the Edge Otsu algorithm. The initial threshold values for the Edge Otsu algorithm were determined from visually inspecting the NDWI values of surface water in the Weija reservoir, the Densu river channel and the Densu Delta Wetland. The edge length parameter was assigned the spatial resolution of the PlanetScope images used for the study. The edge buffer parameter values were determined using the trial-and-error approach as stated in subsection 4.1.1.3 above. The implementation of the Otsu thresholding by the Edge Otsu algorithm on the sourced PlanetScope images was performed by categorising pixels with NDWI values greater than the computed Otsu threshold values as water and pixels with lesser NDWI values as non-water. The PlanetScope flood images, namely, PF25JUN17 and PF14JUL17, were used to map surface water bodies within the model domain, while the dry-weather flow image, PD24DEC19, was used to map surface water bodies within the Densu Delta Wetland.

4.1.3. Height Above Nearest Drainage (HAND) Creation and Filtering

The Height Above Nearest Drainage (HAND) algorithm by Rennó et al. (2008) was proposed to detect regions with the lowest elevation and thus with a chance of inundation. According to the authors, the HAND, a HydroDem analysis tool, characterizes DEM elevation variation between each land surface pixel and the channel bottom pixel to which flow is transported. In view of this, in satellite-based surface water mapping, the HAND can be used as a tool to constrain the detection of surface water pixels to specified threshold elevations within a floodplain or any area of interest with marginal differences between dry and wetted surfaces. The technique serves to improve the accuracy of satellite-based surface water maps by reducing surface water misclassification. Several studies have highlighted the use of the HAND to accurately detect surface water pixels from remotely sensed imagery (Hu & Demir, 2021; Huang, Nguyen, Zhang, Cao, & Wagner, 2017; Markert et al., 2020). This study employed the HAND to constrain surface water detection to flood-prone areas in the study area. The 10 m resolution DEM was used to create the HAND filter for the model domain. The creation of the HAND was executed by adapting the method demonstrated by Rennó et al. (2008), as illustrated in Figure 4-4 below. As shown in the figure, the elevation of each HAND pixel is a result of the elevation differences between the pixels and the corresponding nearest drainage pixel elevation.

The development of the HAND filter was implemented employing the Spatial Analyst extension toolbox of ArcGIS in ArcMap 10.8.1, and Figure 4-5 shows the processes and steps used. Since the topography of an area affects flow directions and the dendritic network, Rennó et al. (2008) indicated that a DEM without local sink points is required to ensure accurate computation of flow directions and, consequently, the definition of the drainage system. Thus, the local depressions in the 10 m resolution DEM of the model domain were filled using the fill tool. Several methods for computing flow directions exist in literature (Zhou & Liu, 2002). However, for this study, the most commonly applied D8 algorithm originally put forward by O'Callaghan & Mark (1984) was used to create flow direction and flow accumulation from the DEM with filled depressions. The flow accumulation tool, which computes the number of upstream grid cells that flow into a single cell, was computed and used to obtain the drainage network. The flow accumulation raster was then classified to obtain the flow accumulation threshold for extracting the drainage network within the model domain. The raster of the drainage network was converted into a point shapefile which was used together with the flow direction raster in the watershed

tool to create zones with the same local drainage patterns for zonal statistics on the elevations present in these zones to be performed. Using the original 10 m resolution DEM with the depressions or sinks, the lowest elevation within the created zones was detected. Finally, this lowest elevation was subtracted from the original 10 m resolution DEM. The pixel values of resultant HAND were then converted to integers in order to have discrete HAND elevations.

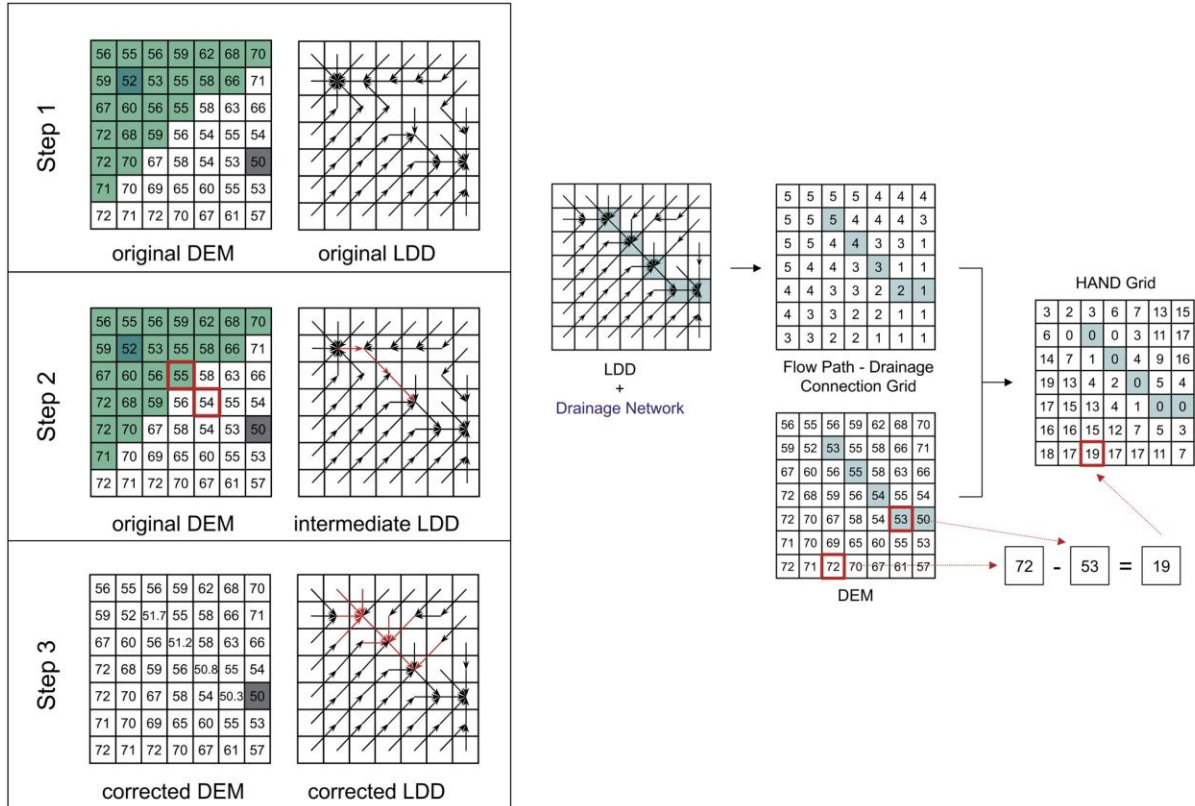


Figure 4-4: Diagram explaining the HAND development process as executed in the study by Rennó et al. (2008)

For the model domain, regions with HAND elevations that were less than or equal to 2 were considered regions that would get inundated with water. Consequently, detected water pixels in the Sentinel-1 and PlanetScope flood images with the exact locations as the HAND elevations that fit the condition were kept as water in the filtered surface water maps. The water pixels that did not meet the criteria were converted to dry pixels. The extent of the extracted HAND due to this condition was the same as the HAND extent used by Addae (2018). The filtering procedure performed on the PlanetScope surface water maps of the model domain was executed after the images were resampled to the resolution of the 10 m HAND. The Sentinel-1 images, however, did not need resampling since the satellite images had a spatial resolution of 10 m. The permanently wetted Densu Delta Wetland did not fall within the spatial coverage of the 10 m HAND; therefore, no filtering was performed for the satellite-based surface water maps of the region. The HAND filtering processes were performed in ArcMap 10.8.1 using the raster calculator tool.

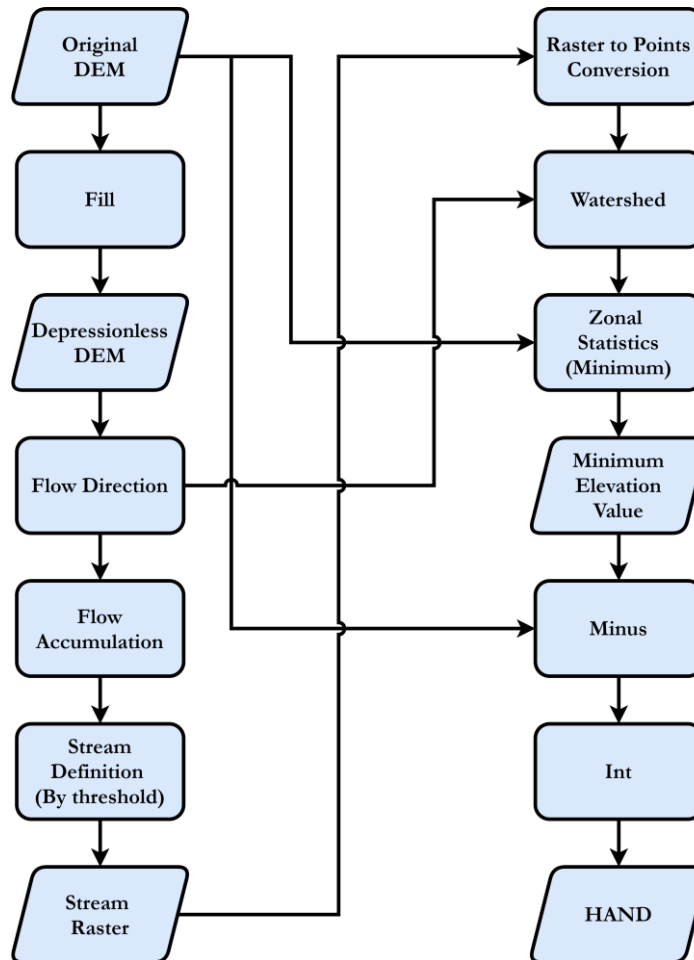


Figure 4-5: HAND creation flowchart

4.1.4. Evaluation of Surface Water Maps

Visual inspection was used as the primary means of assessing all surface water maps produced in the study. Also, the Kappa coefficient and overall classification accuracy were used to assess the satellite-based surface water maps quantitatively. These metrics were chosen because they have been extensively used in several surface water mapping studies (Ashtekar et al., 2019; Bhaga et al., 2020; Markert et al., 2020). Since no ground truth data of flooded regions were collected for the study, the high-resolution 3 m PF14JUL17 and PD24DEC19 optical satellite images were employed as reference images, and as such, reference data were collected from these images using visual interpretation. This enabled the quantitative evaluation of the satellite-based surface water maps of the model domain as well the Densu Delta Wetland. However, cloud cover at the upper part of PF25JUN17 made it impossible to collect reference data on the whole model domain. Therefore, the surface water map produced from PF25JUN17 were not evaluated. The surface water map of SF25JUN17 was also not quantitatively assessed due to the inability of collecting reference data from SF25JUN17 or any comparable optical image that captured the event of 25/06/2017. Similarly, the surface water map produced from SF07JUL17 was not assessed quantitatively due to the lack of comparable high-resolution optical satellite imagery. The surface water maps evaluated in this study were produced from PF14JUL17, PD24DEC19 and SD24DEC19. A hundred reference points were created in ArcMap 10.8.1 for each surface water map evaluated. The accuracy assessments of the surface water maps were performed using the accuracy assessment tool in ERDAS IMAGINE 2020.

4.1.5. Sentinel-1 and PlanetScope Image Fusion

Since SAR and optical sensors both observe the earth surface differently, fusing data from these sensors can result in a more robust surface water map. For the purpose of exploiting the strengths of both Sentinel-1 SAR and PlanetScope optical satellite images, the feature-level image fusion method was utilized in fusing the various satellite images employed for this study. The aim was to improve the accuracy of the surface water maps produced using data from a single sensor. Unlike pixel-level image fusion, feature-level image fusion is guided by the qualities of the preferred output. Decision-level image fusion, on the other hand, is computationally expensive since more than one classifier is needed.

The feature-level image fusion method used in fusing the SAR and optical satellite images was adapted from the study by Tavus et al. (2020). For a single satellite image fusion operation, the VV and VH polarisation bands of a Sentinel-1 image and all the spectral reflectance bands of the PlanetScope images as well as the NDWI maps were co-registered and stacked for supervised digital image classification. The co-registration operations were performed in ERDAS IMAGINE 2020. Training and validation samples were manually delineated from PlanetScope images in ArcMap 10.8.1. The Random Forest classifier was sourced for the classification processes, which were performed in RStudio 4.0.5. The Random Forest classifier was chosen because of its ability to evaluate the importance of each input feature (or variable) and its performance in providing good classification results even without hyper-parameter tuning (Z. Xu et al., 2018). The random forest classifier is also fast and comparatively robust to outliers and noise and devoid of overfitting (Breiman, 2001).

One hundred points each for the water and non-water classes were sampled for training and validation purposes for a single fusion procedure. For each classification executed, the random forest classifier was trained with 70% of the sampled points, and the remaining 30% was used to validate the classification output. Since multiple iterations of the random forest classifier can result in different classification accuracies, ten iterations were run for every classification performed. This was to facilitate selecting a visually plausible classification output with the highest overall classification accuracy and Kappa coefficient out of the ten classification results due to the iterations. SF07JUL17 was fused with PF14JUL17 to map surface water bodies within the model domain. SD24DEC19 and PD24DEC19 were also fused to map surface water bodies within the Densu Delta Wetland. Since SF07JUL17 and PW07JUL17 were not captured on the same day, the fusion output was considered multi-sensor and multi-temporal. The feature-level image fusion approach used for the study is presented in Figure 4-6.

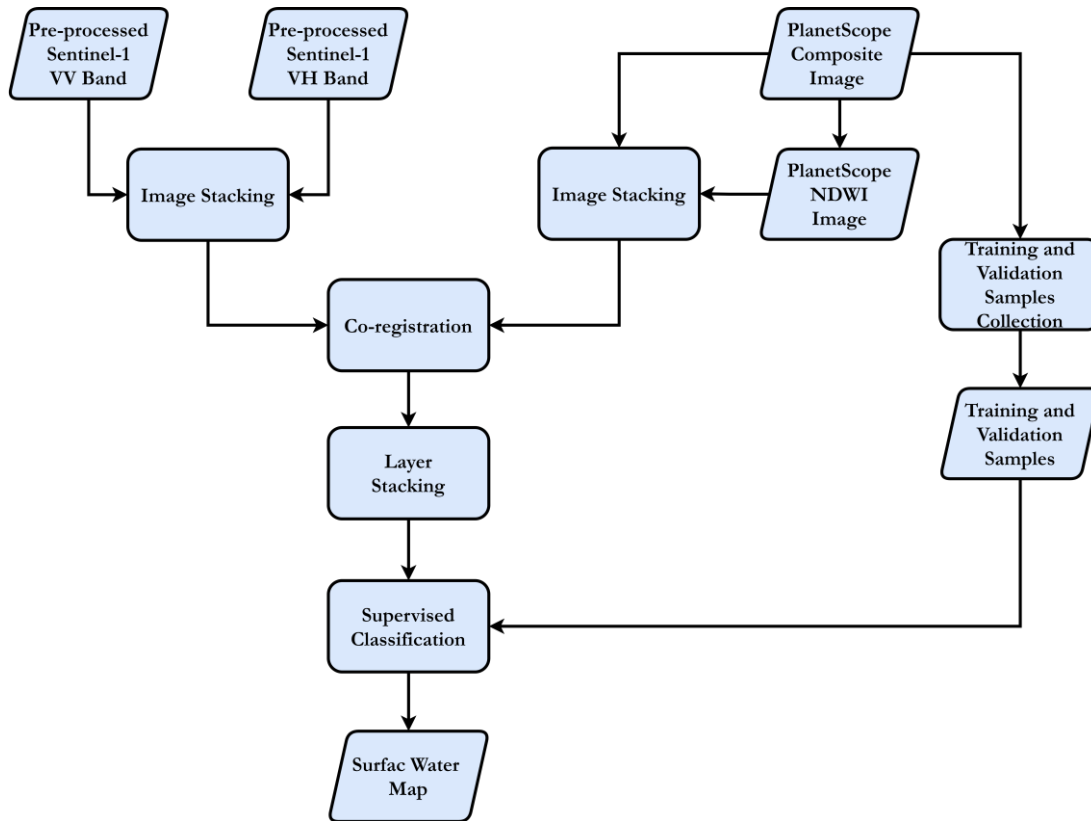


Figure 4-6: Feature-level satellite image fusion approach used to fuse the Sentinel-1 and PlanetScope satellite images

4.2. Hydrodynamic Modelling

4.3. Sobek Model Setup and Schematisation

A hydrodynamic model was necessary to assess the effects of tides in the study area. Therefore, the study employed the 1D2D SOBEK hydrodynamic model to simulate flow processes in the channel and on the floodplains. The 1D2D SOBEK hydrodynamic model setup, which included the model schematisation, was adapted from the study of Addae (2018). Also, the 1D network, cross-section data, surface roughness data, boundary conditions and the 2D grid were adopted from Addae (2018). Information on the SOBEK model, the 1D flow and 2D flow equations, as well as the 1D-2D connections, are represented in Appendix C of this thesis document.

The schematisation of the 1D and 2D components of the model was performed in the schematisation task block. This block contains the NETTER, which is the network generator and editor of the SOBEK model that allows model schematisation with a GIS map layer as the background. In the generation of a 1D network in the NETTER, calculation nodes are added to the branches that are created. Apart from schematisation operations such as importing and editing network elements as well as 2D grids, the advanced analysis tools in the NETTER can also be used to visualise simulation results as flow animations. Moreover, importing cases from other projects as well as exporting simulated inundation maps in formats accessible in GIS environments is possible in the NETTER. The background map on which the schematisation was performed was imported into the NETTER in an Enhance Compression

Wavelet (.ecw) image file format. The adopted 1D network was made up of a number of branches with several calculation nodes connected via connections nodes.

The modifications made to the schematisation of the 1D2D SOBEK hydrodynamic model included substituting the 2D boundary nodes installed at the upstream and downstream ends of the model domain with 1D boundary nodes. According to Deltares (2018), the exterior borders of a hydraulic schematisation are marked by these boundary nodes, and as a consequence, accurate boundary conditions should be employed to characterize interactions (i.e. water inflows and outflows) with the real world from outside the model domain. The 1D boundary node of the SOBEK permits the input of flow (Q), water level (H) or Q - H boundary conditions. Alternating discharge data (flow condition) was assigned to the 1D boundary node located at the upstream channel inflow point of the 1D network to account for the reservoir releases that enter the model domain. To account for the water level at the downstream end of the 1D network, the specified constant head (Dirichlet) condition was applied to the downstream 1D boundary node. This was to enable a free flow condition and thus facilitate the outflow of water from the model domain.

In addition to the 1D boundary nodes, a 2D line boundary was defined at the downstream end of the model domain to allow the inflow and outflow of water over multiple 2D grid cells. This was to establish a tidal boundary to account for the effects of tidal behaviour. The 2D line boundary effects specified flow or head conditions, both of which can be constant or can vary with time to the grid cells to which it is assigned. A 2D line boundary can only be established when oriented vertically or horizontally (see Figure 4-7). Deltares (2018) instructs that all grid cells on which a 2D line boundary is installed should contain no-data values (i.e., -9999), and also, from each boundary grid cell, water ought to be permitted to flow to or from a single grid cell. Furthermore, 2D line boundaries cannot be installed on nested grids. Figure 4-7 illustrates the likely installations of a 2D line boundary.

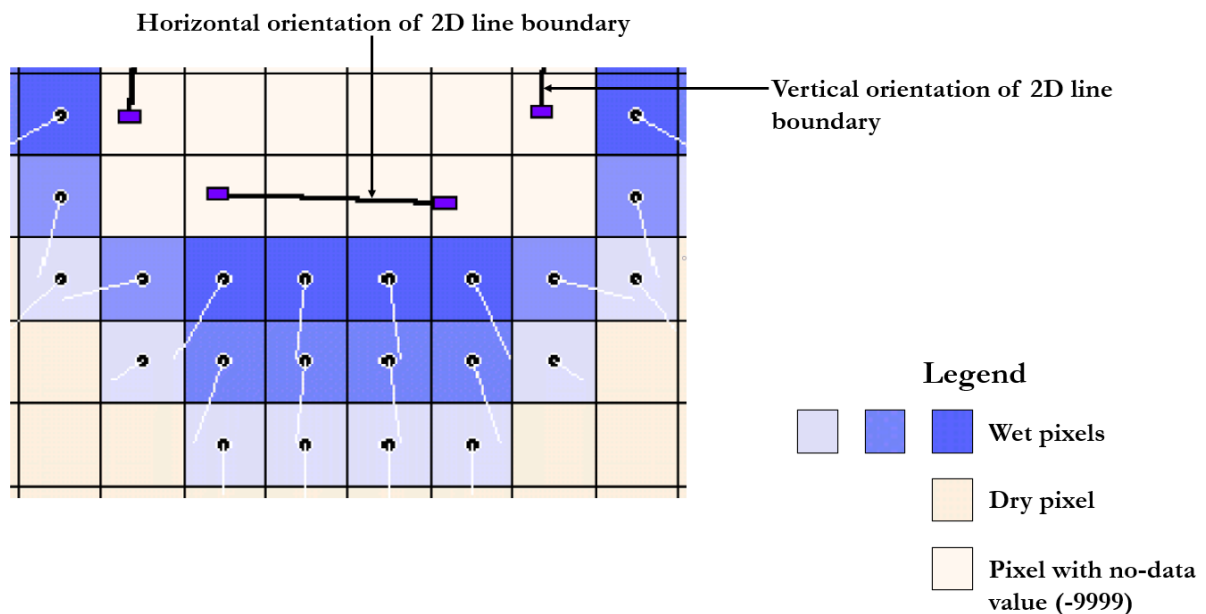


Figure 4-7: An example of a 2D line boundary configuration adapted from Deltares (2018)

For this thesis, it is essential to mention that the 2D line boundary installation location did not represent the actual coastline where the Densu River through the Densu Delta Wetland connects to the Atlantic

Ocean. This was because the 10 m resolution DEM used in schematising the 1D2D SOBEK model did not extend to the coastline. Moreover, along the coastline, a high dune area separates the coast from the Densu Delta Wetland of which part of the downstream end of the model domain covers. The part of the Densu Delta Wetland covered by the model domain is a peat area often inundated by saline water from the Atlantic Ocean downstream due to tidal intrusion. This led to the assumption that this peat area serves as a connection between the model domain and the ocean. Thus, the 2D line boundary was installed at the edge of the lower-left corner of the model domain below the downstream 1D boundary node. The elevations of the 2D grid cells for which the 2D line boundary was installed were the lowest in the DEM.

A riverbed's shape, which is described collectively by cross-sections, largely determines the channel conveyance capacity and thus the discharge that may flow through respective cross-sections. Thus, an accurate model schematisation involves defining a number of cross-sections, which is achieved by adding flow-cross-section nodes. Generally, cross-sections are entered at locations where there are distinct changes in shape, discharge, or roughness. Usually, large uniform river channels with flat channel slopes need a few cross-sections compared to meandering channels and channels with steep riverbed slopes. In this study, for an accurate depiction of the channel system, twelve flow cross-sections nodes comprised of ten Y-Z and two trapezium profiles were defined at the appropriate locations on the requisite branches. The model data editor window for a trapezoidal flow cross-section node in SOBEK allows the definition of the dimensions, bed level, surface level, slope, maximum flow width and bottom width. For Y-Z profile cross-sections, the dimensions, surface level, and level shift can be assigned in the model data editor window. SOBEK uses linear interpolation to interpolate between user-located cross-sections and network-generated cross-sections along the branches to provide gradual densification of model calculation nodes. Densification serves to construct a 1D channel system with a gradual transition of channel properties and distribution of calculation nodes to best represent channel flow behaviour. Also, four bridges were established on some branches within the model domain.

A 2D grid was imported in the NETTER after the 10 m resolution DEM was transformed into an ACII file format in ArcMap 10.8.1 to represent the floodplains. Furthermore, regarding representing flow resistance within the model domain due to surface roughness in the channel and the floodplains, a constant Manning's coefficient of 0.03 was used to test the model and perform sensitivity analysis. As described in Appendix C, the 1D channel system is connected to the 2D grid via the connection or the calculations nodes and the centres of the 2D grid cells. The schematisation of the model domain is shown in Figure 4-8.

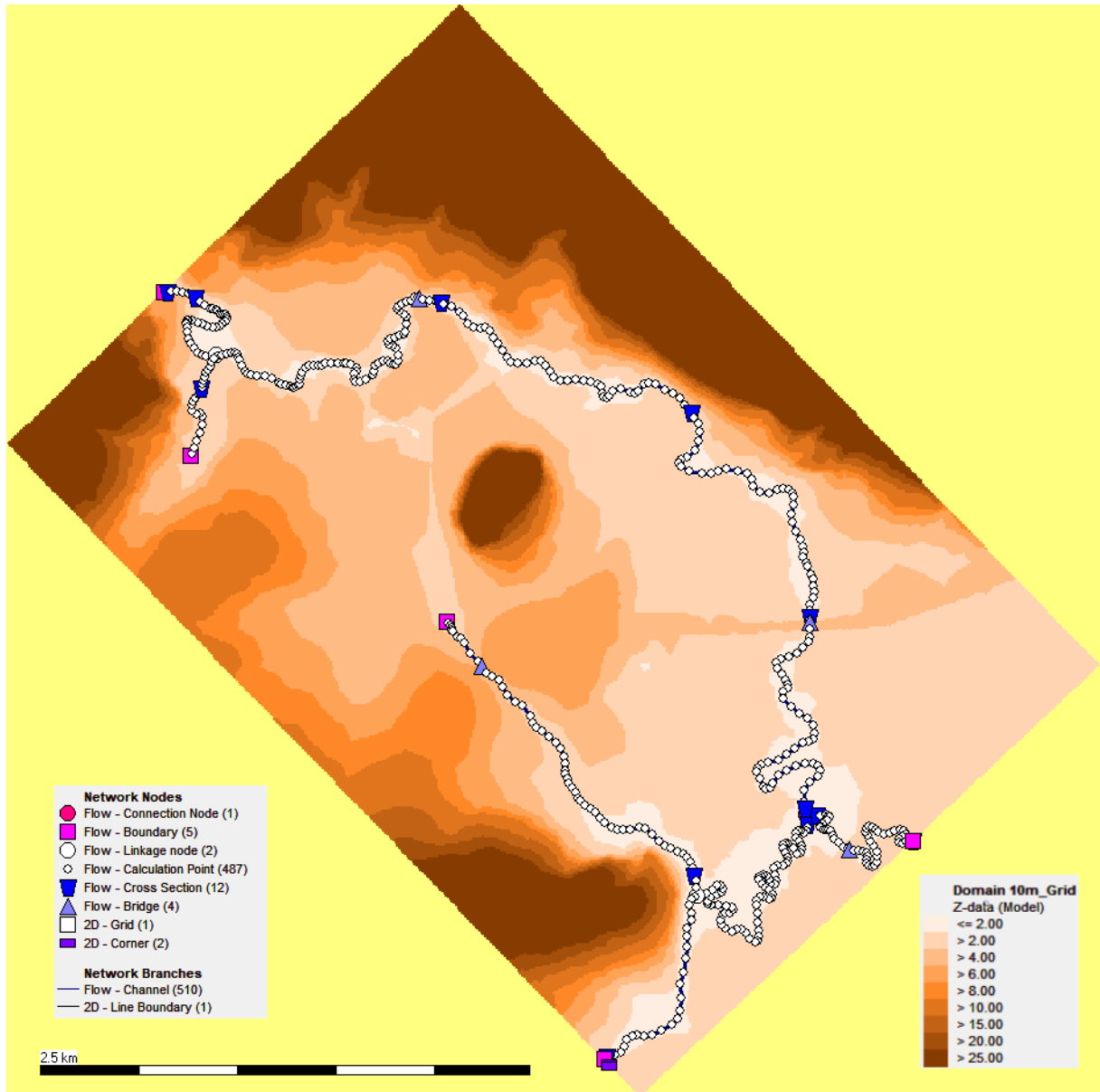


Figure 4-8: 1D2D SOBEK hydrodynamic model schematisation of the model domain

4.4. Tidal data referencing

The datum of the tidal data obtained for the study could not be ascertained from the Tides4fishing website. Also, due to the lack of observed tidal measurement from Ghana, it was a challenge to reference the tidal data employed for the study to the local chart datum. However, due to the tidal intrusion that exists in the peat region where the 2D line boundary was installed, it was assumed that low tides cause water to flow out of the model domain whereas, high tides cause water to enter the model domain. This implied that the average tidal height should match the lowest point of the DEM at the location of the 2D boundary line installation to best simulate tidal water intrusion and withdrawal. As a result, a datum-correction factor (1.06 m) was established to correct the average tidal height. This established factor was used to correct the tidal data used in all the simulations. Figure 4-9 illustrates the assumption made in referencing the tidal data to the elevation at the downstream end of the model domain where the 2D line boundary was installed.

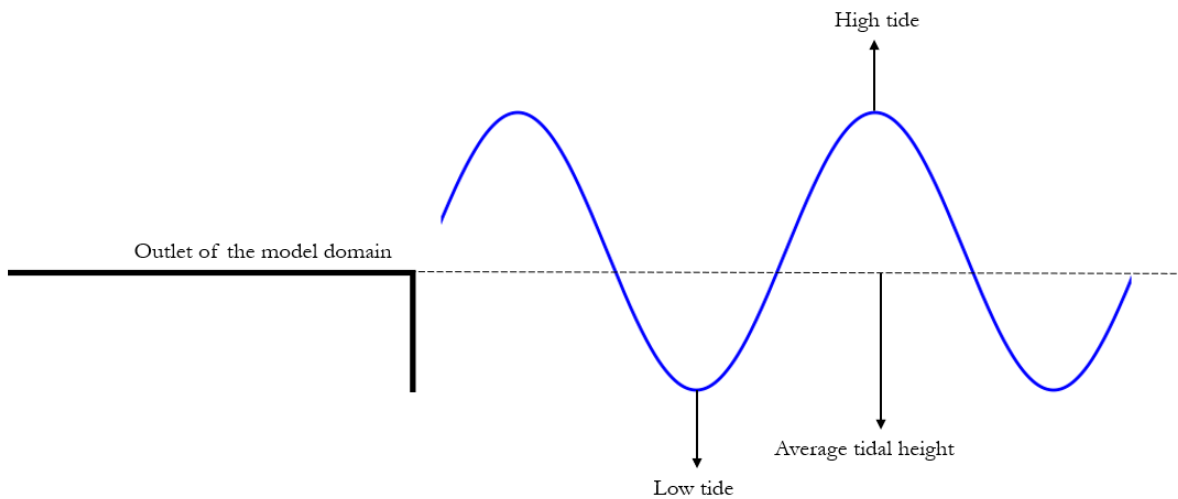


Figure 4-9: Diagram showing the referencing of the average tidal height to the lowest elevation of the DEM where the 2D line boundary was installed

4.5. Model Testing

The schematised 1D2D SOBEK model was tested to assess if the model represented the real world satisfactorily. The low and high flow discharge data of Addae (2018) were sourced to create constant inflow conditions for the 1D-flow boundary node located at the upstream edge of the model domain. Six separate simulations were run for the tests performed using the constant upstream low inflow discharge, the constant upstream high inflow discharge, and tidal data. The tidal data used for the tests was the referenced tidal data from 08/07/2017 at 00:00:00 to 10/07/2017 at 23:00:00, plus an additional water level of 0.94 m. This was to evaluate if the schematised model could handle tidal intrusion that could propagate to the upper part of the model domain. With a computational timestep of one hour, the simulation period for all the model runs was three days. The first simulation was performed with only the tidal data to assess the effect of the tidal intrusion and to assess how far upstream the tides are propagated to cause inundation. Thus, the model was simulated with a constant upstream inflow discharge of 0 m³/s. The second and third simulations were to assess the model simulated inundation due to the applied constant low and high inflow discharges, respectively. For both simulations, the effects of tides were not considered, and as such, the applied boundary condition assigned at the downstream 2D line boundary was a constant ocean water level of 0 m. The fourth simulation involved simulating the model with both the tidal data and the constant low inflow discharge as the upstream boundary condition. The fifth was a simulation with the constant high inflow discharge as the input upstream boundary condition and the tidal data as the downstream boundary condition. Lastly, the sixth simulation employed the use of both the low and high inflow discharges as well as the tidal data. The inflow discharge data for the upstream 1D boundary node was divided into three parts. The first part of the inflow data comprised the constant low inflow for the first simulation day, followed by the constant high inflow for the second simulation day. The third and final part of the upstream inflow discharge data comprised the constant low inflow for the third day of simulation.

4.6. Sensitivity Analysis

The schematisation of the model in this study involved the installation of a 2D boundary line segment at the downstream edge of the model domain to simulate the effects of tidal intrusion on inundation extent. Thus, boundary conditions assigned to the 2D line boundary affects flow across multiple grid cells. However, since the 2D line boundary would influence the model outputs, it was paramount to assess its effects to quantify any related uncertainties. For this purpose, the number of cells used in installing the 2D line boundary was tested while simulating the hydrodynamic model with different inflow discharges. Moreover, for low and high tides, the model's sensitivity was assessed in conjunction with the variations of the number of 2D grid cells as well as the upstream inflow discharges. The number of 2D grid cells used in performing the sensitivity analysis of the model ranged from two to five. The upstream boundary inflows applied in the simulations were constant discharges of 50 m³/s, 100 m³/s and 150 m³/s. A constant low tide of 2.00 m and a constant high tide of 3.70 m were applied to the 2D line boundary. Afterwards, the outputs of the simulations were assessed by comparing the area of inundation obtained as a result of using two 2D grid cells in installing the 2D line boundary to the subsequent simulations of varied 2D grid cells. The comparisons were performed separately by computing the percentage increases between the outputs of the simulations.

4.7. Surface Roughness

Due to the different land cover types present in the model domain, the parameterised surface roughness data from Addae (2018) was employed for model simulations after the model testing and sensitivity analysis were performed. According to Addae (2018), the surface roughness data was produced using a land cover map of the area together with Manning's roughness coefficient values representative of the various land cover types, which were adapted from the study of Medeiros, Hagen, & Weishampel (2012) (see Table 4-1). To ensure that both the DEM and surface roughness raster were of the same spatial extent, the latter was clipped to the extent of the DEM. The surface roughness raster was imported into the NETTER of SOBEK after it was converted into an ASCII file format in ArcMap 10.8.1.

Table 4-1: Manning's roughness coefficient values adapted from Medeiros et al. (2012)

Land cover type	Manning's roughness coefficient
Road	0.010
Bare land	0.018
Open forest	0.022
River	0.030
Wetland	0.045
Shrubs	0.045
Settlement	0.052

4.8. Model Calibration

Model calibration refers to the fine-tuning of a model through operations such as the optimisation of model parameters, modification of the estimation of meteorological inputs, improving the model conceptualisation, and boundary conditions (Rientjes, 2016). Model calibration aims to fit a model simulated output to the observed data. Due to the lack of field observed flood depth and inundation extent, satellite-based surface water maps were considered to serve model calibration. The satellite-based surface water maps were compared to the corresponding model simulated inundation extents and assessed using the critical success index (CSI) described in the study of Grimaldi, Li, Pauwels, & Walker (2016).

The critical success index (CSI) is a performance measure that has been frequently used in many studies that have performed model calibration using satellite-based surface water maps (Grimaldi et al., 2016). CSI measures the fraction of correctly simulated wet pixels. A CSI value of one (1) indicates a perfect fit between a satellite-based surface water map and its respective model simulated inundation extent while a CSI value of zero (0) indicates a poor fit. The computation of CSI is dependent on the construction of a contingency table (see Table 4-2). This contingency table is used to categorise the pixels of the satellite-based surface water maps and simulated inundation extents into wet and dry pixels split by deterministic boundaries.

Table 4-2: Contingency table adapted from Grimaldi et al. (2016)

	Number of wet pixels in the satellite-based surface water map	Number of pixels not wet in the satellite-based surface water map
Number of wet pixels in the model simulated inundation extent	A	B
Number of pixels not wet in the model simulated inundation extent	C	D

Moreover, since the multivariate assessment in the study performed by Addae (2018) proved that the combination of the Sentinel-1 and PlanetScope surface water maps resulted in an improved fit with the model simulated inundation extent, the calibration of the 1D2D Sobek flood model was attempted using the fused surface water map of the model domain produced in subsection 4.1.5. With the aim of fitting the simulated inundation extent to that of the satellite-based map, an attempt was made to vary the surface roughness data used in setting up the 1D2D Sobek hydrodynamic model since Addae (2018) indicated that the model, which was adapted for this study, was sensitive to the surface roughness. Also, since the model was sensitive to the number of 2D grid cells used in establishing the 2D line boundary, the lower limit (two 2D grid cells) was maintained throughout the simulations. The equation used in computing the CSI values for evaluating the various inundation extent comparisons is presented in Table 4-3.

Table 4-3: Information on performance measure used for the inundation extent comparisons adopted from Grimaldi et al. (2016)

Performance Measure	Equation	Range
Critical success index (CSI)	$\frac{A}{A + B + C}$	0 to 1

4.9. Model Simulation with Sea Level Rise Projections

According to the sea level projections documented in the study by Sagoe-Addy & Appeaning Addo (2013), the mean sea level of Ghana is anticipated to rise by 23.4 cm and 36.4 cm by the years 2060 and 2100, respectively. The modelled projections were based on A2 and B2 IPCC climate scenarios. The study's findings are consistent with the sea level rise projection range reported by the Ministry of Foreign Affairs of the Netherlands (2018), in which Ghana's mean sea level is expected to rise between 13 cm to 45 cm in 100 years. Efforts made through literature review to identify a method that relates mean sea level

rise to the increase in tidal amplitude in the coast of Accra and also the coast of West Africa proved futile. As a result, two scenario simulations of flooding in 2060 and 2100 were performed using the sea level rise projections from Sagoe-Addy & Appeaning Addo (2013). The 1D2D SOBEK hydrodynamic model simulations performed to assess the effects of sea level rise on the model domain was executed by increasing the heights of tidal data employed for the study by 23.4 cm for the case of 2060 and 36.4 cm for the case of 2100. The upstream inflow discharge data for 2017 was used for all the scenario simulations. Comparisons of the simulated inundation extents of the current flooding (i.e., without tidal height increase) and that of the simulated inundation extents of the two scenarios were also performed. Afterwards, differences in the simulated inundation extents were assessed based on the change in inundation area as well as the change in average water depths.

5. RESULTS AND DISCUSSION

5.1. Surface Water Mapping

The results of the surface water mapping approach presented in the subsections below were achieved after pre-processing all the Sentinel-1 SAR and PlanetScope optical satellite images employed for the study. The surface water maps produced resulted from the application of the Edge Otsu algorithm and the feature-level image fusion method presented in section 4.1 of this thesis document.

5.1.1. Sentinel-1 Surface Water Mapping

Using SAR imagery to map surface water bodies in urban areas can be challenging due to vertical structures such as buildings and trees. A review of literature revealed that there is no standard SAR surface water mapping method or algorithm guaranteed to achieve the best results. Consequently, the Edge Otsu algorithm, which yielded high accuracies in the study by Markert et al. (2020), was highlighted for mapping surface water in the downstream urban area of the Densu River basin using the Sentinel-1 images. The abbreviations SF25JUN17 and SF07JUL17 represent the Sentinel-1 flood images captured on 25/06/2017 and 07/07/2017, respectively. SD26APR17 and SD24DEC19 also represent the Sentinel-1 dry-weather flow images captured on 26/04/2017 and 24/12/2019, respectively.

5.1.1.1. RGB Composite images

Figure 5-1 below presents the RGB composite images produced from SF25JUN17 and SF07JUL17. The VV polarisation band of SD26APR17 was employed in the production of the two RGB composite images. The RGB composite images aided in distinguishing between permanent water bodies and floodwaters in the study area. The VV polarisation band of SD26APR17 was assigned to the red channel, which implied that a high backscatter response was expected in the channel since the image contained no flooded areas. Also, assigning the VV polarisation band of a flood image to the green and blue channels meant that there would be a low backscatter response in both channels over flooded areas and therefore flooded areas should appear in red. An evenly dark colour was expected over permanent water bodies due to the low backscatter returns in the red, green, and blue channels. Moreover, over surrounding areas where no flood was captured in both the dry and flood images, tones of grey were expected as the backscatter would practically be the same in all the channels. The cyan colour observed in some regions of the RGB composite images can be attributed to other land cover types unrelated to floods. In Figure 5-1, permanent water bodies, namely, the Weija reservoir and the Densu river channel, are shown to have a darker colour while floodwaters are shown in red. Grey tones characterise areas with no water. The RGB composite images produced show floodwaters just along the river channel and not on major parts of the floodplains.

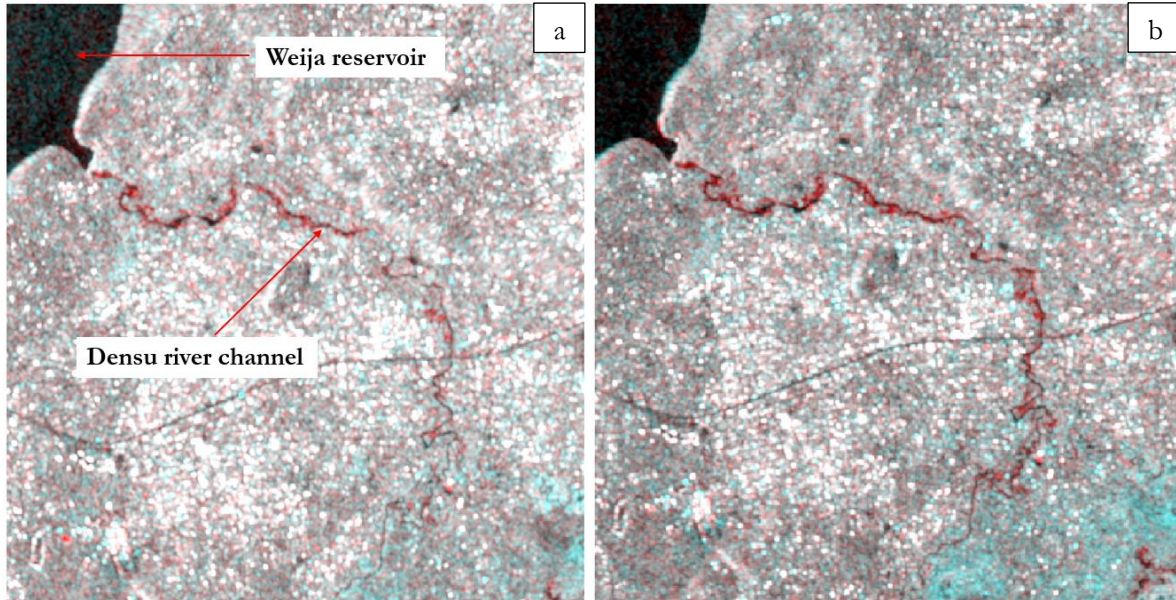


Figure 5-1: Sentinel-1 RGB composites images of floods (a) SF25JUN17 (b) SF07JUL17

5.1.1.2. Application of the Edge Otsu Algorithm on the Sentinel-1 Images

The visual interpretation performed on the pre-processed Sentinel-1 flood and dry-weather flow satellite images and the respective image histograms resulted in the determination of the backscatter threshold values for the initial threshold parameter. The threshold value used for each SAR image was identified between the two peaks of the bimodal image histograms of the respective images. The initial threshold parameter values assigned to the Edge Otsu algorithm to map surface water bodies in SF25JUN17 was -14.69 dB, while that of SF07JUL17 was -14.92 dB. The initial threshold value applied to map surface water bodies in SD24DEC19 was -15.84 dB. Figure 5-2 shows the image histograms of the Sentinel-1 images and the location of the identified backscatter threshold values assigned to the Edge Otsu algorithm. Concerning the edge length parameter of the Edge Otsu algorithm, since the spatial resolution of the Sentinel-1 images employed for the study was 10 m, the parameter was assigned a distance of 10 m in mapping surface water in all the Sentinel-1 images. Assigning a distance of 10 m to the edge length parameter ensured that all detected edges in the binary images created with the initial threshold parameter values were retained.

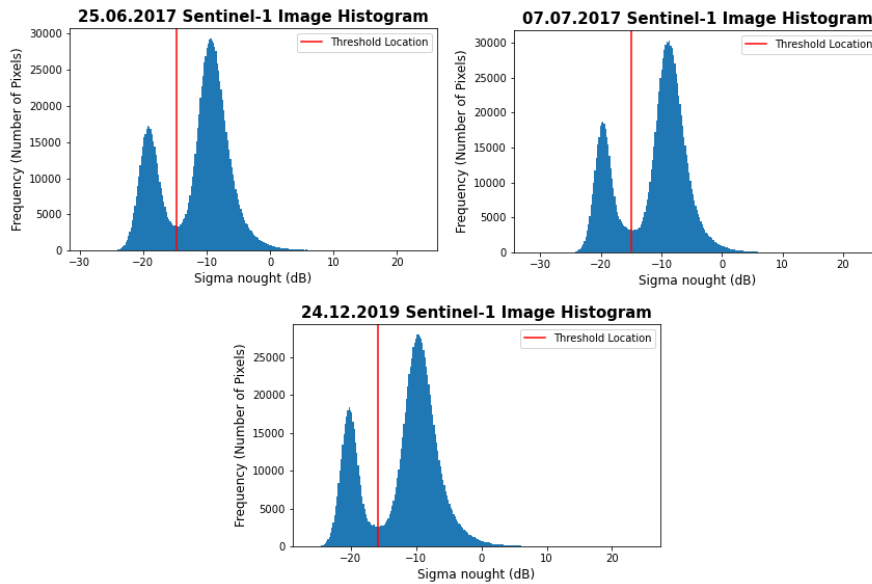


Figure 5-2: Image histograms of the Sentinel-1 flood images (captured on 25/06/2017 & 07/07/2017) and the dry-weather flow image (captured on 24/12/2019)

Figure 5-3 contains graphical illustrations of the sensitivity analysis performed on SF25JUN17 to assess the effects of the edge buffer parameter on the resultant surface water maps. The sensitivity analysis of the parameter was performed because it could not be determined from the various satellite images. By visually assessing the areas bounded by the red squares in Figure 5-3 below, it can be observed that an increase of water pixels in areas that were dry in RGB composite images displayed in subsection 5.1.1.1 began after assigning the Edge Otsu algorithm a distance of 50 m. Table 5-1 contains the results of the comparisons performed between the water masks of the various Sentinel-1 images and their corresponding surface water maps by maintaining the initial threshold and edge length parameters while varying the edge buffer parameter. The findings presented in the table were used in selecting the edge buffer parameter value that resulted in a surface water map with the lowest RMSE when compared to a respective water mask. This resulted in assigning the edge buffer parameter a distance of 40 m to map surface water in SF25JUN17, SF07JUL17 and SD24DEC19. The outcome of the sensitivity analysis and the optimisation of the edge buffer parameter in this section of the study suggests that the optimal parameter value in mapping surface water bodies within the study area using the Edge Otsu algorithm and Sentinel-1 images is 40 m.

Table 5-1: Comparison of Sentinel-1 surface water maps and water masks

Approach	SF25JUN17 (flood)		SF07JUL17 (flood)		SD24DEC19 (dry-weather)	
	Area (km ²)	RMSE	Area (km ²)	RMSE	Area (km ²)	RMSE
Conventional Thresholding (water mask)	34.87		33.47		32.54	
Edge Otsu algorithm (Edge buffer = 10 m)	34.55	0.16	33.34	0.06	32.20	0.17
Edge Otsu algorithm (Edge buffer = 20 m)	34.55	0.16	33.34	0.06	32.20	0.17
Edge Otsu algorithm (Edge buffer = 30 m)	34.55	0.16	33.34	0.06	32.20	0.17
Edge Otsu algorithm (Edge buffer = 40 m)	34.55	0.16	33.34	0.06	32.20	0.17
Edge Otsu algorithm (Edge buffer = 50 m)	35.65	0.39	34.67	0.60	33.14	0.30
Edge Otsu algorithm (Edge buffer = 60 m)	35.65	0.39	34.67	0.60	33.14	0.30

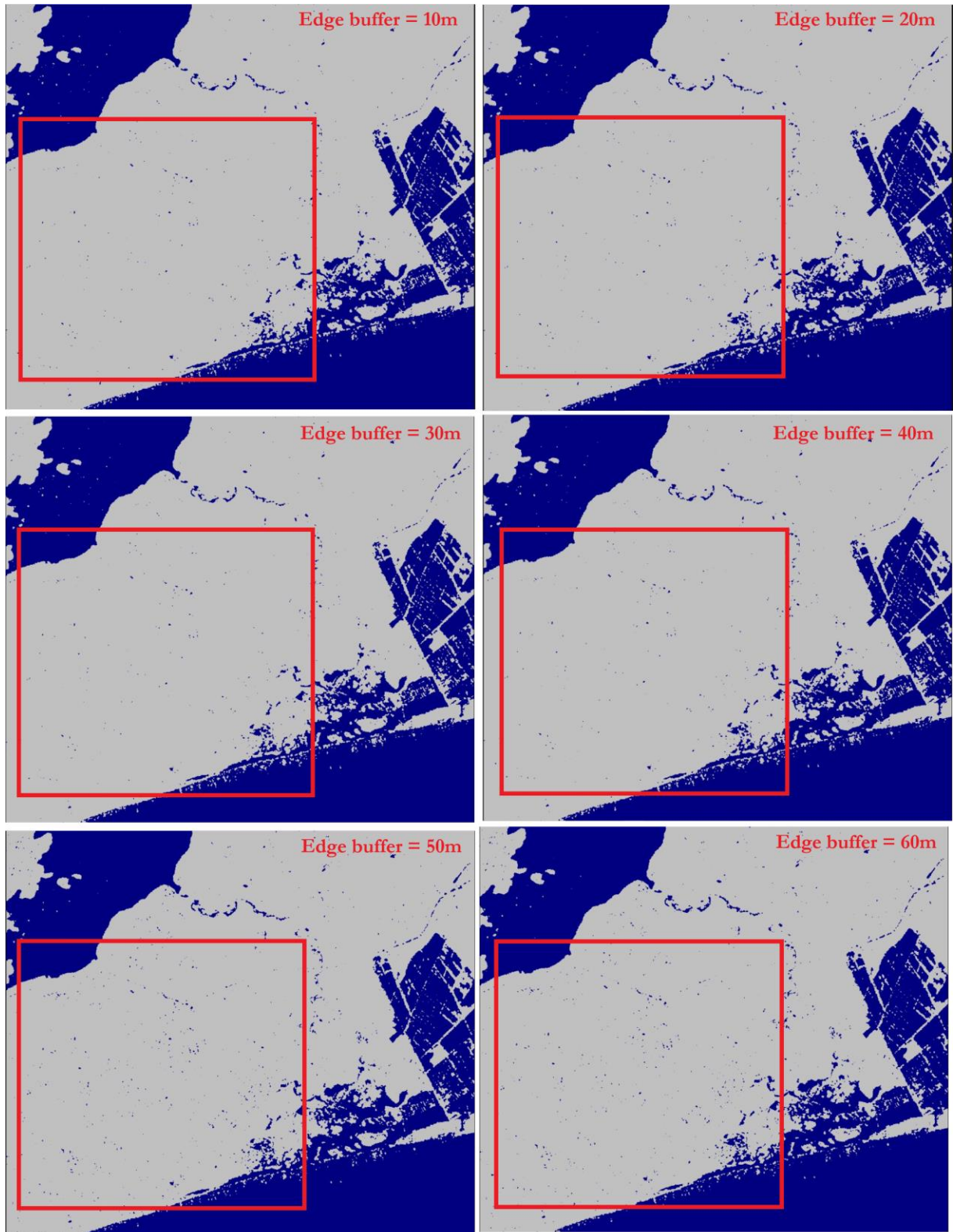


Figure 5-3: Sensitivity analysis performed on surface water maps produced from SF25JUN17

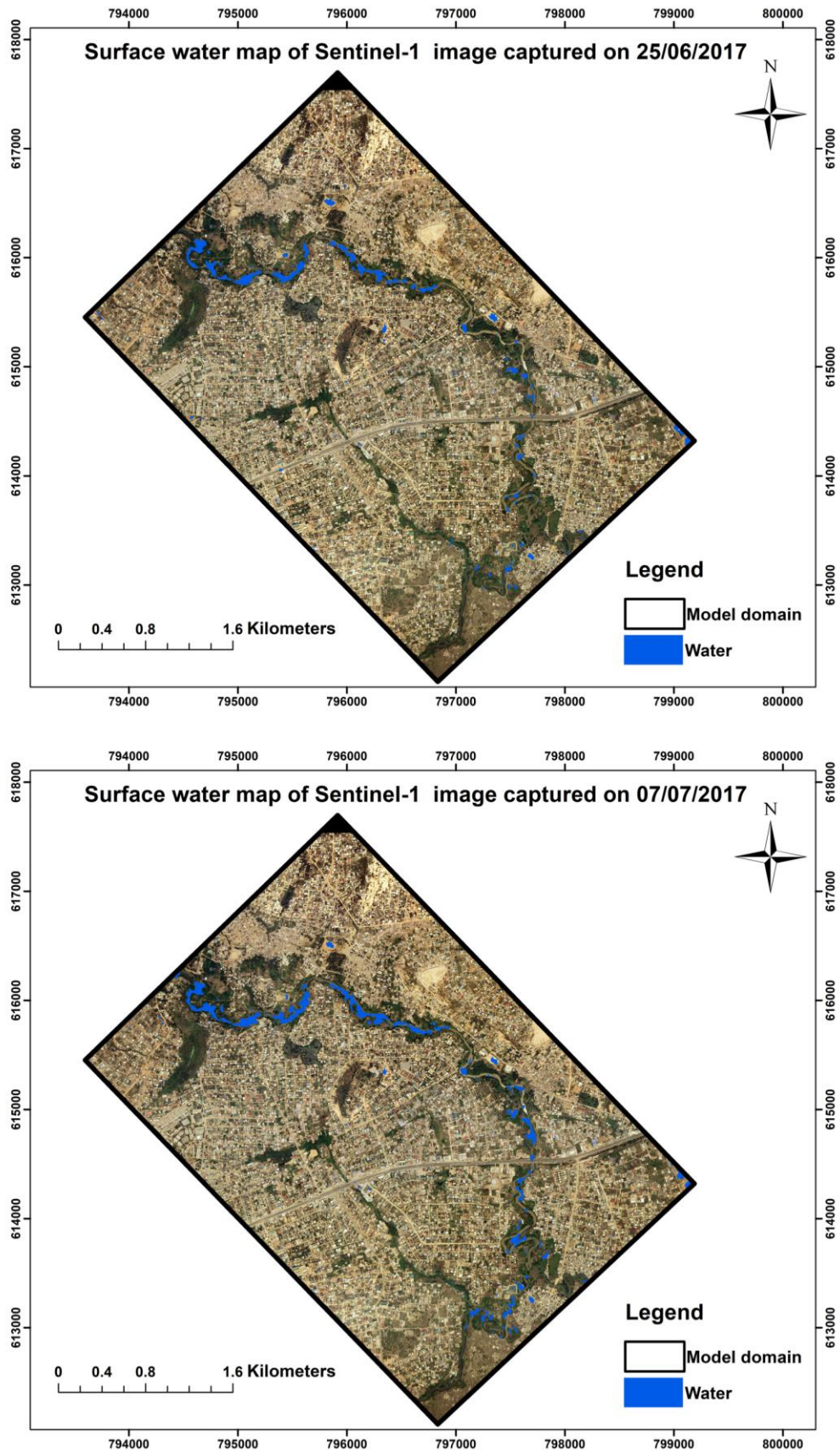


Figure 5-4: Surface water maps of the model domain based on the Sentinel-1 flood images

Figure 5-4 above shows the surface water maps of the model domain produced from the Sentinel-1 flood images. The surface water map of the Densu Delta Wetland is also shown in Figure 5-5. Observations of the Sentinel-1 surface water maps of the model domain show that the number of surface water pixels present in SF07JUL17 was more than that of SF25JUN17. The discontinuous representation of the mapped surface water within the river channel can be attributed to the presence of vegetation, which is known to cause the backscatter returns of regions covered surface water to resemble that of dry regions, as documented by Refice et al. (2018). Furthermore, the few isolated water pixels that were not mapped on the floodplains may have resulted from puddles in the area.

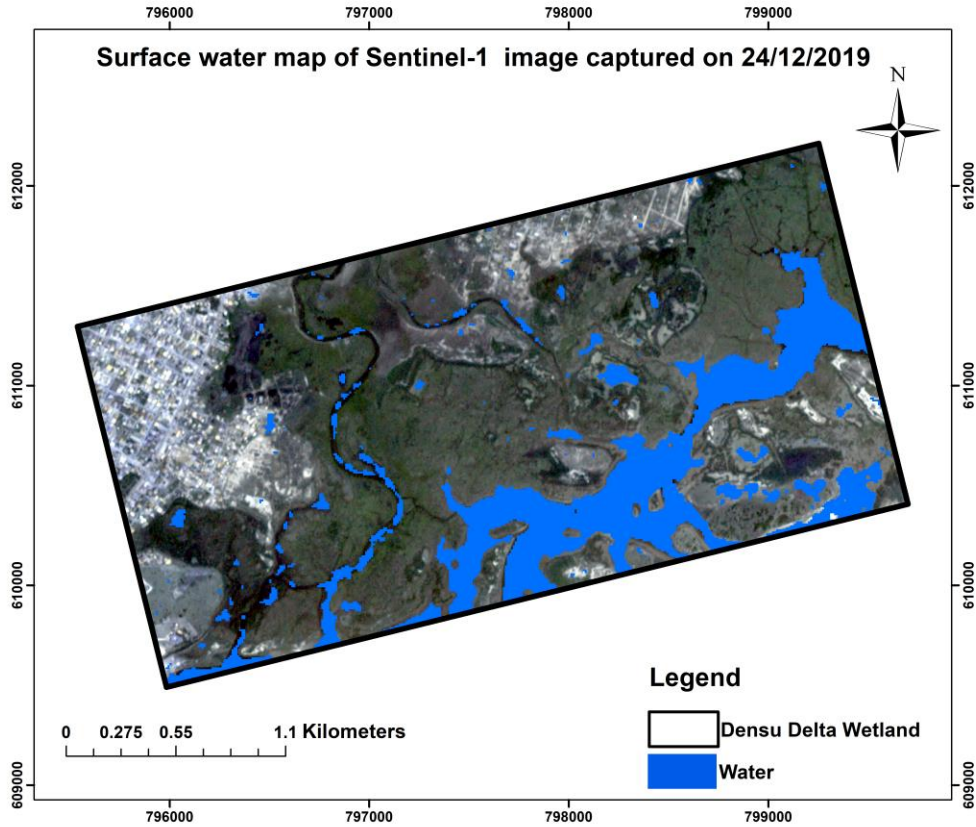


Figure 5-5: Surface water map of the Densu Delta Wetland based on the dry-weather condition captured by the Sentinel-1 SAR satellite image

5.1.2. PlanetScope Surface Water Mapping

The NDWI by McFeeters (1996) is known to be sensitive to buildings and has been often related to overestimating surface water bodies in urbanised regions (Chouari, 2021). The different spectral reflectance of water bodies in different satellite images implies that image segmentation by applying conventional NDWI thresholding values when mapping surface water in urban areas may lead to misclassification. As a result, it is imperative to determine appropriate threshold values for each optical satellite image, as demonstrated in this study, in order to obtain plausible results. The abbreviations PF25JUN17 and PF14JUL17 represent the PlanetScope flood images captured on 25/06/2017 and 14/07/2017, respectively. The PlanetScope dry-weather flow image captured on 24/12/2019 is also represented by PD24DEC19.

5.1.2.1. NDWI Maps

Cloud cover in PF25JUN17 was dominant in the area of the Weija reservoir, making it impossible to assess the NDWI values in that region. The assessment of pixels located within the river channel proved that majority of the pixels had negative NDWI values. There were also widespread similarities between the NDWI values of pixels located in the river channel and buildings in the NDWI map of PF25JUN17. In some parts of the image, the clouds and cloud shadows had similar NDWI values as the water in the river channel. The NDWI map computed with PD24DEC19 also depicted the surface water in the Densu river channel to have negative NDWI values. There were similarities between the NDWI values of built-up areas and surface water in the NDWI map computed from PD24DEC19.

The NDWI map of PF14JUL17 was different. Although there were similarities between NDWI values of water and buildings, the similarities were not widespread, and water in the reservoir, the river channel and the Densu Delta Wetland pixels had positive NDWI values. Also, the NDWI maps from all the PlanetScope optical images showed different NDWI value ranges for surface water. The findings suggested that the spectral characteristics of surface water bodies varied in the various PlanetScope optical satellite images used for the study. Thus, using a single threshold value for all the images may lead to inaccurate satellite-based surface water maps. Among the NDWI maps computed to map surface water within the model domain, PF25JUN17 showed the most similarities between surface water pixels in the river channel and the built-up areas present in the image. Figure 5-6 shows the NDWI maps of PF25JUN17 and PF14JUL17. Part of PF25JUN17, where the Weija reservoir is located, was cropped out due to cloud cover.

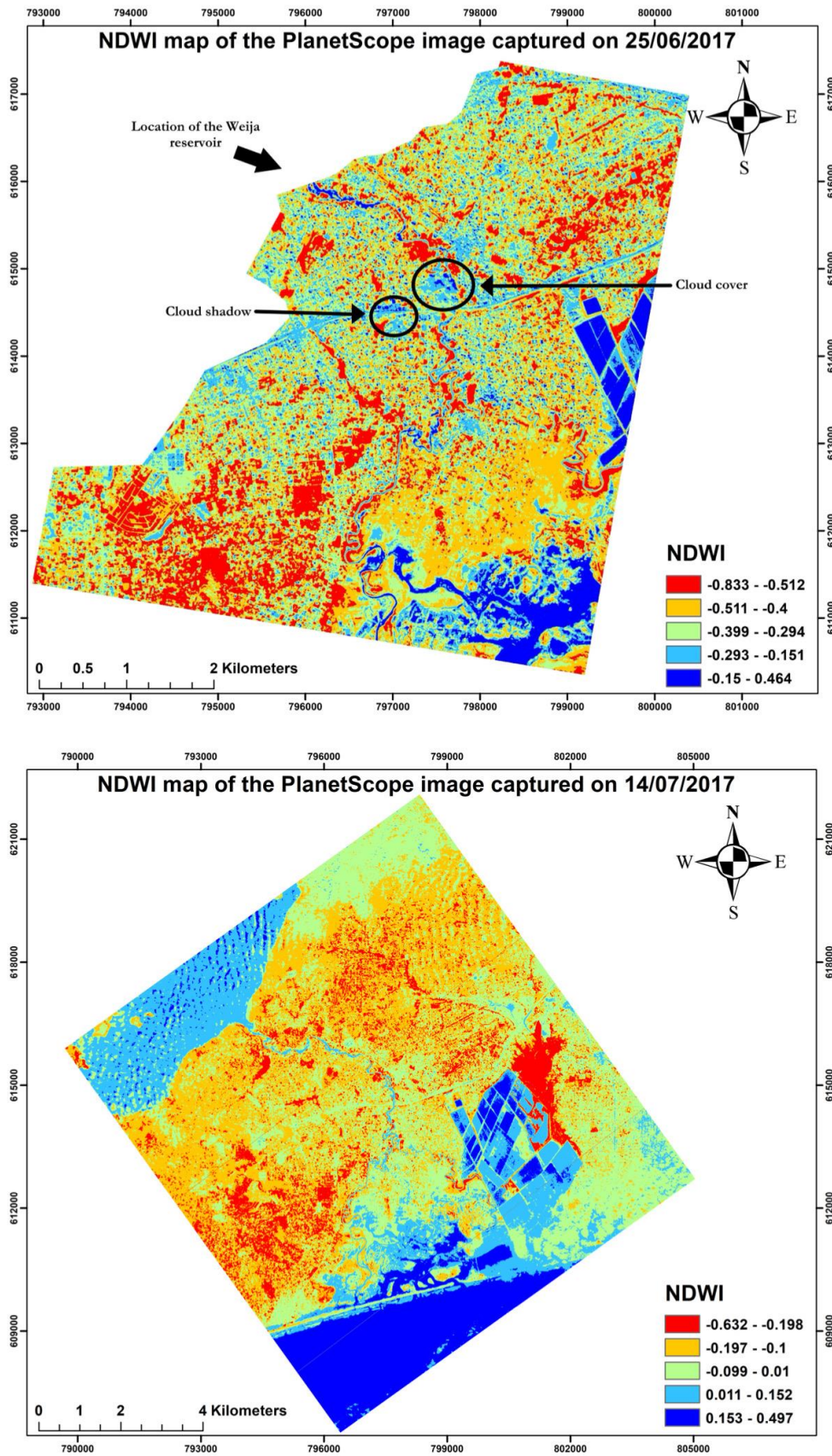
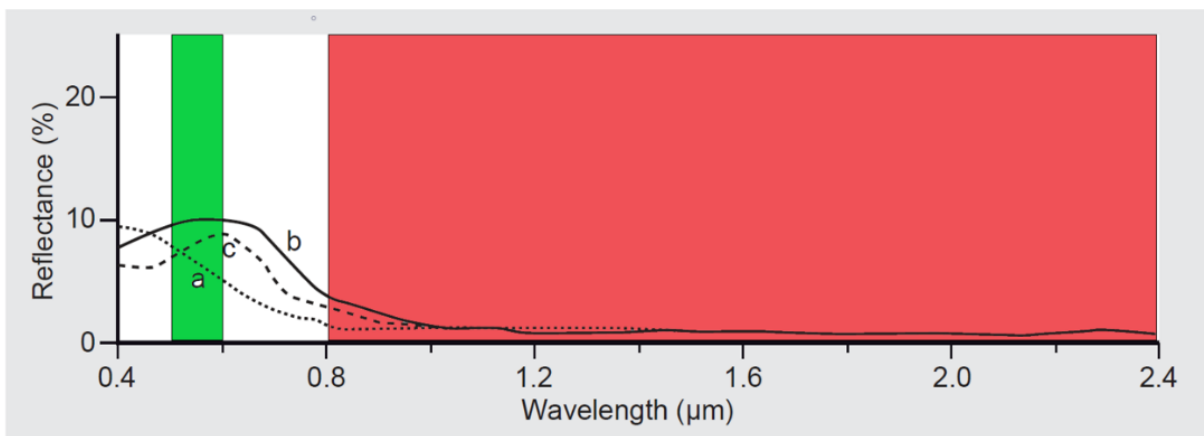


Figure 5-6: NDWI maps of the PlanetScope flood images used in mapping surface water within the model domain

The goal of the NDWI, as proposed by McFeeters (1996), was to enhance regions covered with water by suppressing bare land and vegetated regions. However, in suppressing these land cover types, the spectral index does not eliminate their influence from the outputs produced. Moreover, it was reported by H. Xu (2006) that the spectral index is ineffective in suppressing built-up areas when used to detect surface water in urban areas. Consequently, the enhanced regions covered with water in NDWI maps are detected together with built-up areas. Although this phenomenon was observed with the NDWI maps produced from the PlanetScope images employed for the study, the widespread similarities exhibited in the NDWI map produced from PF25JUN17 was peculiar. After comparing the similarities in the NDWI maps produced from PF25JUN17, a surface reflectance image, and PF14JUL17, a top-of-atmosphere reflectance image, it was necessary to know why the two maps were so different. An examination of the spectral reflectance values in the green and near-infrared (NIR) bands of the two optical images was executed to ascertain the cause of this outcome.

The pixel-by-pixel assessment performed on spectral reflectance values of a number of pixels in the bands revealed that the reflectance values of water pixels in the green band of PF25JUN17 were higher than that of the same pixels in the NIR bands. However, the reflectance of water in the NIR band should be lower than in the green band since water reflects electromagnetic radiation better in the visible range than in the NIR range. Also, electromagnetic radiation is better absorbed in the NIR range of the electromagnetic spectrum than in the visible range. This is further explained in Figure 5-7, as the different spectral reflectance signatures of different water compositions, namely, water containing sediments, water containing chlorophyll, and ocean water, show spectral reflectance values of water to be higher in the green band than in the NIR band.



Legend

- | | |
|---|----------------------------|
| ■ Wavelength of green band | a - Ocean water |
| ■ Wavelength of near-infrared (NIR) band | b - Turbid water |
| | c - Water with chlorophyll |

Figure 5-7: Spectral reflectance signatures of different compositions of water adapted from (ITC, 2013)

The spectral reflectance of other land cover types such as soil, built-up areas and vegetation exhibit spectral reflectance values in green and NIR infrared bands that contrast the spectral reflectance of water as shown in Figure 5-7. The reflectance in the NIR band is higher than that of the green band in these mentioned land cover types. This was the case of the NDWI map produced from PF14JUL17 presented in Table 5-2. The reflectance pattern of water in the green and NIR bands of PF25JUN17 resulted in the widespread equivalence in the NDWI values of water and non-water surfaces as shown and evaluated in Figure 5-6 and Table 5-2, respectively. Since PF25JUN17 is a surface reflectance product, it was

challenging to ascertain why the spectral reflectance of pixels located in regions covered with water was higher in the NIR band than in the green band. Also, all the pixels used for the assessment were cloud-free. This suggests that the cause of the unconventional spectral reflectance of water in the green and NIR bands as exhibited in PF25JUN17 may be due to defects within the satellite image.

Table 5-2: Pixel-by-pixel assessment of spectral reflectance values in the PlanetScope flood images

Point	PF25JUN17			PF14JUL17		
	Band	Reflectance	NDWI	Band	Reflectance	NDWI
Water pixels						
1	Green	998	-0.09	Green	1440	0.07
	Near-infrared	1187		Near-infrared	1261	
2	Green	976	-0.09	Green	1514	0.04
	Near-infrared	1167		Near-infrared	1393	
3	Green	827	-0.22	Green	1452	0.09
	Near-infrared	1287		Near-infrared	1201	
Built-up pixels						
1	Green	2566	-0.11	Green	1936	-0.12
	Near-infrared	3211		Near-infrared	2472	
2	Green	1695	-0.24	Green	1702	-0.01
	Near-infrared	2789		Near-infrared	2060	
3	Green	1959	-0.17	Green	1666	-0.01
	Near-infrared	2789		Near-infrared	2033	

5.1.2.2. Application of the Edge Otsu Algorithm on the PlanetScope Images

Due to the similarities between NDWI values of surface water bodies and some land cover types, especially buildings in all the NDWI maps created, it was impossible to fully segment surface water in all the PlanetScope optical satellite images. As a result, determining the NDWI threshold values to segment the satellite images through the pixel-by-pixel assessment was challenging. From the evaluations performed in all the NDWI maps, the identified pixels within the reservoir and the river channel with minimum NDWI values were used as initial threshold values for mapping surface water with the Edge Otsu algorithm. Consequently, the initial threshold values used were -0.29 for PF25JUN17 and 0.01 for PF14JUL17. The initial threshold value used for PD24DEC19 was -0.14.

Since the spatial resolution of the PlanetScope optical satellite images was 3 m, the edge length parameter of the Edge Otsu algorithm was assigned a distance of 3 m for all the optical images processed. This was done with the aim of not eliminating any detected edge. The sensitivity analysis performed to assess the edge buffer parameter's effect of resultant PlanetScope surface water maps enabled the optimisation of the parameter. The sensitivity analysis of the edge buffer parameter resulted in assigning different values to the parameter to map surface water on the PlanetScope images. Table 5-3 shows the comparison performed between the water mask of the various PlanetScope images and their respective surface water maps produced by varying the edge buffer parameter while keeping the other two parameters fixed. The edge buffer parameter values applied in mapping surface water in PF25JUN17, PF14JUL17 and PD24DEC19 were 100 m, 3000 m and 900 m, respectively. These selected edge buffer parameter values resulted in surface water maps with the lowest RMSE when compared to the respective water masks produced using the manual thresholding method in ArcMap 10.8.1.

Table 5-3: Comparison of the PlanetScope surface water maps and water masks

Approach	PF25JUN17		PF14JUL17		PD24DEC19	
	Area (km ²)	RMSE	Area (km ²)	RMSE	Area (km ²)	RMSE
Conventional thresholding (water mask)	6.77		34.84		26.90	
Edge Otsu algorithm (Edge buffer = 100 m)	9.72	1.47	40.05	2.60	34.44	3.77
Edge Otsu algorithm (Edge buffer = 200 m)	10.04	1.64	38.43	1.79	32.59	2.85
Edge Otsu algorithm (Edge buffer = 300 m)	11.11	2.17	37.60	1.38	31.00	2.05
Edge Otsu algorithm (Edge buffer = 400 m)	11.87	2.55	37.60	1.38	29.66	1.38
Edge Otsu algorithm (Edge buffer = 500 m)	12.61	2.92	36.88	1.02	28.53	0.82
Edge Otsu algorithm (Edge buffer = 600 m)	12.61	2.92	36.20	0.68	27.42	0.26
Edge Otsu algorithm (Edge buffer = 700 m)	12.61	2.92	36.20	0.68	27.42	0.26
Edge Otsu algorithm (Edge buffer = 800 m)	12.61	2.92	36.20	0.68	26.90	0.00
Edge Otsu algorithm (Edge buffer = 900 m)	12.61	2.92	36.20	0.68	26.90	0.00
Edge Otsu algorithm (Edge buffer = 1000 m)	12.61	2.92	36.20	0.68	26.40	0.25
Edge Otsu algorithm (Edge buffer = 2000 m)	12.61	2.92	35.51	0.33	25.50	0.70
Edge Otsu algorithm (Edge buffer = 3000 m)	12.61	2.92	35.51	0.33	25.50	0.70

The use of different edge buffer parameters in the application of the Edge Otsu algorithm in mapping surface water bodies in the PlanetScope images may have resulted from the disparities in the NDWI value ranges of water computed from each of the satellite images. The surface water maps of the model domain produced from the PlanetScope flood images are shown in Figure 5-8.

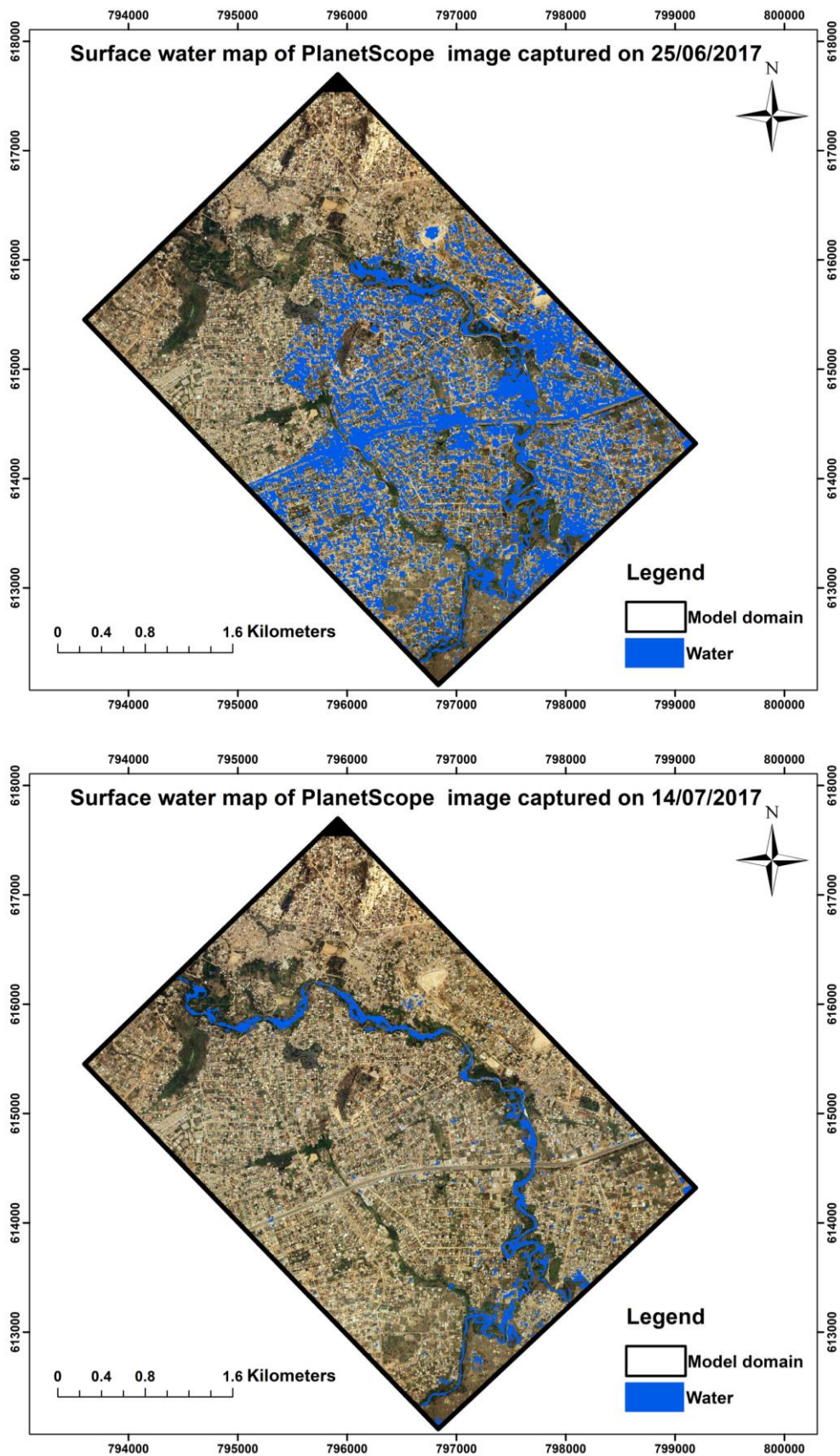


Figure 5-8: Surface water maps of the model domain based on the PlanetScope flood images

The surface water maps produced from PF25JUN17 and PF14JUL17 showed that although the Edge Otsu algorithm mapped surface water in the Weija reservoir and the river channel, scattered clusters of pixels were observed on the floodplains. The misclassification of built-up areas as surface water was dominant in the surface water map created from PF25JUN17. Even roads were mapped as water. This indicates the degree to which other land cover types had similar NDWI values as the surface water in the river channel. Also, clouds and shadows that covered parts of the satellite image were mapped as water. The findings indicate the sensitivity of the Edge Otsu algorithm to input data, as documented by Markert et al. (2020). Also, there were scattered water pixels in the upper-left corner of the surface water map of PD24DEC19, where buildings are located. The majority of the scattered pixels in the surface water maps created with the PlanetScope images were verified as buildings when compared to the true colour composites of the various images. The surface water map of the Densu Delta Wetland is presented in Figure 5-9 below.

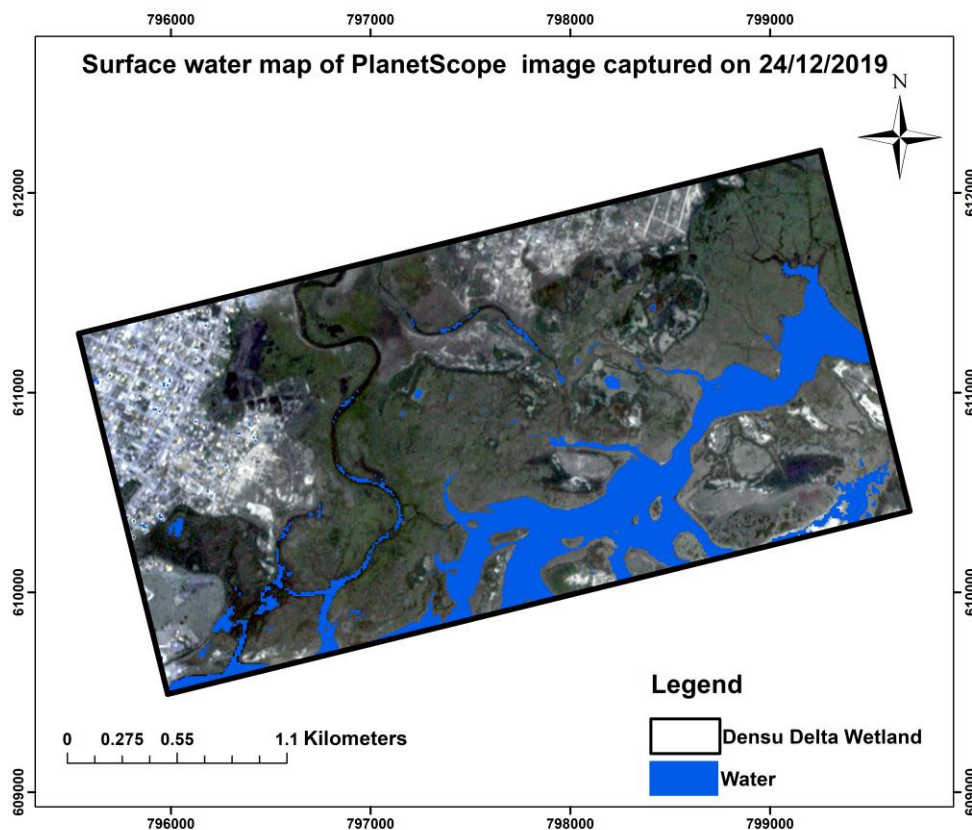


Figure 5-9: Surface water map of the Densu Delta Wetland based on the dry-weather condition captured by the PlanetScope optical satellite image

5.1.3. HAND Filtering

Figure 5-10 shows the HAND created from the 10 m resolution DEM. The extraction of the drainage network from the flow accumulation raster was executed using a threshold value of 23,544. This threshold value was determined manually by classifying the flow accumulation lines into five (5) classes and then using visual interpretation and prior knowledge of the model domain through the processing of the satellite images to select the minimum value in the flow accumulation class range that depicts the actual flow lines. It was observed from the analysis of the 10 m resolution DEM that the lowest elevation (i.e., 2 m) runs from the upstream edge of the model domain to the downstream outlet on the left-hand side. The HAND was used to reduce the misclassification of surface water that occurred during the application of the Edge Otsu algorithm. The filtering process involved limiting surface water detection and mapping to flood-prone areas within the model domain. No HAND filtering operations were performed on the

surface water maps created for the Densu Delta Wetland. This was due to the lack of a HAND filter for the area. However, this did not significantly affect the surface water maps as the misclassification of water pixels observed in the surface water map produced from PD24DEC17 was not widespread since the number of the misclassified water pixels were not many (see Figure 5-9).

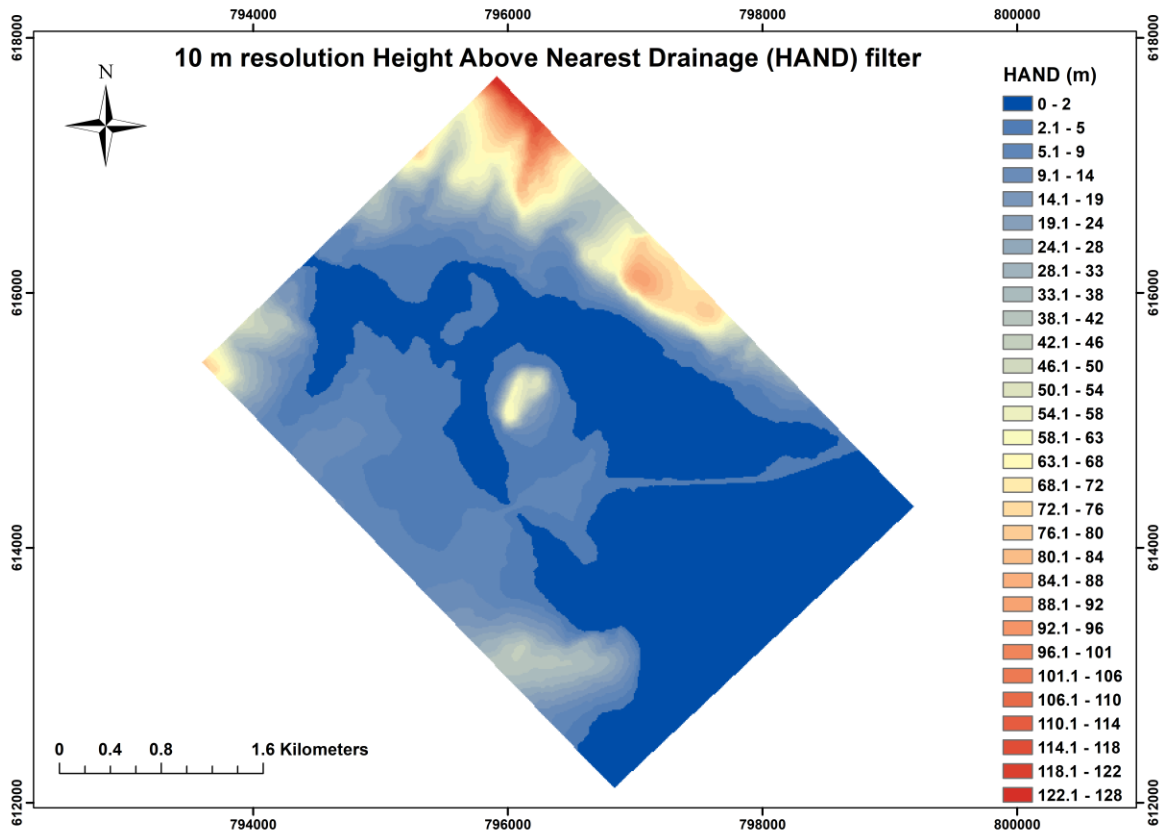


Figure 5-10: Map of HAND filter created using the 10m resolution DEM.

The surface water maps of the model domain for the Sentinel-1 and PlanetScope satellite images after the HAND filtering operations are shown in Figure 5-11 and Figure 5-12, respectively. The surface water maps produced due to the HAND filtering processes performed on the sentinel-1 and PlanetScope images show no water pixel at elevations higher than the defined HAND threshold elevation. The HAND filtering approach improved the surface water maps produced from the flood images of both the PlanetScope and Sentinel-1 satellite images. As shown in Figure 5-11, the isolated water pixels that were not mapped on the floodplains as shown in Figure 5-4 were filtered from the surface water map produced from the Sentinel-1 flood images (SF25JUN17 and SF07JUL17). Also, from the filtered surface water maps produced from the PlanetScope flood images (PF25JUN17 and PF14JUL17) shown in Figure 5-12, it can be observed that some of the scattered clusters of water pixels located in the built-up areas on both sides of the Densu river channel were reduced. The findings indicate the created 10 m resolution HAND filter’s ability to improve the surface water mapping operations executed with the Edge Otsu algorithm by effectively eliminating detected water pixels that were unrealistic or were not floodwaters.

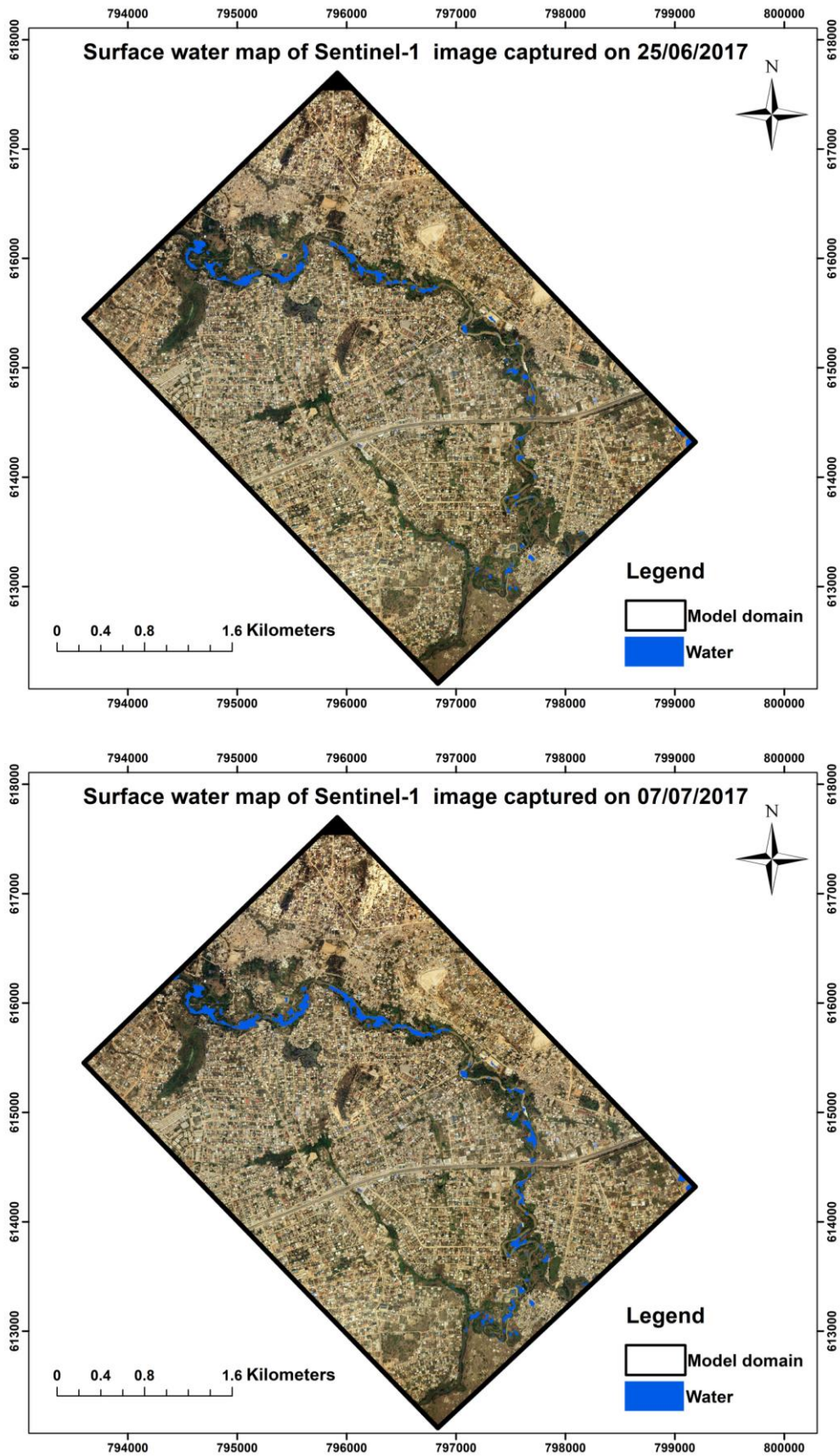


Figure 5-11: Filtered surface water maps of the model domain based on the Sentinel-1 flood images

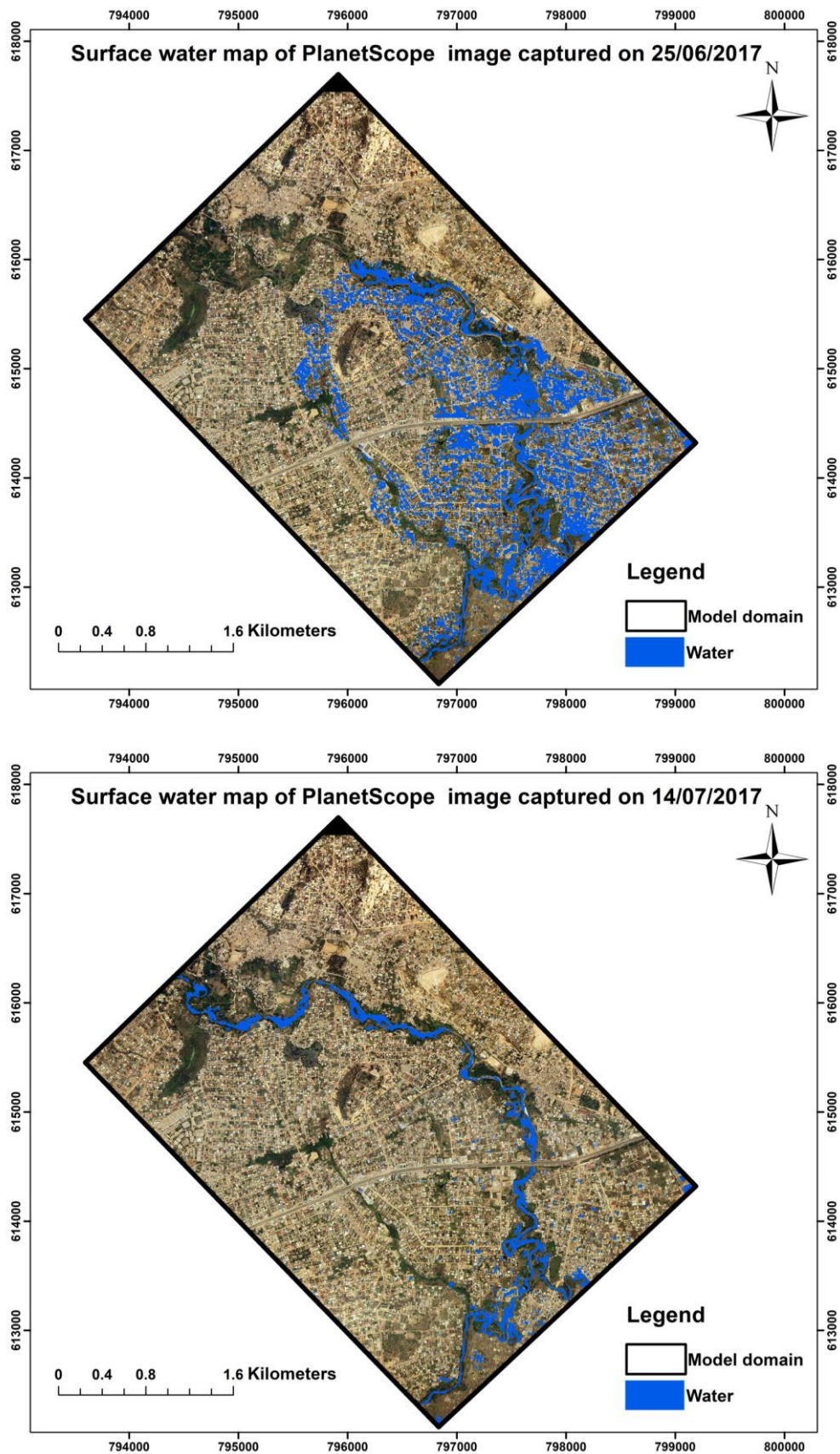


Figure 5-12: Filtered surface water maps of the model domain based on the PlanetScope flood images

5.1.4. Evaluation of Surface Water Maps

Using visual interpretation, the reference data used in assessing the surface water maps produced were delineated from PF14JUL17 and PD24DEC19. The HAND filtered surface water map of PF14JUL17 and the surface water maps of the Densu Delta Wetland produced from SD24DEC19 and PD24DEC19 were evaluated individually. The overall classification accuracy of the surface water map created from PF14JUL17 was 86.14%, with a Kappa coefficient of 0.69. Regarding the Densu Delta Wetland, the overall accuracies of the surface water maps created from SD24DEC19 and PD24DEC19 were 84.16% and 90.10%, respectively. The Kappa coefficient of SD24DEC19 was 0.69, while that of PD24DEC19 was 0.80.

As per the results of the assessments performed, the accuracy of the surface water map of PF14JUL17 was satisfactory despite the misclassified water pixels observed in the built-up areas, as shown in Figure 5-12. Although the surface water map of PD24DEC19 performed better than that of SD24DEC19, the overall classification accuracies and Kappa coefficients achieved in mapping surface water bodies within the Densu Delta Wetland were high. As documented by Notti et al. (2018), spatial resolution is a factor that determines the potential of a satellite image in mapping surface water. Therefore, the difference in the accuracy of the surface water map of SD24DEC19 and PD24DEC19 can be attributed to the medium spatial resolution (10 m) of the Sentinel-1 satellite image. Overall, the findings of the accuracy assessments highlight the Edge Otsu algorithm's ability to produce surface water maps of high accuracy. The results of the accuracy assessments, especially the surface water maps of the Densu Delta Wetland, are similar to the accuracies achieved in the study by Markert et al. (2020).

5.1.5. Sentinel-1 and PlanetScope Image Fusion

SF25JUN17 and PF25JUN17 were not fused due to the large cloud cover (see Appendix A) and widespread NDWI similarity of surface water and built-up areas present in the NDWI map of PF25JUN17. The supervised classification performed for the fusion of SF07JUL17 and PF14JUL17 resulted in an overall classification accuracy of 97% and a Kappa coefficient of 0.93. The important features for classification performed in descending order were the NIR band, the NDWI band, the VV polarisation band and the blue band. Likewise, the VH polarisation, green and red bands followed. The findings showed an improvement in the accuracy of the surface water map produced from PF14JUL17 as per the accuracy assessment results documented in the previous section. However, by visually inspecting the surface water map created, few scattered water pixels located in dry areas can be seen similar to the surface water map of PF14JUL17 in Figure 5-8. For this reason, the HAND filter produced in the study was used to process the fused surface water map further to reduce the misclassified water pixels detected on high elevations. The overall classification accuracy of the surface water map of the Densu Delta Wetland produced from SD24DEC19 and PD24DEC19 was 98% and had a Kappa coefficient of 0.97. As per the accuracy assessment results, the accuracies achieved using the individual images were improved due to the fusion approach. Also, the misclassified water pixels present in the upper-left corner of the surface water map produced from PD24DEC19 shown in Figure 5-9 were not present in the surface water map produced from the fused image. The classification's important features or variables in descending order were the NIR band, the NDWI, the green band, and the VV polarisation band. The red band, VH band and blue band follow in the same order.

Although the fusion method improved the accuracy of the surface water maps produced from each of the images involved in the fusion operations, the results suggested that the visual appearance and the accuracy of the resultant fused surface water map significantly depended on the input data. This was due to the misclassification of surface water bodies observed in the fused surface water map produced from SF07JUL17 and PF14JUL17. The high accuracy and satisfactory representation of water and non-water regions in the fused surface water map of the Densu Delta Wetland suggested that the small built-up area

in PD24DEC19 did not affect the classification as shown in the fused surface water map produced from SF07JUL17 and PF14JUL17. PD24DEC19 was also cloud-free, and this may have influenced the classification results. Figure 5-13 and Figure 5-14 show the image fusion approach employed for the study.

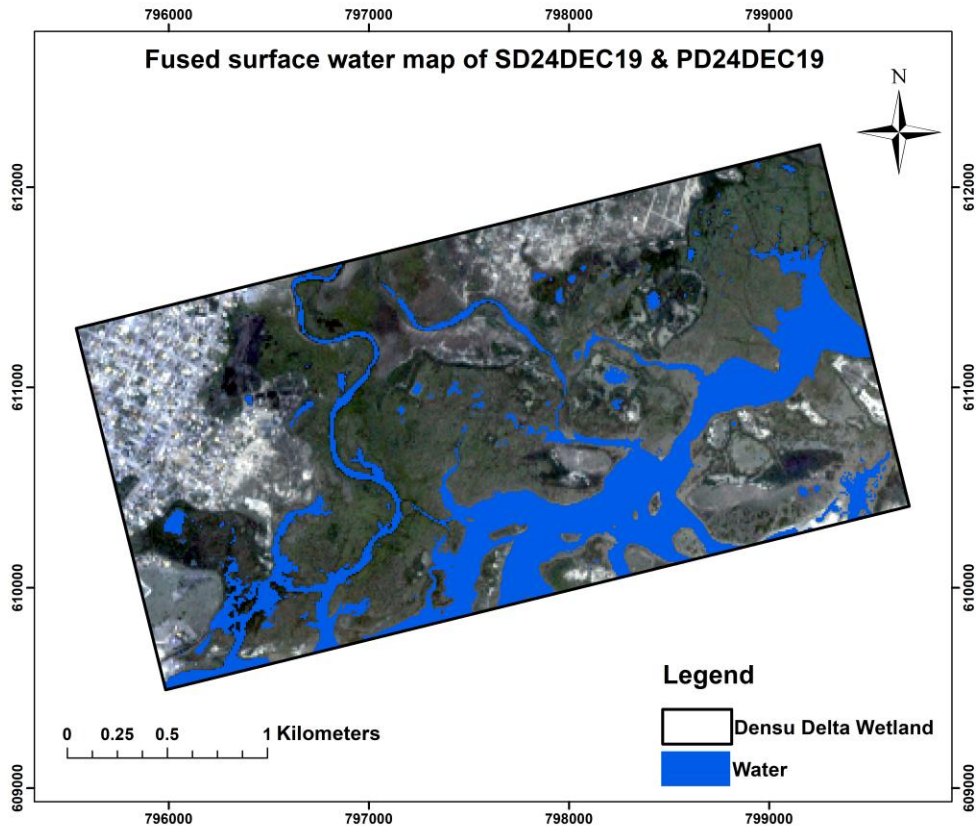


Figure 5-13: Surface water map of the Densu Delta Wetland based on the fusion of the Sentinel-1 and PlanetScope dry-weather flow images

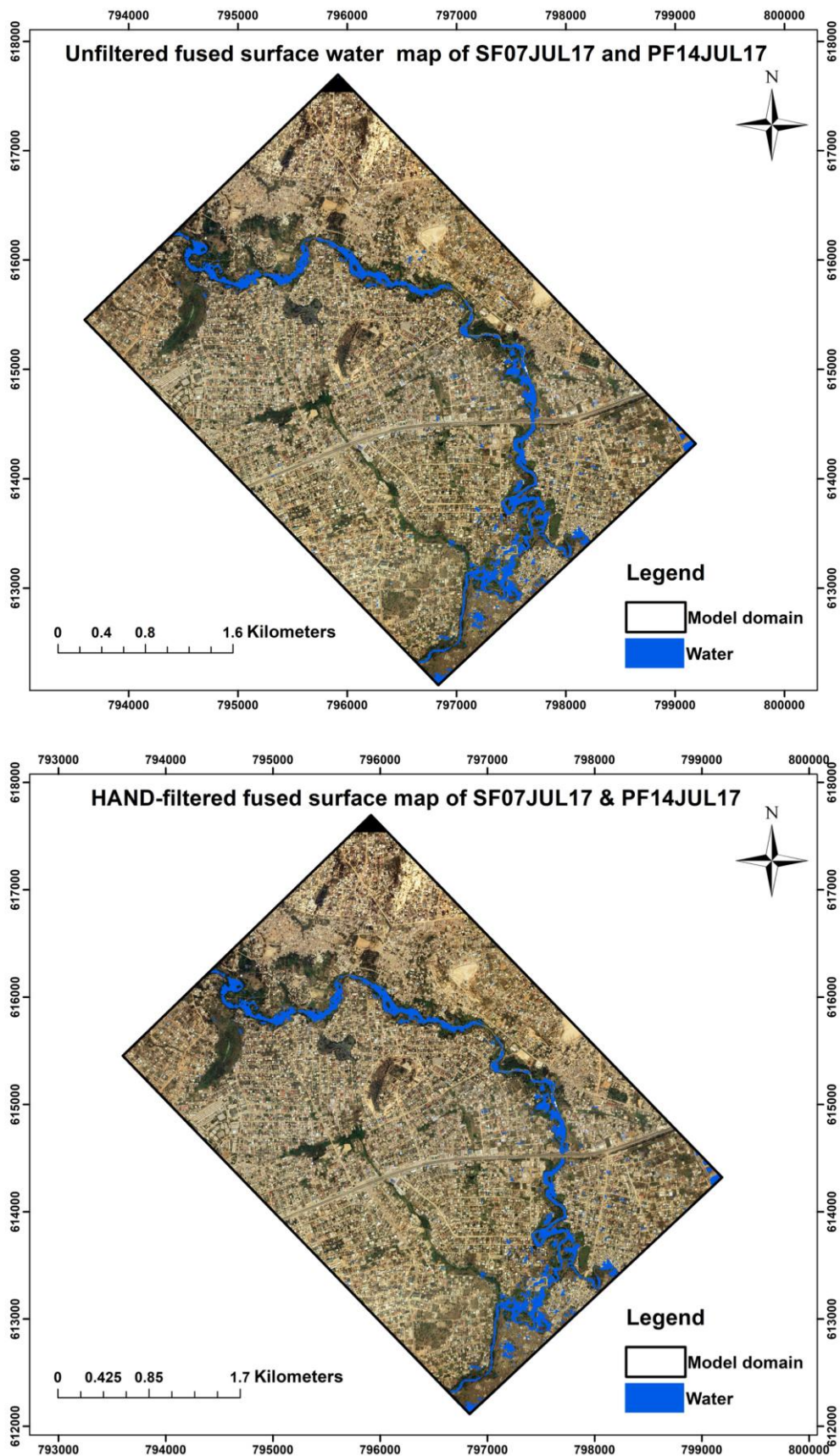


Figure 5-14: Surface water maps of the model domain based on the fusion of the Sentinel-1 and PlanetScope flood images

5.2. Hydrodynamic Modelling

5.2.1. Model Testing

The model test runs were performed to assess if the behaviour of the schematised model represented real-world flow processes and to assess the impacts and extent of sea-water intrusion within the model domain. Model testing is essential in establishing trustworthiness in the schematisation of a model, and as such, this step was a prerequisite in setting up the 1D2D SOBEK hydrodynamic model to produce meaningful results. The results of the different simulations executed with the constant low inflow data, the constant high inflow data and the tidal data as boundary conditions are presented in maps below. The animations of each testing simulation were visually inspected to evaluate the schematisation's correctness and to draw conclusions. The outcome of the simulation with only the tidal data is presented in Figure 5-15. The figure shows the inundation extents and water depths at low and high tides. Also, the animation of the results indicates a more significant water depth during high tides. As shown in the figure, the tidal effects as per the tidal data applied show tidal intrusion to the upstream region of the model domain. The intrusion of the tides high up the model domain may have resulted from the domain's flat terrain.

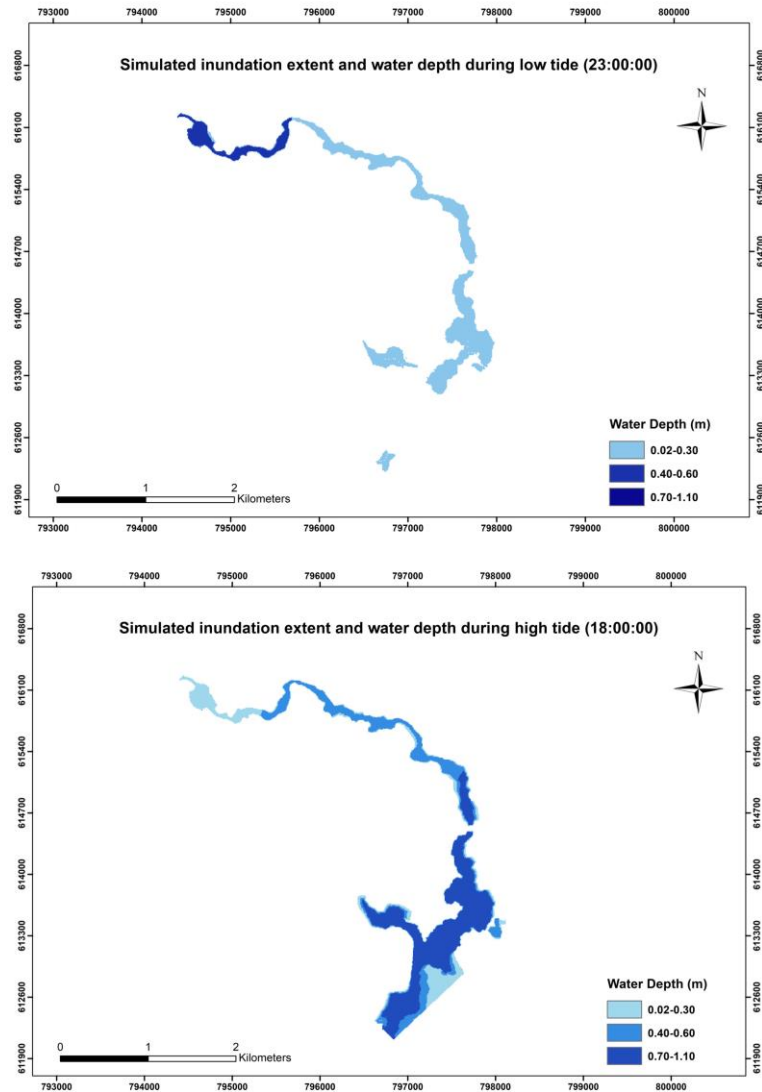


Figure 5-15: Maps showing the simulated inundation extents and water depths during low and high tides without inflow discharges

As seen in Figure 5-16, the assessment of the results obtained using the constant low and high inflow discharges and the tidal water level of 0 m indicate different inundation extents. As was expected, the area inundated as a result of the high inflow discharge was more extensive than that of the low inflow discharge, which indicated the model's ability to simulate different upstream boundary conditions appropriately.

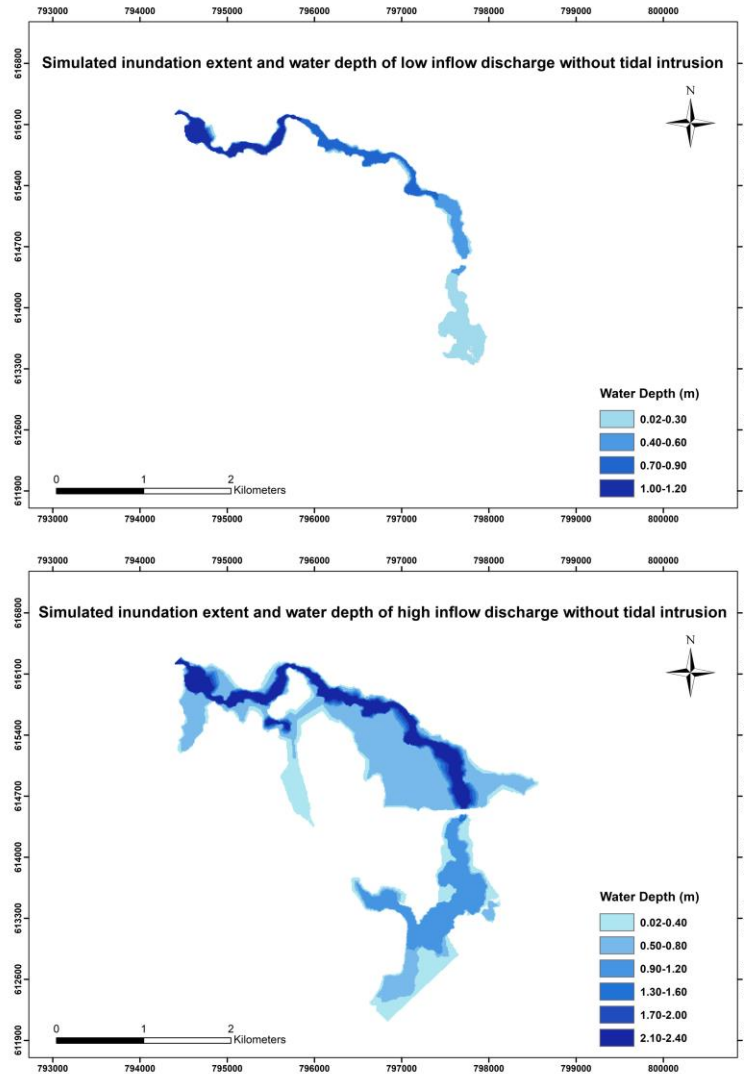


Figure 5-16: Maps showing the simulated inundation extents of low and high inflow discharges without tidal intrusion

The subsequent separate simulations with the upstream inflows of constant low flow and tidal data as well as constant high flow and tidal data all resulted in increased inundation extents. The findings indicated the model's plausible response to both the upstream inflows and the tides from the downstream edge of the model domain. Figure 5-17 shows the results of separately simulating the model with the constant low inflow discharge and the tidal data as well as simulating the model with the constant high inflow discharge and the tidal data.

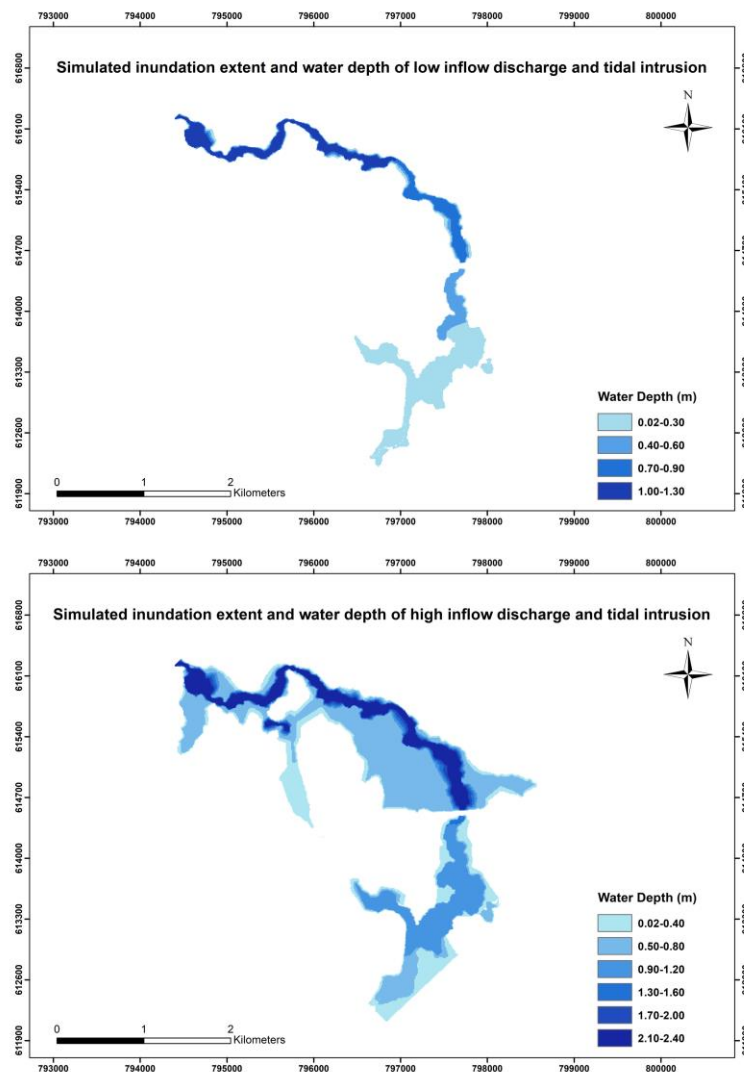


Figure 5-17: Maps showing the simulated inundation extents and water depths of low and high inflow discharges and tidal intrusion

Lastly, simulating the 1D2D SOBEK model with discharge data containing both constant low and high inflow discharges and the tidal data resulted in inundation extents and water depths similar to the ones shown in Figure 5-17. The maps obtained for the first and third simulation days were similar to the inundation extent and water depths as presented in the map of the low inflow discharge and the tidal intrusion. This was due to the constant low inflow discharge used for both days. The constant high inflow discharge used for the second simulation day also resulted in an inundation extent and water depths similar to the inundation extent presented in the map of the high inflow discharge and the tidal intrusion. The model test findings indicated the potential of the model to produce plausible results representative of real-world flow processes within the model domain. Water was observed to overtop the river channel banks and to inundate the floodplains (2D grid) once the model simulated water levels were higher than the bank heights of the river branches. The inundation on the 2D grid cells receded with water flowing to the channel when the flood levels dropped. This was evident in the last model test simulation with inflow discharge containing constant low and high inflow discharge data and the tidal data at the downstream edge of the model domain.

5.2.2. Sensitivity Analysis

The changes in inundation area due to the variations of the number of 2D grid cells showed that the model was sensitive to the number of 2D grid cells used installing the 2D line boundary as well as the low and high tides. The results of the sensitivity analysis performed are presented in Figure 5-18. From the figure, it can be observed that there was a significant difference in results obtained using constant high tide data as opposed to using the constant low tide data. The results of the comparisons performed between the simulated inundation extents as a result of varying the number of 2D grid cells used in installing the 2D line boundary are presented in Table 5-3. Concerning the results obtained from the simulation with the inflow discharge of 50 m³/s and the constant high tide data, the inundation area increased by around 6% after the number of 2D grid cells used in installing the 2D line boundary was increased from two to three. Increasing the number of 2D grid cells to five increased the inundation area by around 9%. Also, increasing the number of 2D grid cells from two to four increased the inundation area by some 7%. Similarly, the results obtained using the same inflow discharge and the low tide data resulted in changes in the inundation area. However, the changes were not significant as the increase of the 2D grid cells from two to five increased the inundation area by less than 1%.

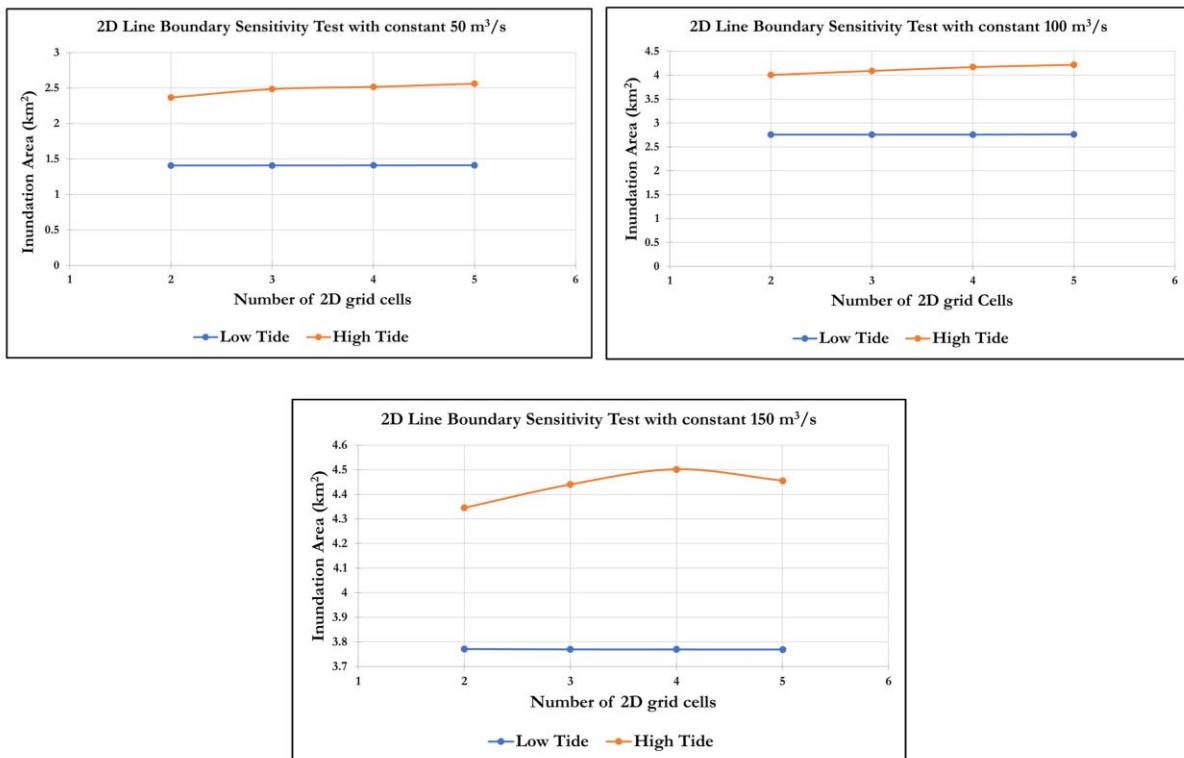


Figure 5-18: Scatter plots of the sensitivity analysis results

For the simulations using a constant inflow discharge of 100 m³/s and constant high tide data, an increase in the number of 2D grid cells from two to three increased the inundation by around 2%. The inundation area increased by a little above 4% after increasing the number of 2D grid cells from two to four and by around 6% after increasing the 2D grid cells from two to five. There were no increases in the inundation area after increasing the number of 2D grid cells from two to three and two to four and simulating the model with constant inflow discharge of 100 m³/s and constant low tide data. Also, it can be seen from the table that there was a relatively insignificant increase in the inundation area after increasing the number of 2D grid cells from two to five.

The final set of simulations involving the constant inflow discharge of 150 m³/s and the constant high tide data and the constant low tide data showed slight overall increases in the inundation area. Regarding the simulations that were executed using the inflow discharge data and the low tide data, increasing the 2D grid cells from two to three and then from two to four increased the inundation area by less than 1%. Increasing the number of 2D grid cells from two to five resulted in an inundation increase of less than 1%. Concerning the simulations executed using the constant inflow discharge of 150 m³/s and the constant high tide data, the inundation area increased by around 3% when the number of 2D grid cells was increased from two to three. Increasing the number of 2D grid cells from two to four increased the inundation area by around 4%. The inundation area increased by 3% when the number of 2D grid cells used to install the 2D line boundary increased from two to five, which was lower than the inundation area obtained after increasing the number of 2D grid cells from two to four.

Table 5-4: Results of the inundation area comparisons

Upstream inflow discharge = 50 m ³ /s				
Number of Cells	Low Tide		High Tide	
	Area of Inundation (km ²)	Percentage Increase (%)	Area of Inundation (km ²)	Percentage Increase (%)
2	1.4067		2.3638	
3	1.4087	0.14	2.4843	5.10
4	1.4099	0.23	2.5165	6.46
5	1.4123	0.40	2.5615	8.36
Upstream inflow discharge = 100 m ³ /s				
Number of Cells	Low Tide		High Tide	
	Area of Inundation (km ²)	Percentage Increase (%)	Area of Inundation (km ²)	Percentage Increase (%)
2	2.7582		4.0069	
3	2.7582	0.00	4.0912	2.10
4	2.7583	0.00	4.1698	4.07
5	2.7587	0.02	4.2186	5.28
Upstream inflow discharge = 150 m ³ /s				
Number of Cells	Low Tide		High Tide	
	Area of Inundation (km ²)	Percentage Increase (%)	Area of Inundation (km ²)	Percentage Increase (%)
2	3.7711		4.3448	
3	3.7696	0.04	4.4398	2.19
4	3.7693	0.05	4.5018	3.61
5	3.7689	0.06	4.4555	2.55

5.2.3. Model Results

The simulation period used in all the cases constructed in the study was three days. This was due to the lengthy computational time that would have been encountered in simulating a single case with discharge data spanning a period of three and half weeks. The simulation period employed for the cases is similar to that of Addae (2018). Also, after the first simulation was executed, restart files were used as initial data in all the subsequent simulations. This was to maintain simulation states by continuing successive simulations

from the last computation timesteps of previous simulations. The results obtained from the 1D2D SOBEK hydrodynamic simulations are represented in Figure 5-19.

In Figure 5-19, all the simulated inundation extents show a more extensive inundation at the upstream area above the road (as indicated in Figure 5-21) than the downstream section of the model domain. The water accumulation at the upstream section of the model domain resulted from the high inflow discharge from the reservoir spillage and the size of the channel under the bridge through which flow is transported to the downstream region (see Figure 5-21). The findings suggested that the large volumes of water released from the reservoir on the specific days and times indicated on the maps below were larger than that volume that could be transported underneath the bridge without a backwater effect. Moreover, in simulated inundation maps produced from low inflow upstream discharges, the water accumulation shown in the figure below were not observed.

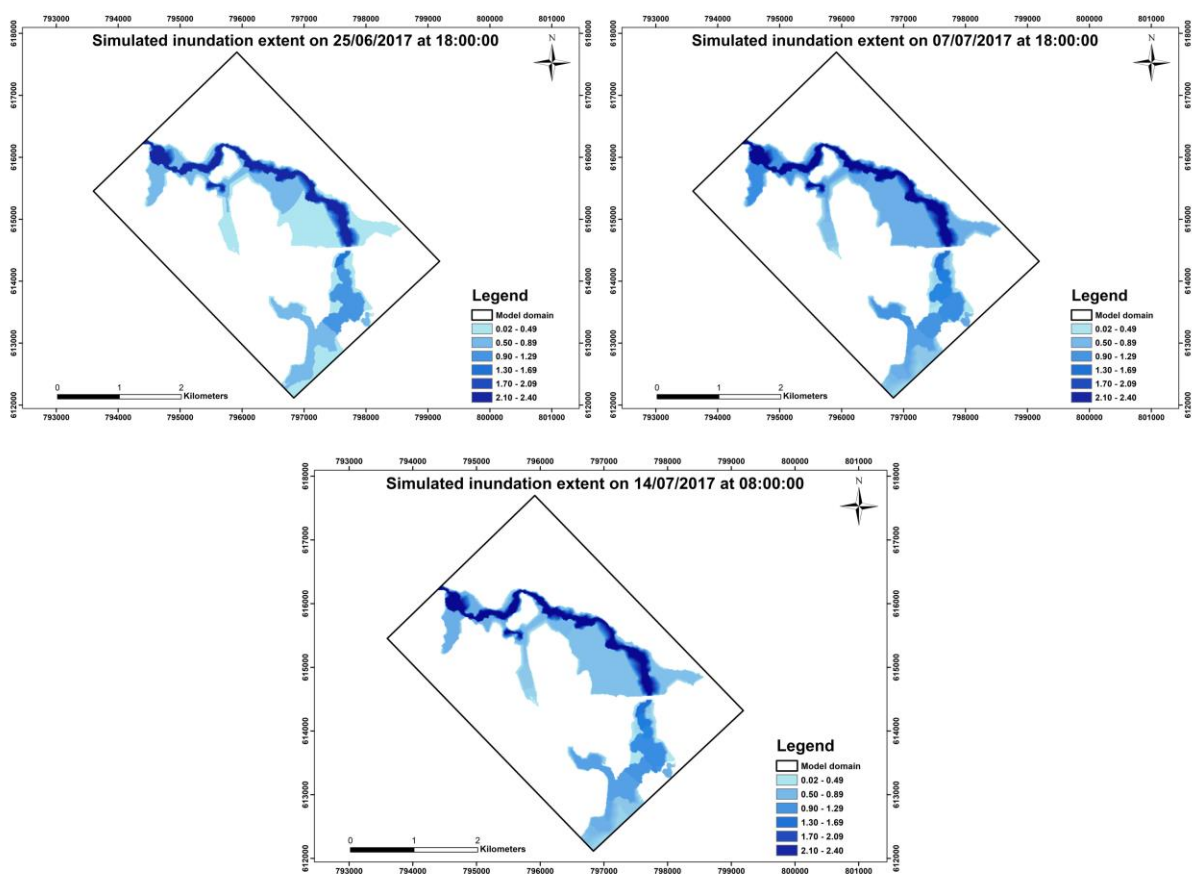


Figure 5-19: Simulated inundation extents

It can also be observed in Figure 5-19 that all the simulated inundation extents show high water depths greater than 2 m within the river channel where water is accumulated in the upstream region of the model domain. This is explained by the low elevation of the river channel in the region as compared to the surrounding terrain. The low elevation of the river channel caused inundation in the channel to be greater than the surrounding areas. Overall, the simulated inundation extents produced from the 1D2D SOBEK hydrodynamic model were plausible and representative of the data used to build and simulate the model.

5.2.4. Comparison of satellite-based surface water maps and model simulation inundation extents

A specific objective of this study was to compare the fused satellite-based surface water map with the respective model simulated inundation extent to calibrate the 1D2D SOBEK hydrodynamic model in order to achieve the main objective of the study, which was to assess the effects of sea level rise on the downstream coastal urban area of the Densu River Basin in Accra. The satellite-based surface water maps produced from the individual satellite images except for the map produced from PF25JUN17 were also compared to the respective simulation inundation maps.

The comparison of the satellite-based surface water map and the respective model simulated inundation extents was executed based on the time at which the various satellite images were captured. The surface water map produced from the Sentinel-1 flood image captured on 25/06/2017 at 18:17:47 (SF25JUN17) was compared to the model simulated inundation extent of the same day but at 18:00:00 due to the hourly computation timestep of the model outputs. Similarly, since SF07JUL17 was captured on 07/07/2017 at 18:18:05, the surface water map produced from this satellite image was compared to the simulated inundation extent of 07/07/2017 at 18:00:00. The same criterion was used to compare the satellite-based surface water map produced from the PlanetScope optical satellite image captured on 14/07/2017 and at 07:57:12. Later, using a multivariate comparison, the fused multi-temporal satellite-based surface water map created from SF07JUL17 and PF14JUL17 was compared to the corresponding model simulated inundation extents. The critical success index (CSI) was used as the performance measure to assess the fit between the outputs of the satellite images and the hydrodynamic model. The summarised results of the comparison made between the satellite-based surface water maps and the respective simulated inundation extents are presented in Table 5-5.

Table 5-5: Results of the satellite-based surface water maps and simulated inundation extent comparisons

Satellite Image	Number of wet pixels in both satellite-based surface water map and simulated inundation extent	Number of pixels that were not wet in satellite-based surface water but wet in simulated inundation extent	Number of pixels that were not wet in simulated inundation extent but wet in the satellite-based surface water map	CSI
Comparison of Sentinel-1 satellite-based surface water maps and simulated inundation extent				
SF25JUN17	1316	37790	168	0.03
SF07JUL17	1935	38589	137	0.05
Comparison of PlanetScope satellite-based surface water map and simulated inundation extent				
PF14JUL17	4083	34418	506	0.10
Multivariate assessment of fused satellite-based surface water map and simulated inundation extents				
SF07JUL17 & PF14JUL17	5089	35432	447	0.12

From Table 5-5, it can be observed that with a CSI value of 0.10, the model simulated inundation extent produced on the 14/07/17 at 08:00:00 showed the highest fit amongst all the single model simulated inundation extents examined in the study. Also, as per the multivariate assessment performed, a CSI value of 0.12 was obtained when the fused multi-temporal satellite-based surface water map produced from SF07JUL17 and PF14JUL17 was compared to the corresponding model simulated inundation extents.

The maps in Figure 5-20 below show the comparisons made between the satellite-based surface water maps and the respective simulated inundation extents.

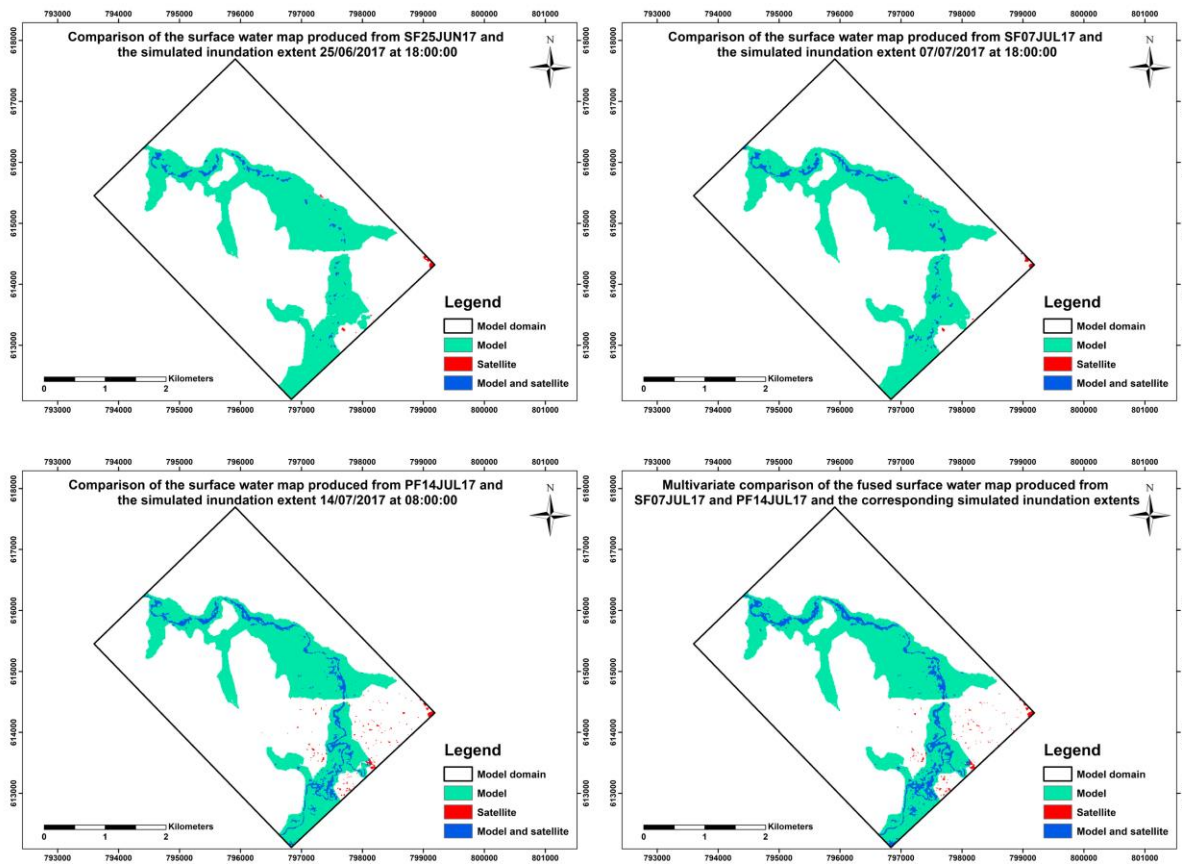


Figure 5-20: Maps showing the comparisons made between satellite-based surface water maps and simulation inundation extents

The comparison findings revealed that the fit between the satellite-based surface water maps and the model simulated inundation was not satisfactory, and thus the satellite-based surface water maps could not serve model calibration. These findings are in contrast to that of Addae (2018), as the satellite-based surface water maps produced in that study matched better with the simulated inundation extents than in this study. A major cause of the differences in the findings of the two studies is the significant difference in the satellite-based surface water maps produced.

The poor misfit of the satellite-based surface water maps and the simulated inundation extents produced in this study can be attributed to factors in both map types. The satellite surface water mapping phase of the study produced surface water maps with satisfactory accuracy based on the quantitative accuracy assessments performed. However, a number of factors can be identified to have contributed to uncertainties in the satellite-based surface water maps. An example is the misclassification of water pixels in the maps produced from the PlanetScope optical images as per the visual inspections performed. Another factor can be observed in the surface water maps produced from the Sentinel-1 images, as the overall representation of the river channel was not continuous since patches of dry land within the course of the river were observed in the maps. However, such uncertainties could only have affected the fit to a minimal degree as the differences between the surface water maps produced from the Sentinel-1 images and the corresponding inundation extents from the model was significant. The large degree of misfit is

also evident in the comparison made between the fused satellite-based surface water map produced from SF07JUL17 and PF14JUL17 and the corresponding simulation inundation extents.

The processes that were undertaken in setting up the 1D2D SOBEK hydrodynamic model adapted from Addae (2018) also resulted in model outputs that were representative of the forcing applied to the model as per the model testing performed. The model was able to handle low and high inflows from the upstream boundary node as well as the tidal intrusion at the downstream end of the model domain. However, the large inundation shown by the simulated inundation extents in Figure 5-20 can be attributed to DEM employed for schematising the model. An examination of the map in Figure 5-21 shows that the immediate elevation (4 m) higher than the elevation of the river channel (2 m) can be seen to cover a large region. As a result, when surface water in the river channel overtops the banks, it would not take time for the inundation of a large region to occur. This is evident in all the simulated inundation extents shown in Figure 5-19. The large inundation at the upper part of the model domain beyond the road can be seen to cover the regions with elevations between 2 m to 4 m. Also, the DEM used lacked the representation of vertical surface features such as buildings that predominantly covered the model domain, and as such, the restriction to flow that these features could have caused were not considered in all the simulations. A careful examination of the satellite images (see Appendix B) employed for the study shows that surface water in the various satellite images is not widespread as the model predicted.

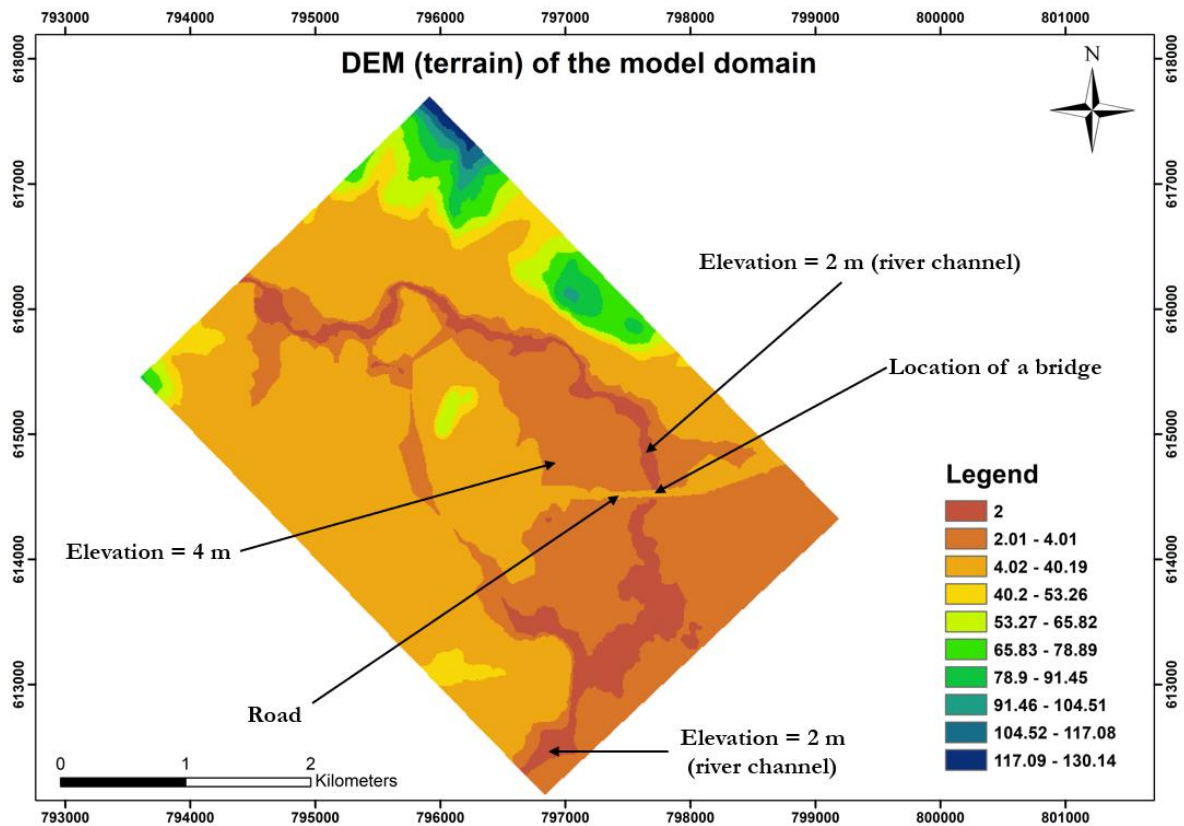


Figure 5-21: DEM used for creating the 2D grid in the 1D2D SOBEK hydrodynamic model

5.2.5. Model results of future tidal projections

Although the 1D2D SOBEK hydrodynamic model could not be calibrated in the study, the set of procedures executed to set up the model and perform test runs created the basis to proceed and perform simulations to assess the effect of sea level rise on flooding in the model domain. Also, the acknowledged uncertainties of the model simulated outputs could not be addressed in the study due to the lack of a detailed DEM that could accurately represent the terrain of the model domain. As a result, the simulations of the two highlighted sea level rise scenarios (i.e., 2060 and 2100) were executed using the inflow discharge data of 2017 and the increased tidal heights of the 2017 tidal data obtained for the study.

The results of the comparison made between the simulated inundation extents of 2017 and the scenario of 2060 are shown in Figure 5-22. The comparison findings based on the different time instances show in the figure revealed that the inundation area increased by 1.39% and 0.58% on 25th June at 18:00:00 and 14th July at 08:00:00, respectively. However, the inundation on 7th July decreased by 0.04%. The inundation area increase recorded in the respective simulated inundation extent maps of the 2060 scenario was at the downstream area of the model domain. The comparison of the average water depths in the various simulated inundation extents also revealed an increase in all the inundation extents produced from the simulations of the 2060 scenario. On the 25th of June, the average water depths increased by 2.26%, and on 7th July, an increase of 0.25% was recorded. The average water depths increased by 2.02% in the simulated inundation extent of 14th July.

Figure 5-23 shows the comparison made between the simulated inundation extents of 2017 and that of the scenario of 2100. The assessment results proved that inundation areas in all the simulated inundation extents of the 2100 scenario increased. The increase in the inundation area on 7th July at 18:00:00 was 0.20%. This was the lowest recorded inundation increase in all simulated inundation extents of the 2100 scenario. The inundation area increases on 25th June at 18:00:00 was 4.01%, while 14th July at 08:00:00 was 1.35%. The findings of the scenario simulations revealed that inundation in the downstream area in all simulated inundation extents increased. Similar to the water depths in the simulated inundation maps of the 2060 scenario, the average water depths increased in all the simulated inundation extents of the scenario of 2100. The average water depth increases of 2.86% and 0.4% were recorded in the simulated inundation extents of 25th June and 7th July, respectively. The highest average water depth increase recorded in all the simulated inundation extents of the 2100 scenario was 3.26% and was recorded on 14th July.

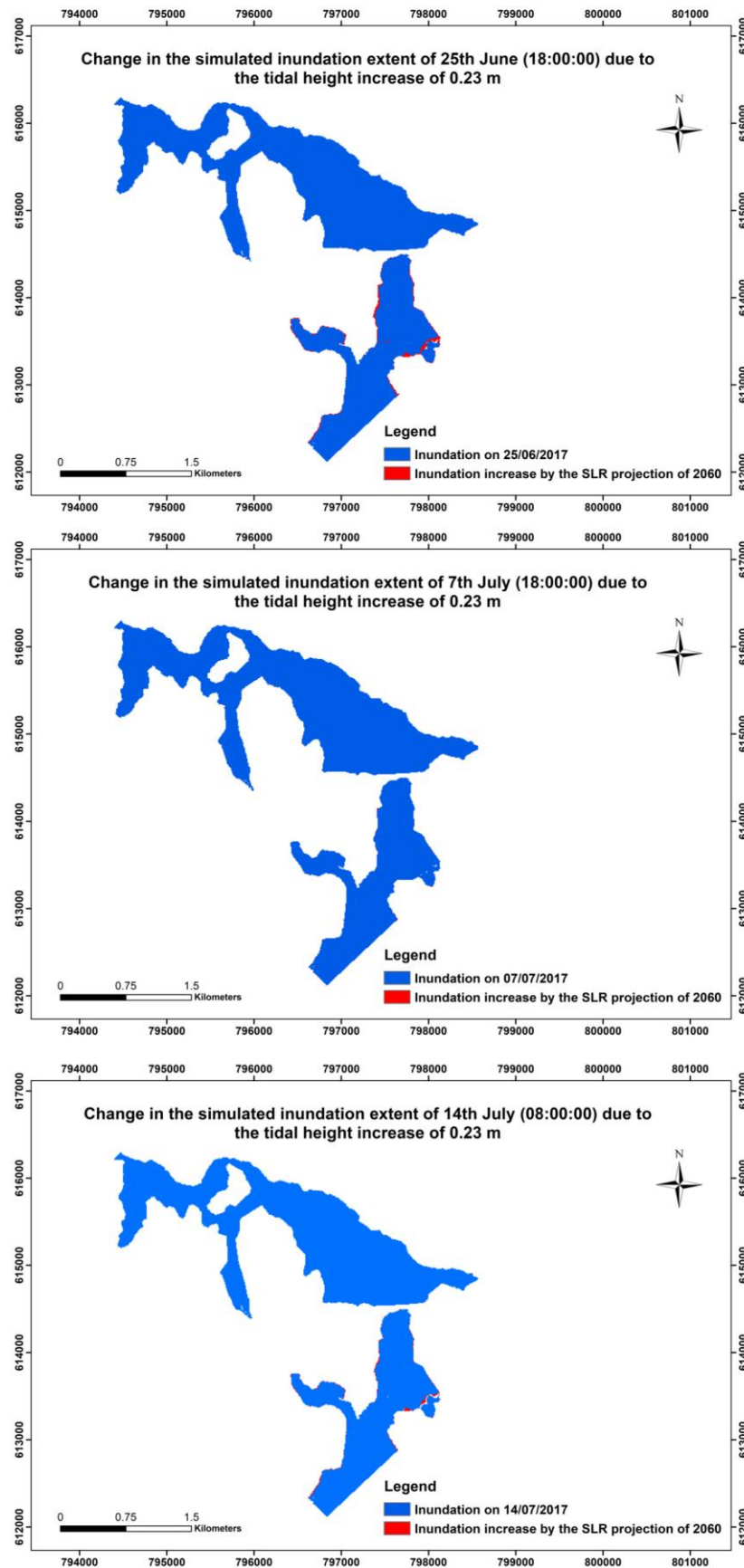


Figure 5-22: Change in simulated inundation extent as a result of the sea level rise (SLR) projection of 2060

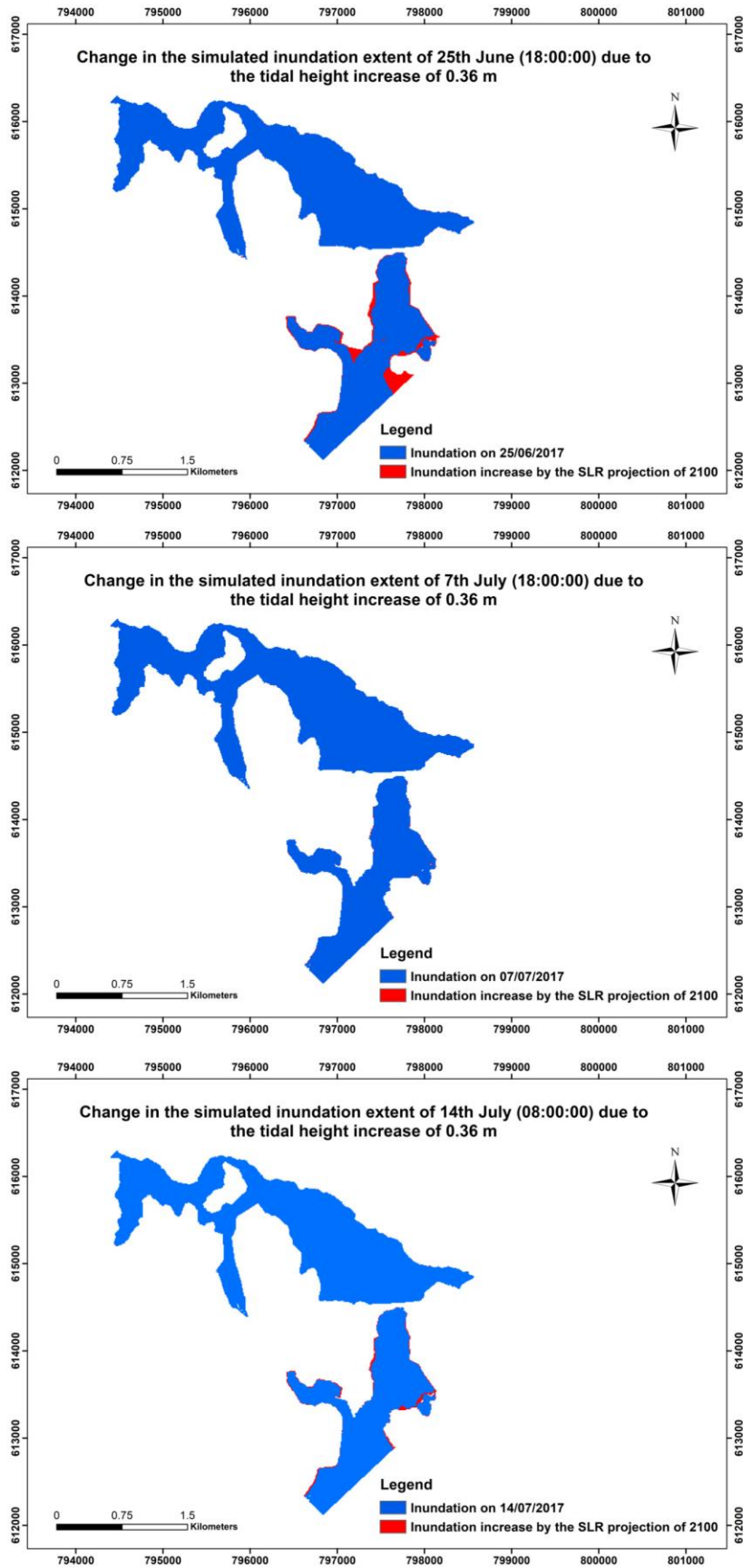


Figure 5-23: Change in simulated inundation extent as a result of the sea level rise (SLR) projection of 2100

6. CONCLUSION AND RECOMMENDATION

6.1. Conclusion

The objective of this research was to assess the effects of sea level rise by climate change on flooding in the coastal urban area downstream of the Densu River basin. A previous study performed by Addae (2018) identified the upstream reservoir spillage and the backwater effect due to seawater intrusion at the downstream area as the cause of the recurrent floods in the area. Since hydrodynamic models are employed to acquire knowledge of floods, the 1D2D SOBEK hydrodynamic model of Addae (2018) was adapted to simulate flow processes in this urban area of the data-scarce Densu River basin with the aim of achieving the study objective. Due to the lack of field observed data, the calibration of the hydrodynamic model was attempted using satellite-based surface water maps produced from Sentinel-1 and PlanetScope satellite images.

Furthermore, since the accuracy of model calibration is dependent on the accuracy of the observation data used, it was imperative to assess the performance of SAR and optical satellite images in mapping surface water. In view of this, the Edge Otsu algorithm was used to map surface water on the satellite images employed for the study. The algorithm was applied using the Google Earth Engine (GEE), the GEE Python API and the HYDRAFloods open-source python package. The HAND algorithm was also used to produce a HAND filter of the model domain to filter misclassified water pixels in the satellite-based surface water maps and detected water pixels that were not as a result of the floods in the satellite images.

As a preliminary analysis step before the actual surface water mapping operations, the findings of the RGB composite images created from the Sentinel-1 flood images proved that flooded regions existed only along the Densu river channel. The backscatter threshold values identified for the Sentinel-1 flood images captured on 25/07/2017 (SF25JUN17) and 07/07/2017 (SF07JUL17) differed slightly. The findings revealed that the satellite-based surface water maps of the model domain produced from the Sentinel-1 flood images were plausible and representative of the surface water in the various images. However, the surface water maps showed dry patches along the course of the river channel as per the visual inspection performed. These dry patches were attributed to the vegetation along the river channel, which may have caused an increase in the backscatter returns captured in the satellite image. Thus, these regions were mapped as dry since regions covered with water in SAR satellite imagery generally have low radar backscatter intensities. The surface water maps of the model domain produced from the wet Sentinel-1 images could not be quantitatively assessed due to the lack of comparable cloud-free optical images. However, the Sentinel-1 imagery of a dry-weather flow condition capture on 24/12/2019 (SD24DEC17) used in mapping surface water in the Densu Delta Wetland was quantitatively assessed. The visual inspection of the surface water map produced from SD24DEC17 proved that the surface water map was plausible apart from a few dry patches observed in the map. Moreover, the overall classification accuracy and Kappa coefficient of the satellite-based surface water map produced from SD24DEC17 were 84.16% and 0.69, respectively.

Surface water bodies on the PlanetScope optical satellite images were detected using NDWI. The examination of the NDWI maps produced from satellite images revealed similarities of NDWI values of surface water regions and built-up areas. Clouds and cloud shadows also depicted similar NDWI values as water. As a result, it was challenging in determining the threshold values to segment water from all the NDWI maps computed fully. Also, the ranges of NDWI values of regions covered with water in all the maps were different. The findings suggested that the spectral reflectance values of surface water in the various optical satellite images employed for the study were different and consequently caused the

difference in the NDWI value ranges for water. Thus, using one threshold value to segment water in all the NDWI maps computed from the PlanetScope flood images would lead to inaccurate data analysis. Due to the NDWI value similarities of surface water and urban structures, the satellite-based surface water maps produced from the PlanetScope flood images exhibited some misclassification of water pixels. The surface water map produced from the PlanetScope flood image captured on 25/06/2107 (PF25JUN17), in particular, showed widespread misclassification of water pixels as compared to the surface water map produced from the PlanetScope flood image captured on 14/07/2017 (PF14JUL17). The surface water map produced from the dry-weather flow Sentinel-1 image captured on 24/12/2017 (PD24DEC17) also showed misclassified water pixels as a result of the built-up areas present in the satellite image. Examination of the pre-processed PF25JUN17 to ascertain the cause of the widespread misclassification revealed that pixels in regions covered with water had higher spectral reflectance values in the near-infrared band than in the green band. The analysis findings suggested possible defects in the satellite image since the spectral reflectance of water in the NIR band ought to be lower than in the green band and not the inverse as in the case of dry areas. With the exception of the surface water map produced from PF25JUN17, the overall visual inspection of the surface water maps produced from PF14JUL17 and PD24DEC17 showed that the maps were representative of the surface water in the satellite image, although there was some misclassification of water pixels. The quantitative accuracy assessment of the surface water map of PF14JUL17 resulted in an overall classification accuracy and Kappa coefficient of 86.14% and 0.69, respectively. The surface water map of the Densu Delta Wetland produced from PD24DEC17 also recorded an overall classification accuracy and Kappa coefficient of 90.10% and 0.80, respectively.

As a means to harness the advantages of SAR and optical satellite images in mapping surface water, the feature-level image fusion method was applied using the random forest classifier. Apart from creating a fused surface water map of the Densu Delta Wetland using a SAR and an optical image (PD24DEC19 and SD24DEC19) captured on the same day, a multi-temporal fused surface water map of the model domain was also produced using SF07JUL17 and PF14JUL17. The findings of the image fusion approach showed an improved overall classification accuracy and Kappa coefficient compared to the surface water maps produced from the individual SAR and optical satellite images. An overall classification accuracy of 97% with a Kappa coefficient of 0.93 was recorded for the surface water map produced from the fusion of SF07JUL17 and PF14JUL17. Furthermore, the overall classification accuracy and Kappa coefficient of the fused surface water map produced from SD24DEC19 and PD24DEC19 was 98% and 0.97, respectively. However, misclassified water pixels were observed in the fused surface water map produced from SF07JUL17 and PF14JUL17. This was attributed to the NDWI map of PF14JUL17 used in the feature-level satellite image fusion exercise. The similarities of the NDWI values of surface water and built-up areas caused the misclassification of the water pixels that was observed in the fused surface water map. The misclassified water pixels found in the surface water map produced from PD24DEC19 was not observed in the fused surface water map of PD24DEC19 and SD24DEC19. Since the built-up area in PD24DEC19 was not as large as in PF14JUL17, the findings suggest that the occurrence of misclassified water pixels in the fused surface water map produced from the SAR and optical satellite images was dependent on the size of the built-up areas in the area of interest. Also, the fused surface water map produced from SF07JUL17 and PF14JUL17 was affected by clouds present in the PlanetScope flood image. This also indicated that the satellite image fusion approach used in this study could not remedy the effects of clouds and implied that using cloud-free optical images would have resulted in a more satisfactory fused satellite-based surface water map as observed in the fused map of PD24DEC19 and SD24DEC19.

The setting up of the 1D2D SOBEK hydrodynamic flood model used in the study was performed by modifying the schematisation of Addae (2018) while maintaining the 1D network, the DEM, the inflow

discharge data, the cross-section data and the surface roughness data from the study. The modification of the schematisation included substituting the 2D boundary nodes at the upstream and downstream edges of the model domain with 1D boundary nodes. Also, to account for the seawater intrusion over multiple 2D grid cells, the schematisation was modified with a 2D line boundary at the downstream end of the model domain, where the backwater effect was recorded in the simulated inundation extents of Addae (2018). Tidal data of Accra with the same temporal characteristics as the inflow discharge data was sourced as the downstream boundary condition. The model tests proved that the model was able to simulate real-world hydrodynamic processes satisfactorily as the constant low inflow discharge over a period of 3 days triggered a smaller inundation than the constant high inflow discharge used. The model tests also proved that the model could handle tidal intrusion propagated to the upstream part of the model domain. Additionally, the findings of the sensitivity analysis performed revealed that the model is sensitive to the number of 2D grid cells used in installing the 2D line boundary line.

The comparisons made between the satellite-based surface water maps and the simulated inundation extents to calibrate the 1D2D hydrodynamic model were executed using the Critical Success Index (CSI) as the performance measure. The findings of the comparisons proved that the fit between the surface water maps from the satellite mapping operations and the model was not satisfactory. Although a better fit was recorded from the multivariate assessment performed, the fit was also not satisfactory. The poor fit of the inundation extents was attributed to uncertainties in the satellite-based maps as well as the simulated inundation extents. The latter was due to the DEM used in setting up the model. The misfit owing to the comparisons performed implied that the calibration of the model with the satellite-based surface water maps could not be achieved as the variation of the surface roughness data could not improve the fit considerably. As a result, the calibration of the 1D2D hydrodynamic model employed for the study was not successful.

The effects of sea level rise on flooding in the model domain were assessed using two scenarios of tidal height increases based on the sea level rise projections for 2060 and 2100 obtained from literature. The assessments of the simulated inundation extents from the two scenarios were based on the change in inundation area and average water depth. The comparisons performed between the simulated inundation extents of specific instances of the flood event of 2017 and the scenario of 2060 showed an overall increase in inundation in the downstream area of the model domain. However, the inundation increases were not significant as the highest inundation increase among the comparisons performed was 1.39%. The highest increase in the average water depths of the comparisons made also was 2.26%. Similarly, the inundation areas as well as the average water depths in the simulated inundation extents produced from the scenario of 2100 increased. The highest recorded increase in inundation area was 4.01%, while the highest recorded average water depth increase was 3.26%.

The study highlighted the potential and complexities of using SAR and optical satellite images in mapping surface water within an urban area. The study also presented information on fusing these satellite data types to improve satellite-based surface water maps. The hydrodynamic modelling performed by adapting the model of Addae (2018) demonstrates the feasibility of assessing flow processes that account for tidal behaviour within the model domain. The assessment of the sea level rise scenarios constructed in the study indicates increases in inundation area and average water depth and suggests the likelihood of severe inundation in the downstream area of the model domain as a result of sea level rise. These add up to the existing knowledge of the study area and imply the need for more research to improve the understanding of the hydrodynamic processes as well as how remote sensing can be effectively used to improve the output of flood models.

6.2. Recommendation

A major limitation of this study was the lack of detailed representation of the model domain's terrain, which could have improved the simulated inundation extents produced. The DEM used for the model setup exhibited terrain characteristics that resulted in uncertainties in the model simulated outputs. Also, the lack of multiple satellite images which could have been used to map surface water for different instances of the event simulated limited the study. The satellite data types used in the study influenced the choice of surface water mapping techniques used and the results obtained. For example, the PlanetScope images lacked bands that could have been used to compute other water indices that have shown better performances in mapping surface water within urban areas. The recommendations below were formulated for future studies.

- Detailed hydrometric data on a recent flood event should be collected to construct a new hydrodynamic model since no other available satellite image was found to have captured the event modelled in this study. The calibration of the hydrodynamic model of the study area could then be assessed with different datasets.
- Multiple satellite images should be obtained to improve the satellite-based surface water maps of the area. The area of interest in the optical satellite images should be cloud-free, and the collection of SAR images obtained for the study should contain images of finer resolution than that of Sentinel-1 images.
- The model domain should be extended to the coast where the seawater enters the Densu Delta Wetland in order to accurately account for the effects of tides in the study area.
- A DEM with a detailed representation of the study area's terrain and vertical structures should be employed to set up the hydrodynamic model to analyse the hydrodynamic flow processes. This DEM should cover the inaccessible regions of the study area as well.
- Tidal data from the requisite local institution should be acquired to ensure coherence in the datums of the DEM (2D grid) that will be used in setting up the hydrodynamic model and the tidal heights.

LIST OF REFERENCES

- Addae, R. A. (2018). *Satellite-Based Flood Mapping for Hydrodynamic Flood Model Assessment: Accra, Ghana (Masters' thesis)*. Retrieved from https://library.itc.utwente.nl/papers_2018/msc/wrem/AmoahAddae.pdf
- Ardeshir Goshtasby, A., & Nikolov, S. (2007). Image fusion: Advances in the state of the art. *Information Fusion*, 8(2), 114–118. <https://doi.org/10.1016/j.inffus.2006.04.001>
- Ashok, H. G., & Patil, D. R. (2014). Survey on Change Detection in SAR Images. *International Journal of Computer Applications. National Conference on Emerging Trends in Computer Technology (NCETCT-2014)*, 975–8887. Retrieved from <https://citeseerx.ist.psu.edu/viewdoc/download?doi=10.1.1.735.3333&rep=rep1&type=pdf>
- Ashtekar, A. S., Mohammed-Aslam, M. A., & Moosvi, A. R. (2019). Utility of Normalized Difference Water Index and GIS for Mapping Surface Water Dynamics in Sub-Upper Krishna Basin. *Journal of the Indian Society of Remote Sensing*, 47(8), 1431–1442. <https://doi.org/10.1007/s12524-019-01013-6>
- Asumadu-Sarkodie, S., Owusu, P. A., & Jayaweera, H. M. (2015). Flood risk management in Ghana: A case study in Accra. *Advances in Applied Science Research*, 6(4), 196–201. <https://doi.org/10.6084/M9.FIGSHARE.3381484.V1>
- Asumadu-Sarkodie, S., Owusu Phebe, A., & Rufangura, P. (2015). Impact analysis of flood in Accra, Ghana. *Advances in Applied Science Research*, 6(9), 53–78. Retrieved from <https://open.metu.edu.tr/handle/11511/68807>
- Bhaga, T. D., Dube, T., & Shoko, C. (2020). Satellite monitoring of surface water variability in the drought prone Western Cape, South Africa. *Physics and Chemistry of the Earth*, 102914. <https://doi.org/10.1016/j.pce.2020.102914>
- Bioresita, F., Puissant, A., Stumpf, A., & Malet, J. P. (2019). Fusion of Sentinel-1 and Sentinel-2 image time series for permanent and temporary surface water mapping. *International Journal of Remote Sensing*, 40(23), 9026–9049. <https://doi.org/10.1080/01431161.2019.1624869>
- Breiman, L. (2001). Random forests. *Machine Learning*, 45(1), 5–32. <https://doi.org/10.1023/A:1010933404324>
- Canny, J. (1986). A Computational Approach to Edge Detection. *IEEE Transactions on Pattern Analysis and Machine Intelligence*, PAMI-8(6), 679–698. <https://doi.org/10.1109/TPAMI.1986.4767851>
- Chouari, W. (2021). Wetland land cover change detection using multitemporal Landsat data: a case study of the Al-Asfar wetland, Kingdom of Saudi Arabia. *Arabian Journal of Geosciences*, 14(6), 523. <https://doi.org/10.1007/s12517-021-06815-y>
- CIA Factbook. (2021). Ghana - The World Factbook. Retrieved May 22, 2021, from <https://www.cia.gov/the-world-factbook/countries/ghana/>
- Cohen, J. (1960). A Coefficient of Agreement for Nominal Scales. *Educational and Psychological Measurement*, 20(1), 37–46. <https://doi.org/10.1177/001316446002000104>
- Congalton, R. G. (2001). Accuracy assessment and validation of remotely sensed and other spatial information. *International Journal of Wildland Fire*, 10(4), 321. <https://doi.org/10.1071/WF01031>
- Copernicus: Sentinel-2 - Satellite Missions - eoPortal Directory. (n.d.). Retrieved April 15, 2021, from <https://directory.eoportal.org/web/eoportal/satellite-missions/c-missions/copernicus-sentinel-2>
- Crist, E. P. (1985). A TM Tasseled Cap equivalent transformation for reflectance factor data. *Remote Sensing of Environment*, 17(3), 301–306. [https://doi.org/10.1016/0034-4257\(85\)90102-6](https://doi.org/10.1016/0034-4257(85)90102-6)
- Crist, E. P., & Cicone, R. C. (1984). A Physically-Based Transformation of Thematic Mapper Data—The TM Tasseled Cap. *IEEE Transactions on Geoscience and Remote Sensing*, GE-22(3), 256–263. <https://doi.org/10.1109/TGRS.1984.350619>
- Deltares. (2018). *SOBEK, Hydrodynamics, Rainfall Runoff and Real Time Control*. Retrieved from <https://download.deltares.nl/en/download/sobek/>
- Douglas, I., Alam, K., Maghenda, M., McDonnell, Y., Mclean, L., & Campbell, J. (2008). Unjust waters: climate change, flooding and the urban poor in Africa. *Environment and Urbanization*, 20(1), 187–205. <https://doi.org/10.1177/0956247808089156>
- Ekeu-wei, I. T., & Blackburn, G. A. (2018). Applications of Open-Access Remotely Sensed Data for Flood Modelling and Mapping in Developing Regions. *Hydrology*, 5(3), 39. <https://doi.org/10.3390/hydrology5030039>
- Foreman, M. G. G. (1977). *Manual for Tidal Heights Analysis and Prediction*. Retrieved from

https://www.researchgate.net/publication/264782849_Manual_for_Tidal_Currents_Analysis_and_Prediction

- Giustarini, L., Hostache, R., Matgen, P., Schumann, G. J. P., Bates, P. D., & Mason, D. C. (2013). A Change Detection Approach to Flood Mapping in Urban Areas Using TerraSAR-X. *IEEE Transactions on Geoscience and Remote Sensing*, 51(4), 2417–2430. <https://doi.org/10.1109/TGRS.2012.2210901>
- Grimaldi, S., Li, Y., Pauwels, V. R. N., & Walker, J. P. (2016). Remote Sensing-Derived Water Extent and Level to Constrain Hydraulic Flood Forecasting Models: Opportunities and Challenges. *Surveys in Geophysics*, 37(5), 977–1034. <https://doi.org/10.1007/s10712-016-9378-y>
- GSS. (2013). 2010 Population & Housing Census National Analytical Report. In *Ghana Statistical Service*. Retrieved from http://www.statsghana.gov.gh/gssmain/fileUpload/pressrelease/2010_PHC_National_Analytical_Report.pdf
http://statsghana.gov.gh/docfiles/2010phc/National_Analytical_Report.pdf
- Herndon, K., Muench, R., Cherrington, E., & Griffin, R. (2020). An assessment of surface water detection methods for water resource management in the Nigerien Sahel. *Sensors (Switzerland)*, 20(2), 431. <https://doi.org/10.3390/s20020431>
- Hu, A., & Demir, I. (2021). Real-Time Flood Mapping on Client-Side Web Systems Using HAND Model. *Hydrology*, 8(2), 65. <https://doi.org/10.3390/hydrology8020065>
- Huang, C., Nguyen, B. D., Zhang, S., Cao, S., & Wagner, W. (2017). A comparison of terrain indices toward their ability in assisting surface water mapping from sentinel-1 data. *ISPRS International Journal of Geo-Information*, 6(5), 140. <https://doi.org/10.3390/ijgi6050140>
- Irwin, K., Beaulne, D., Braun, A., & Fotopoulos, G. (2017). Fusion of SAR, Optical Imagery and Airborne LiDAR for Surface Water Detection. *Remote Sensing*, 9(9), 890. <https://doi.org/10.3390/rs9090890>
- ITC. (2013). *The core of GIScience: a system based approach*. Retrieved from <https://www.itc.nl/library/education/core-of-giscience/>
- Jiang, W., Ni, Y., Pang, Z., He, G., Fu, J., Lu, J., ... Lei, T. (2020). A new index for identifying water body from sentinel-2 satellite remote sensing imagery. *ISPRS Annals of the Photogrammetry, Remote Sensing and Spatial Information Sciences*, 5(3), 33–38. <https://doi.org/10.5194/isprs-Annals-V-3-2020-33-2020>
- Karim, F., Petheram, C., Marvanek, S., Ticehurst, C., Wallace, J., & Gouweleeuw, B. (2011). The use of hydrodynamic modelling and remote sensing to estimate floodplain inundation and flood discharge in a large tropical catchment. *19th International Congress on Modelling and Simulation, Perth, Australia, 12–16 December 2011*, (2011, December), 3796–3802. Retrieved from <https://mssanz.org.au/modsim2011/18/karim.pdf>
- Karley, N. K. (2009). Flooding and Physical Planning in Urban Areas in West Africa: Situational Analysis of Accra, Ghana. *Theoretical and Empirical Researches in Urban Management*, 4(13), 25–41. Retrieved from <https://core.ac.uk/reader/6257932>
- Klemas, V. (2015). Remote Sensing of Floods and Flood-Prone Areas: An Overview. *Journal of Coastal Research*, 314(4), 1005–1013. <https://doi.org/10.2112/JCOASTRES-D-14-00160.1>
- Landis, J. R., & Koch, G. G. (1977). The Measurement of Observer Agreement for Categorical Data. *Biometrics*, 33(1), 159. <https://doi.org/10.2307/2529310>
- Liu, Z., Blasch, E., Bhatnagar, G., John, V., Wu, W., & Blum, R. S. (2018). Fusing synergistic information from multi-sensor images: An overview from implementation to performance assessment. *Information Fusion*, 42, 127–145. <https://doi.org/10.1016/j.inffus.2017.10.010>
- Mahyoub, S., Fadil, A., Mansour, E. M., Rhinane, H., & Al-Nahmi, F. (2019). Fusing of optical and synthetic aperture radar (SAR) remote sensing data: A systematic literature review (SLR). *International Archives of the Photogrammetry, Remote Sensing and Spatial Information Sciences - ISPRS Archives*, 42(4/W12), 127–138. <https://doi.org/10.5194/isprs-archives-XLII-4-W12-127-2019>
- Markert, K. N., Markert, A. M., Mayer, T., Nauman, C., Haag, A., Poortinga, A., ... Saah, D. (2020). Comparing Sentinel-1 Surface Water Mapping Algorithms and Radiometric Terrain Correction Processing in Southeast Asia Utilizing Google Earth Engine. *Remote Sensing*, 12(15), 2469. <https://doi.org/10.3390/rs12152469>
- Martinis, S., Clandillon, S., Plank, S., Twele, A., Huber, C., Caspard, M., ... Fuchs, E.-M. (2017). *ASAPTERRA Final Report*. Retrieved from http://elib.dlr.de/110776/1/ASAPTERRA_FinalReport_2017.pdf
- Mason, D. C., Giustarini, L., Garcia-Pintado, J., & Cloke, H. L. (2014). Detection of flooded urban areas in high resolution Synthetic Aperture Radar images using double scattering. *International Journal of Applied Earth Observation and Geoinformation*, 28(1), 150–159.

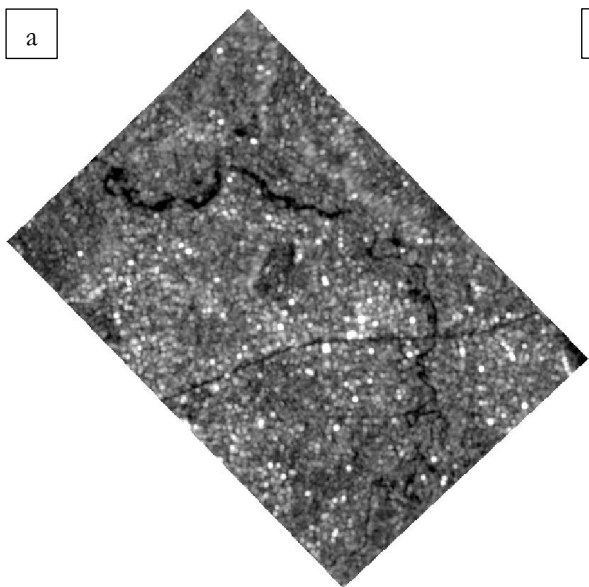
- <https://doi.org/10.1016/j.jag.2013.12.002>
- McFeeters, S. K. (1996). The use of the Normalized Difference Water Index (NDWI) in the delineation of open water features. *International Journal of Remote Sensing*, 17(7), 1425–1432. <https://doi.org/10.1080/01431169608948714>
- McHugh, M. L. (2012). Interrater reliability: the kappa statistic. *Biochemia Medica*, 22(3), 276–282. <https://doi.org/10.11613/BM.2012.031>
- Medeiros, S. C., Hagen, S. C., & Weishampel, J. F. (2012). Comparison of floodplain surface roughness parameters derived from land cover data and field measurements. *Journal of Hydrology*, 452–453, 139–149. <https://doi.org/10.1016/j.jhydrol.2012.05.043>
- Ministry of Foreign Affairs of the Netherlands. (2018). *Climate Change Profile: Ghana*. Retrieved from <https://www.government.nl/binaries/government/documents/publications/2019/02/05/climate-change-profiles/Ghana.pdf>
- Mishra, V. K., & Pant, T. (2020). Open surface water index: a novel approach for surface water mapping and extraction using multispectral and multisensory data. *Remote Sensing Letters*, 11(11), 973–982. <https://doi.org/10.1080/2150704X.2020.1804085>
- Notti, D., Giordan, D., Caló, F., Pepe, A., Zucca, F., & Galve, J. (2018). Potential and Limitations of Open Satellite Data for Flood Mapping. *Remote Sensing*, 10(11), 1673. <https://doi.org/10.3390/rs10111673>
- O’Callaghan, J. F., & Mark, D. M. (1984). The extraction of drainage networks from digital elevation data. *Computer Vision, Graphics, & Image Processing*, 28(3), 323–344. [https://doi.org/10.1016/S0734-189X\(84\)80011-0](https://doi.org/10.1016/S0734-189X(84)80011-0)
- Ogilvie, A., Poussin, J. C., Bader, J. C., Bayo, F., Bodian, A., Dacosta, H., ... Sambou, S. (2020). Combining multi-sensor satellite imagery to improve long-term monitoring of temporary surface water bodies in the senegal river floodplain. *Remote Sensing*, 12(19), 1–30. <https://doi.org/10.3390/rs12193157>
- Okyere, C. Y., Yacouba, Y., & Gilgenbach, D. (2013). The problem of annual occurrences of floods in Accra: An integration of hydrological, economic and political perspectives. *Theoretical and Empirical Researches in Urban Management*, 8(2), 45–79. Retrieved from <http://www.jstor.org/stable/24873349>
- Otsu, N. (1979). THRESHOLD SELECTION METHOD FROM GRAY-LEVEL HISTOGRAMS. *IEEE Trans Syst Man Cybern, SMC-9*(1), 62–66. <https://doi.org/10.1109/tsmc.1979.4310076>
- Owusu-Ansah, J. K., Dery, J. M., & Amoako, C. (2019). Flood vulnerability and coping mechanisms around the Weija Dam near Accra, Ghana. *GeoJournal*, 84(6), 1597–1615. <https://doi.org/10.1007/s10708-018-9939-3>
- Pan, F., Xi, X., & Wang, C. (2020). A Comparative Study of Water Indices and Image Classification Algorithms for Mapping Inland Surface Water Bodies Using Landsat Imagery. *Remote Sensing*, 12(10), 1611. <https://doi.org/10.3390/rs12101611>
- Pasquier, U., He, Y., Hooton, S., Goulden, M., & Hiscock, K. M. (2019). An integrated 1D–2D hydraulic modelling approach to assess the sensitivity of a coastal region to compound flooding hazard under climate change. *Natural Hazards*, 98(3), 915–937. <https://doi.org/10.1007/s11069-018-3462-1>
- Planet Labs. (2020). Planet Surface Reflectance. In *Planet Labs Inc*. Retrieved from https://assets.planet.com/marketing/PDF/Planet_Surface_Reflectance_Technical_White_Paper.pdf
- Planet Labs. (2021). Planet Imagery Product Specification. In *Planet Labs Inc*. Retrieved from https://assets.planet.com/docs/Planet_Combined_Imagery_Product_Specs_letter_screen.pdf
- Psomiadis, E., Diakakis, M., & Soulis, K. X. (2020). Combining SAR and Optical Earth Observation with Hydraulic Simulation for Flood Mapping and Impact Assessment. *Remote Sensing*, 12(23), 3980. <https://doi.org/10.3390/rs12233980>
- Pulvirenti, L., Chini, M., Pierdicca, N., & Boni, G. (2016). Use of SAR Data for Detecting Floodwater in Urban and Agricultural Areas: The Role of the Interferometric Coherence. *IEEE Transactions on Geoscience and Remote Sensing*, 54(3), 1532–1544. <https://doi.org/10.1109/TGRS.2015.2482001>
- Quang, N. H., Tuan, V. A., Hao, N. T. P., Hang, L. T. T., Hung, N. M., Anh, V. Le, ... Carrie, R. (2019). Synthetic aperture radar and optical remote sensing image fusion for flood monitoring in the Vietnam lower Mekong basin: a prototype application for the Vietnam Open Data Cube. *European Journal of Remote Sensing*, 52(1), 599–612. <https://doi.org/10.1080/22797254.2019.1698319>
- Refice, A., D’Addabbo, A., & Capolongo, D. (2018). *Flood Monitoring through Remote Sensing*. <https://doi.org/10.1007/978-3-319-63959-8>
- Rennó, C. D., Nobre, A. D., Cuartas, L. A., Soares, J. V., Hodnett, M. G., Tomasella, J., & Waterloo, M. J.

- (2008). HAND, a new terrain descriptor using SRTM-DEM: Mapping terra-firme rainforest environments in Amazonia. *Remote Sensing of Environment*, 112(9), 3469–3481. <https://doi.org/10.1016/j.rse.2008.03.018>
- Rientjes, T. H. M. (2016). Hydrologic modelling for Integrated Water Resource Assessments. In *Lecture book for Modules 9-10 Surface water stream*.
- Roggen, D., Tröster, G., & Bulling, A. (2013). Signal processing technologies for activity-aware smart textiles. In *Multidisciplinary Know-How for Smart-Textiles Developers* (pp. 329–365). <https://doi.org/10.1533/9780857093530.2.329>
- Sagoe-Addy, K., & Appeaning Addo, K. (2013). Effect of predicted sea level rise on tourism facilities along Ghana's Accra coast. *Journal of Coastal Conservation*, 17(1), 155–166. <https://doi.org/10.1007/s11852-012-0227-y>
- Shen, X., Wang, D., Mao, K., Anagnostou, E., & Hong, Y. (2019). Inundation Extent Mapping by Synthetic Aperture Radar: A Review. *Remote Sensing*, 11(7), 879. <https://doi.org/10.3390/rs11070879>
- Sipelgas, L., Aavaste, A., Uiboupin, R., & Rikka, S. (2020). Methodology for Mapping Flood Extent on Estonian Floodplains. *IGARSS 2020 - 2020 IEEE International Geoscience and Remote Sensing Symposium*, 4750–4753. <https://doi.org/10.1109/IGARSS39084.2020.9324369>
- Speckle Filtering Pada Synthetic Aperture Radar - Bagas Setyadi. (n.d.). Retrieved April 15, 2021, from <https://bagasetyadi.com/speckle-filtering-pada-synthetic-aperture-radar/>
- Tavus, B., Kocaman, S., Nefeslioglu, H. A., & Gokceoglu, C. (2020). A FUSION APPROACH FOR FLOOD MAPPING USING SENTINEL-1 AND SENTINEL-2 DATASETS. *ISPRS - International Archives of the Photogrammetry, Remote Sensing and Spatial Information Sciences*, XLIII-B3-2(B3), 641–648. <https://doi.org/10.5194/isprs-archives-XLIII-B3-2020-641-2020>
- Tengan, C., & Aigbavboa, C. O. (2016). Addressing Flood Challenges in Ghana: a Case of the Accra Metropolis. *International Conference on Infrastructure Development in Africa*, (June 2015), 498–504. Retrieved from https://www.researchgate.net/publication/316093848_ADDRESSING_FLOOD_CHALLENGES_IN_GHANA_A_CASE_OF_THE_ACCRA_METROPOLIS
- Tides4fishing. (2021). Tide prediction. Retrieved July 23, 2021, from <https://tides4fishing.com/tides/how-tides-are-forecast>
- Twele, A., Cao, W., Plank, S., & Martinis, S. (2016). Sentinel-1-based flood mapping: a fully automated processing chain. *International Journal of Remote Sensing*, 37(13), 2990–3004. <https://doi.org/10.1080/01431161.2016.1192304>
- Vaiyammal, K., & Raja, R. A. A. (2017). *Change Detection on SAR Images*. 5(17), 1–5. Retrieved from www.ijert.org
- van Leeuwen, B., Tobak, Z., & Kovács, F. (2020). Sentinel-1 and -2 Based near Real Time Inland Excess Water Mapping for Optimized Water Management. *Sustainability*, 12(7), 2854. <https://doi.org/10.3390/su12072854>
- Vanama, V. S. K., Rao, Y. S., & Bhatt, C. M. (2021). Change detection based flood mapping using multi-temporal Earth Observation satellite images: 2018 flood event of Kerala, India. *European Journal of Remote Sensing*, 54(1), 42–58. <https://doi.org/10.1080/22797254.2020.1867901>
- Wang, Y. (2015). Advances in Remote Sensing of Flooding. *Water*, 7(11), 6404–6410. <https://doi.org/10.3390/w7116404>
- WRC. (2007). *WATER RESOURCES COMMISSION, GHANA DENSU RIVER BASIN - Integrated Water Resources Management Plan*. Retrieved from <http://www.wrc-gh.org/dmsdocument/16>
- Xing, L., Tang, X., Wang, H., Fan, W., & Wang, G. (2018). Monitoring monthly surface water dynamics of Dongting Lake using Sentinel-1 data at 10 m. *PeerJ*, 6(6), e4992. <https://doi.org/10.7717/peerj.4992>
- Xu, H. (2006). Modification of normalised difference water index (NDWI) to enhance open water features in remotely sensed imagery. *International Journal of Remote Sensing*, 27(14), 3025–3033. <https://doi.org/10.1080/01431160600589179>
- Xu, Z., Chen, J., Xia, J., Du, P., Zheng, H., & Gan, L. (2018). Multisource Earth Observation Data for Land-Cover Classification Using Random Forest. *IEEE Geoscience and Remote Sensing Letters*, 15(5), 789–793. <https://doi.org/10.1109/LGRS.2018.2806223>
- Zhang, H., & Xu, R. (2018). Exploring the optimal integration levels between SAR and optical data for better urban land cover mapping in the Pearl River Delta. *International Journal of Applied Earth Observation and Geoinformation*, 64, 87–95. <https://doi.org/10.1016/j.jag.2017.08.013>
- Zhou, Q., & Liu, X. (2002). Error assessment of grid-based flow routing algorithms used in hydrological models. *International Journal of Geographical Information Science*, 16(8), 819–842.

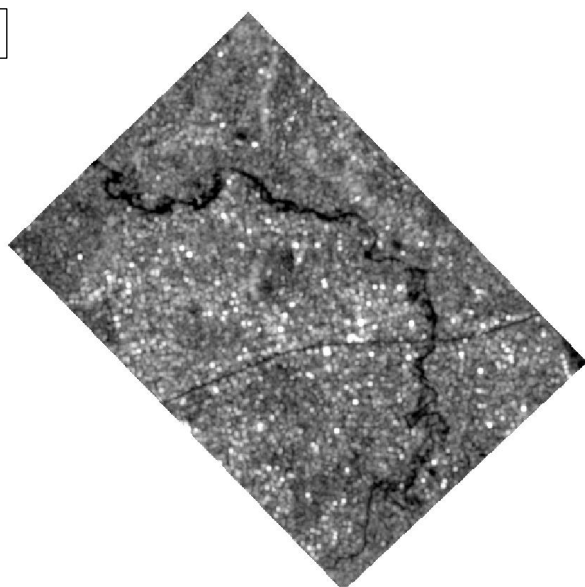
<https://doi.org/10.1080/13658810210149425>

APPENDIX A

a

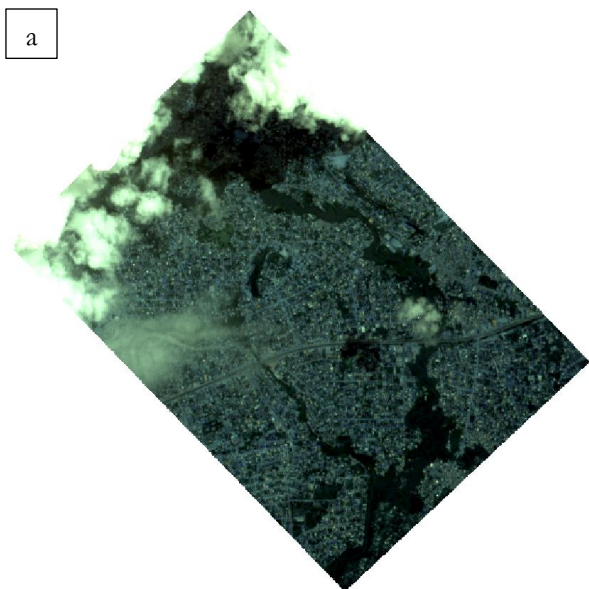


b

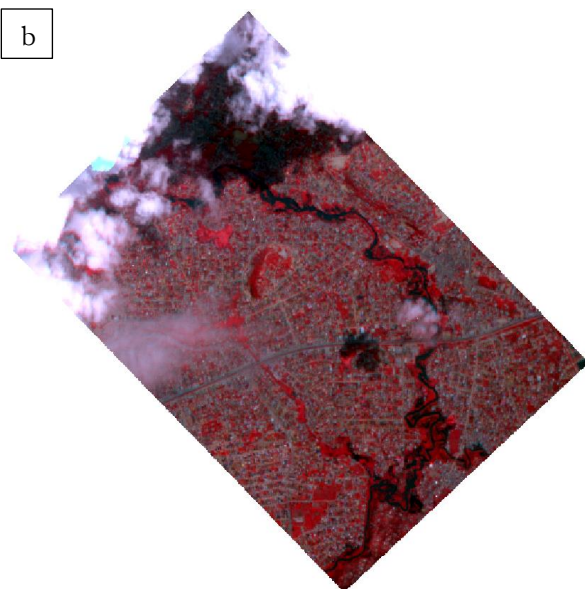


Sentinel-1 images a) image captured on 25/06/2017 b) image captured on 07/07/2017

a



b

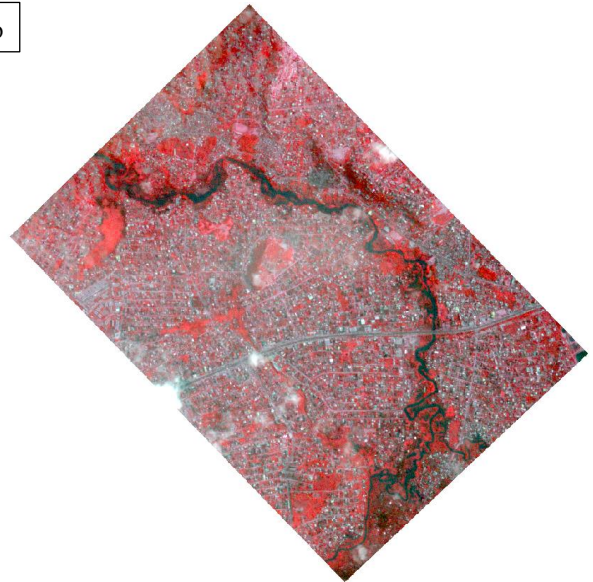


PlanetScope satellite image captured on 25/06/2017 a) true colour composite b) false colour composite

a

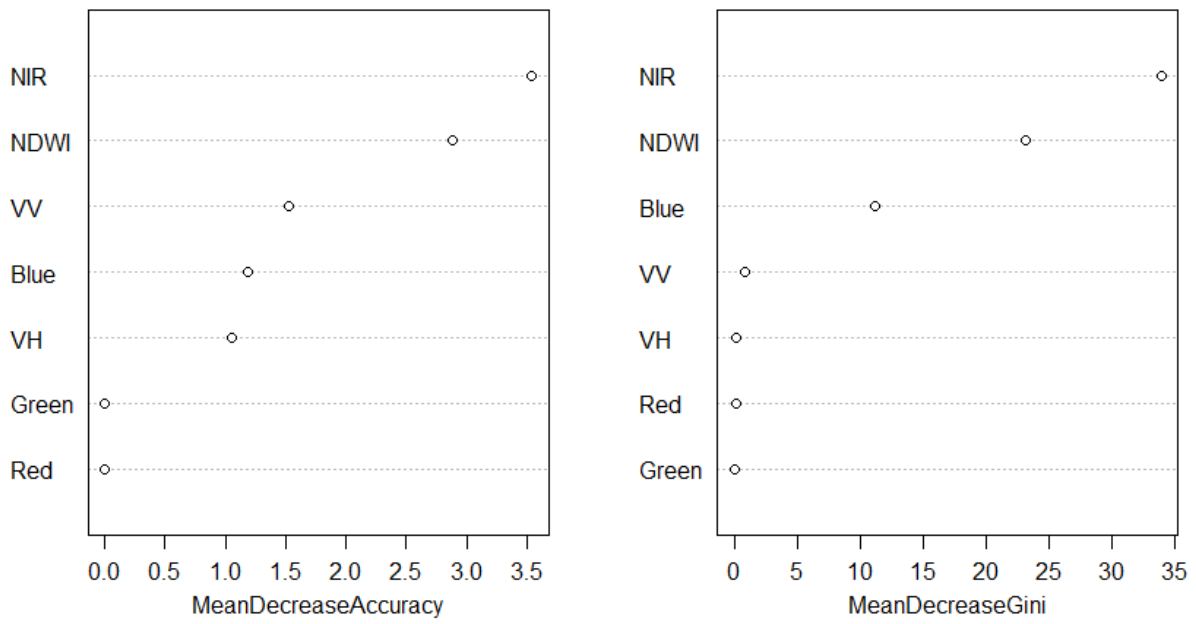


b

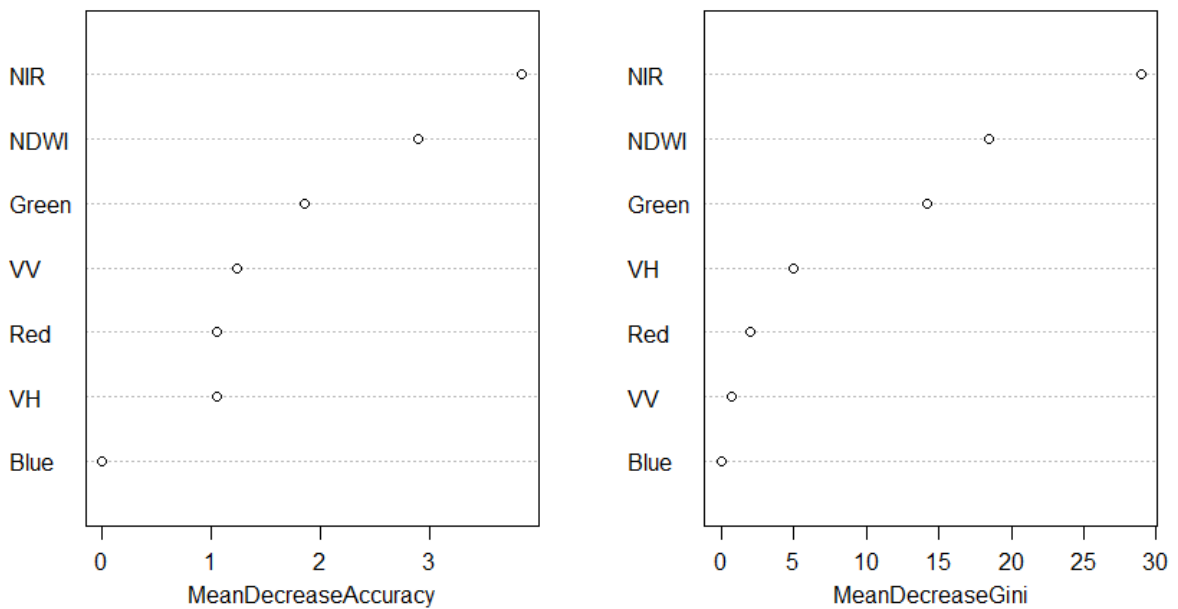


PlanetScope satellite image captured on 14/07/2017 a) true colour composite b) false colour composite

APPENDIX B



Variable importance of the classification of the fused image created from SF07JUL17 and PF14JUL17



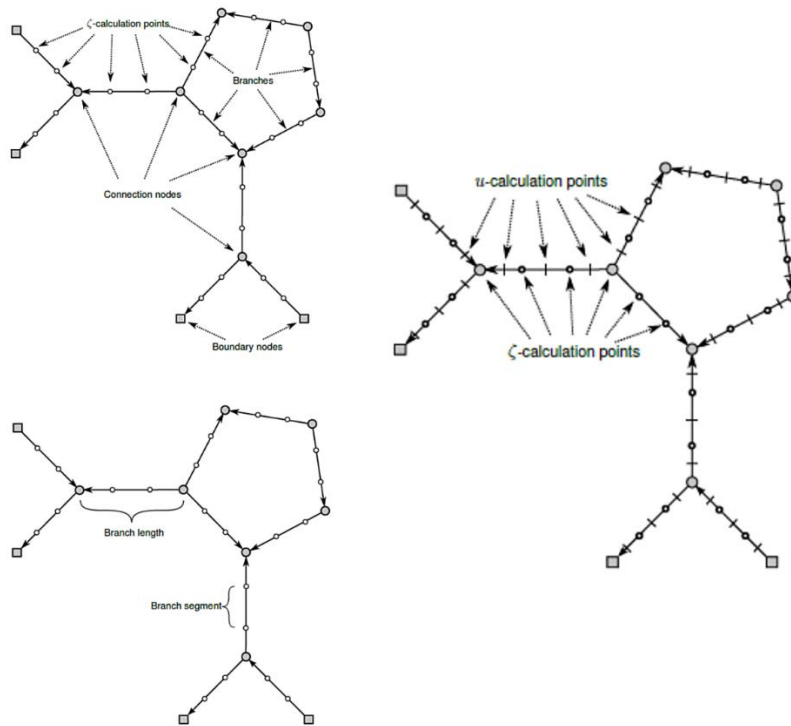
Variable importance of the classification of the fused image created from SD24DEC19 and PD24DEC19

APPENDIX C

1D2D SOBEK Hydrodynamic Model

The information on the SOBEK model and the 1D flow and 2D flow equations below was modified from the Deltares website SOBEK 2.16.004 user manual (<https://download.deltares.nl/en/download/sobek>). The 1D2D SOBEK hydrodynamic model is a robust modelling software package centered on a high-performance computing technology that can be used to simulate flow processes in almost any system. Apart from the fact that this integrated hydrodynamic model is easy to learn, the programme's ability to guide a user in achieving accurate model description by optimising resources makes configuration straightforward. Its graphical user interface is also easy to operate. The SOBEK Modules can handle intricate and simple flows due to accurate representation of events and physical processes in 1D network structures and 2D horizontal grids. The programme offers a single environment to simulate various water-related problems and is ideal for studies such as river floods and urban flooding. The design of the programme enables the integration of other standard data formats and GIS environments. Computer crashes are prevented despite the complexity of any simulation due to the 1D2D SOBEK hydrodynamic model's powerful numerical core. Even with transitions through abruptly changing cross-section shapes, the model ensures mass conservation. However, a computer's internal memory is the only constraint to the size of the programme.

The 1D2D SOBEK hydrodynamic model's 1D flow module is responsible for flow in channels, whereas the 2D module simulates flow processes on floodplains. The 1D flow module is made up of a network of branches linked together at connection nodes. Several ζ -calculation points can be established on each branch of a network. These calculation points, which may not be equidistant, serve as the spatial numerical framework applied in simulations. When computation points are defined, branches are separated into branch segments which together with ζ -calculation points form a staggered grid. Discharges are computed at the branch segments. Water levels and velocities are, however, computed at different locations on a staggered grid. The computation of water levels is made at ζ -calculation points, connection nodes and boundary nodes, while water velocities are computed at u-calculation points. An accurate representation of flow processes is achieved when the distances successive ζ -calculation points are short. However, when the distances are too short, the model's simulation time increases. Therefore, by default, SOBEK applies a minimum of 1 m during simulations. The solution of the continuity equation is performed between the u-calculation points, whereas the momentum equation is performed between ζ -calculation points.



SOBEK flow model staggered grids (source: (Deltares, 2018))

1D-2D Connection

In a 1D2D SOBEK hydrodynamic model, a 1D network is connected to a 2D grid through either the 1D ζ -calculation points or the 1D connection nodes and the 2D grid cells. Only a single connection per 2D grid cell is permitted. Based on the map coordinates of a 2D grid cell's centre and its corresponding 1D connection node or ζ -calculation point, the locations where connections are established are determined by the computational code. The criteria for making or not making a connection is expressed in the equation indicated below.

$$\text{if } |X1 - X2| \leq \Delta x/2 \text{ and } |Y1 - Y2| \leq \Delta y/2 \quad \text{Equation 1}$$

Where:

X1 and Y1	x and y map coordinates for the 1D node
X2 and Y2	x and y map coordinates for the 2D grid cell
Δx	Width of the grid cell in the x-direction
Δy	Width of the grid cell in the y-direction (Δx is equal to Δy)

With no alterations made to the length of the connecting 1D branch, the centre of the 1D connection node is internally relocated to fit the centre of the 2D grid cell once the criteria in the equation above is fulfilled. Consequently, the 2D grid cell is regarded as a component of the 1D connection or calculation point, and as such, flow is processed as 1D when channel flow is below the 2D grid and processed as 2D flow when the flow is above the 2D grid. The figure below shows the 1D-2D connections.

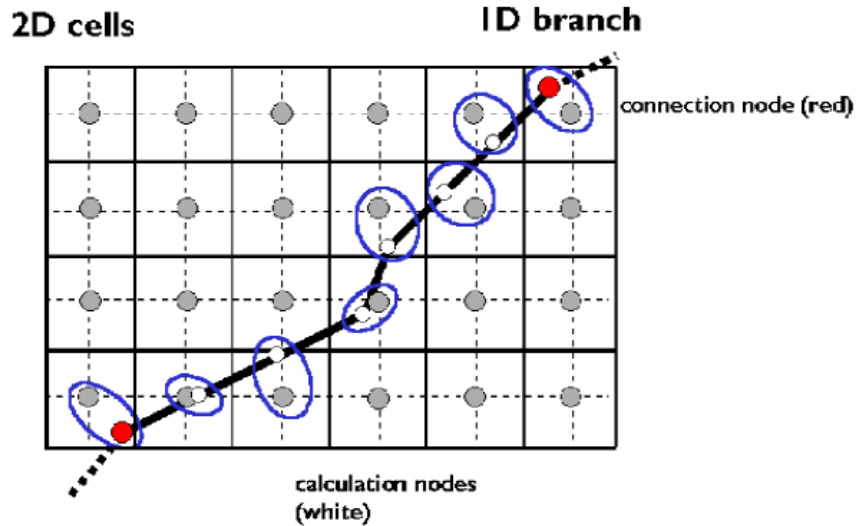


Illustration of the 1D network and 2D grid connections (source: (Deltares, 2018))

Model Equations

The 1D2D SOBEK hydrodynamic simulation engine is fitted with a highly reliable numerical computing scheme and performs combined simulations via an implicit coupling of 1D and 2D flow equations. The model applies both the continuity equation and the momentum equations to conserve mass and momentum, respectively.

1D Flow Equations

In order to calculate 1D flow, the SOBEK model solves the complete De Saint Venant equations. The process involves the solution of the 1D continuity equation and the 1D momentum equations. The two equations are expressed below:

Continuity equation (1D):

$$\frac{\partial A_T}{\partial t} + \frac{\partial Q}{\partial x} = q_{lat} \quad \text{Equation 2}$$

Momentum equation (1D):

$$\frac{\partial Q}{\partial t} + \frac{\partial}{\partial x} \left(\frac{Q^2}{A_f} \right) + gA_F \frac{\partial \zeta}{\partial x} + \frac{gQ|Q|}{C^2 R A_F} - w_f \frac{\tau_{wind}}{\rho_w} + gA_F \frac{\xi Q|Q|}{L_x} = 0 \quad \text{Equation 3}$$

Where:

A_T	Total area (i.e., summation of flow and storage areas) (m ²)
A_F	Flow area (m ²)
t	Time (s)
q_{lat}	Lateral discharge per unit length (m ² /s)
Q	Discharge (m ³ /s)
C	Chézy value (m ^{1/2} /s)
g	Acceleration due to gravity (m/s ²)
ζ	Water level (m)
L_x	Length of branch segment, accommodating an extra resistance node (m)
R	Hydraulic radius (m)

w_f	Water surface width (m)
x	Distance along the channel axis (m)
ρ_w	Density of freshwater (kg/m ³)
τ_{wind}	Wind shear stress (N/m ²)
ξ	Extra Resistance coefficient (s ² /m ⁵)

The first term in the 1D momentum equation above defines inertia, followed by the second term, which describes convection, the third term describes the water level gradient, the fourth term characterises the bed frictions, while the fifth and sixth terms define the influence of the wind force and the extra resistance, respectively. The convection term ensures the conservation of momentum in branches and connection nodes connected to two branches.

2D Flow Equations

The equations applied for the computation of 2D flow are non-linear and a subclass of the notable shallow water equation that depicts water flow with higher horizontal accelerations than vertical accelerations. 2D flow is modelled by solving one continuity equation and two momentum equations.

Continuity equation (2D):

Fluid conservation is guaranteed by the continuity equation. The equation is stated below:

$$\frac{\partial \zeta}{\partial t} + \frac{\partial hu}{\partial x} + \frac{\partial hv}{\partial y} = 0 \quad \text{Equation 4}$$

Momentum equation (2D):

Momentum equations are solved for the x and y directions. These equations comprise horizontal pressure gradient, acceleration, convective, bottom friction as well as wall friction are stated below:

For the x-direction:

$$\frac{\partial u}{\partial t} + u \frac{\partial u}{\partial x} + v \frac{\partial u}{\partial y} + g \frac{\partial \zeta}{\partial x} + g \frac{u|\bar{u}|}{C^2 h} + au|u| = 0 \quad \text{Equation 5}$$

For the y-direction:

$$\frac{\partial v}{\partial t} + u \frac{\partial v}{\partial x} + v \frac{\partial v}{\partial y} + g \frac{\partial \zeta}{\partial y} + g \frac{v|\bar{v}|}{C^2 h} + av|v| = 0 \quad \text{Equation 6}$$

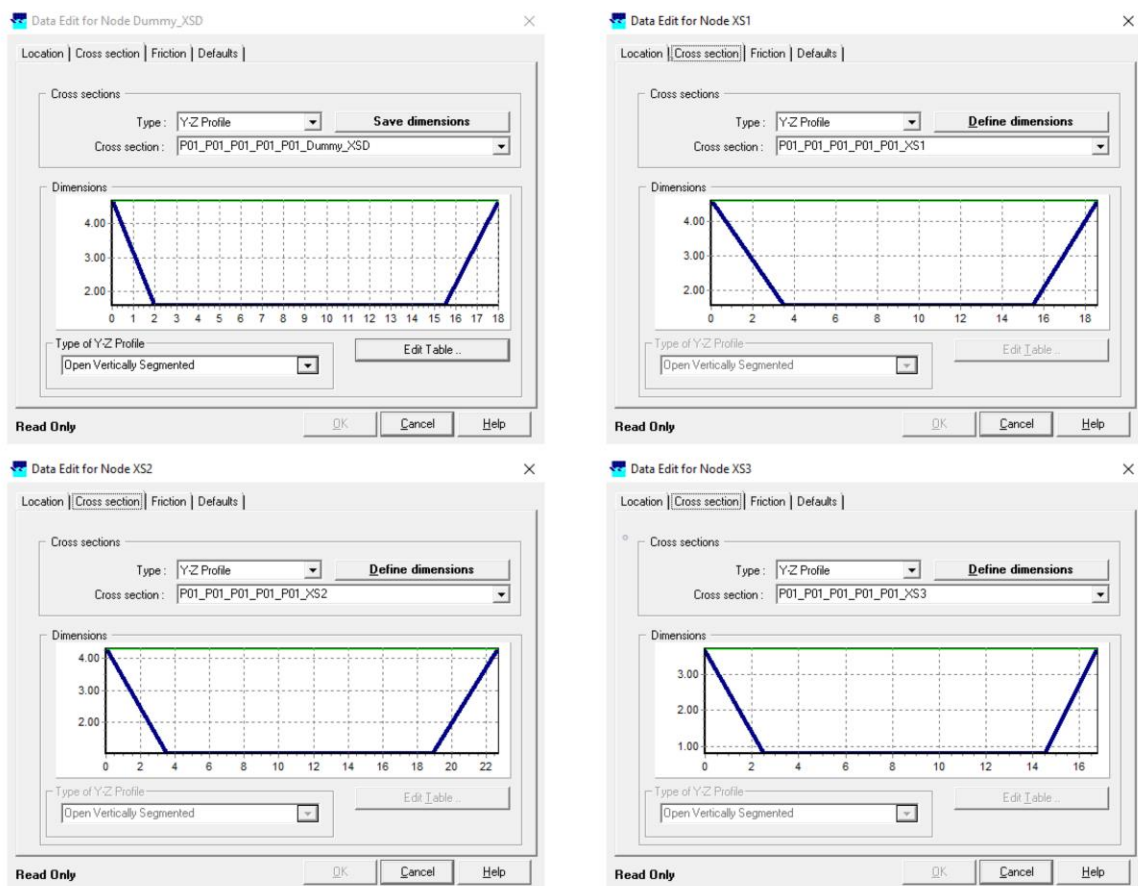
Where:

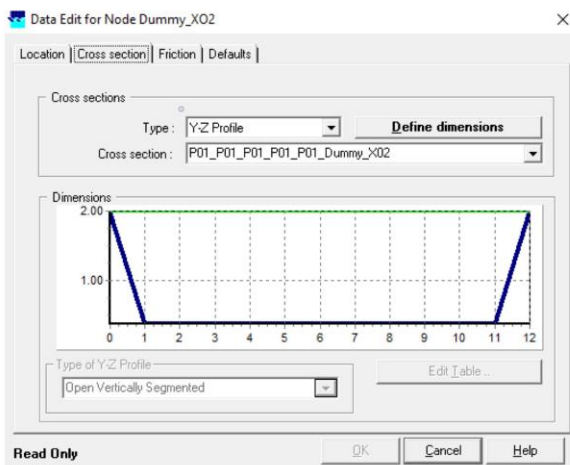
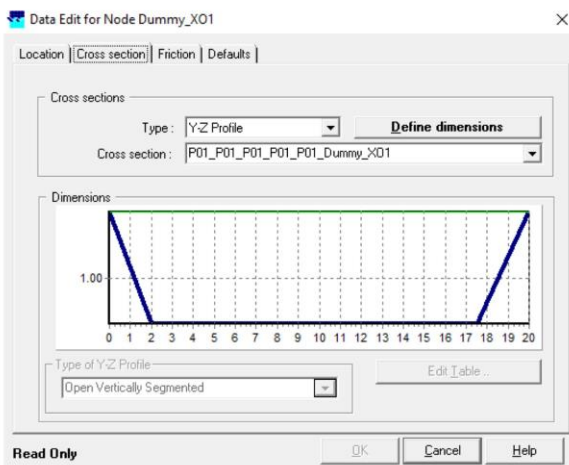
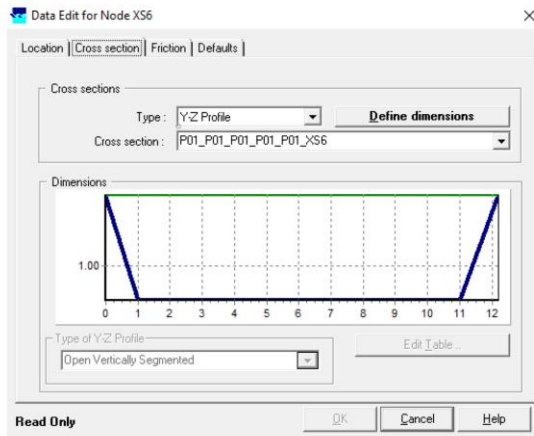
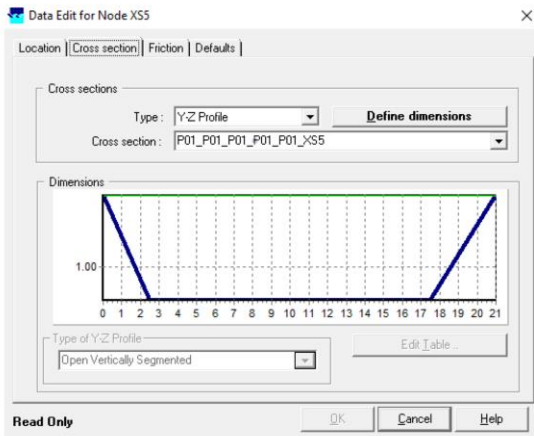
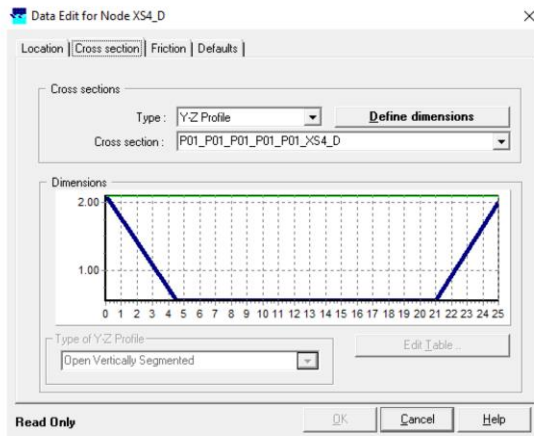
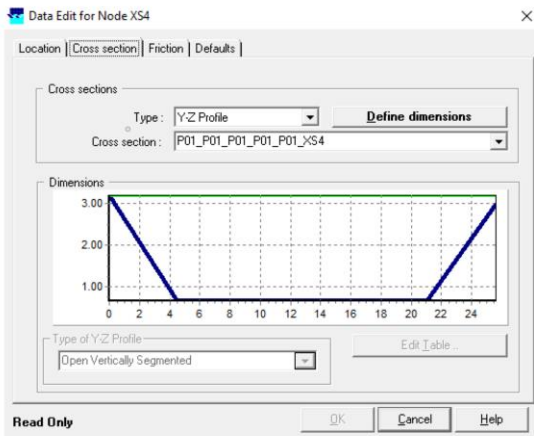
u	Velocity in x-direction (m/s)
v	Velocity in y-direction (m/s)
$ u $	Velocity magnitude ($= \sqrt{u^2 + v^2}$) (m/s)
ζ	Water level above the plane of reference (m)
C	Chézy coefficient ($\sqrt{m/s}$)
h	Total water depth ($= d + \zeta$) (m)
d	Depth below the plane of reference (m)
a	Wall friction coefficient (1/m)

In contrast to the shallow water equations, the 2D equations described above do not include turbulent stress terms responsible for sub-grid momentum transfer amongst grid cells. These terms are comparably insignificant for flood flow calculation, and their exclusion is to save computational work. On the contrary, the inclusion of the wall friction terms addresses the increase in resistance triggered by vertical obstructions such as trees and buildings. The average diameter and number of obstructions per unit area and the average obstacle drag coefficient are used to calculate the wall friction coefficient. In this study, wall friction terms were not considered since the data required to account for vertical obstructions and their necessary properties were not available for the study area. Detailed information on all the terms used in both 1D and 2D flow equations is contained in Deltares (2018).

Dimension of cross-sections used in the schematisation of the model

Y-Z profile cross-sections





Trapezium profile cross-sections

